12-2008

Emergent Phenomena in Spatially Confined Manganites

Thomas Z. Ward
University of Tennessee - Knoxville

Recommended Citation

Ward, Thomas Z., "Emergent Phenomena in Spatially Confined Manganites. " PhD diss., University of Tennessee, 2008.
https://trace.tennessee.edu/utk_graddiss/535

To the Graduate Council:

I am submitting herewith a dissertation written by Thomas Z. Ward entitled "Emergent Phenomena in Spatially Confined Manganites." I have examined the final electronic copy of this dissertation for form and content and recommend that it be accepted in partial fulfillment of the requirements for the degree of Doctor of Philosophy, with a major in Physics.

E.W. Plummer, Major Professor

We have read this dissertation and recommend its acceptance:

Elbio R. Dagotto, Pengcheng Dai, Takeshi Egami, Jian Shen

Accepted for the Council:

Carolyn R. Hodges

Vice Provost and Dean of the Graduate School

(Original signatures are on file with official student records.)

To the Graduate Council:

I am submitting herewith a dissertation written by Thomas Z Ward entitled "Emergent Phenomena in Spatially Confined Manganites." I have examined the final electronic copy of this dissertation for form and content and recommend that it be accepted in partial fulfillment of the requirements for the degree of Doctor of Philosophy, with a major in Physics.

E.W. Plummer, Major Professor

We have read this dissertation
and recommend its acceptance:

Elbio R. Dagotto

Pengcheng Dai

Takeshi Egami

Jian Shen

Accepted for the Council:

Dr. Carolyn R. Hodges
Vice Provost and Dean of the Graduate School

(Original signatures are on file with official student records.)

Emergent Phenomena in Spatially Confined Manganites

A Dissertation
Presented for the
Doctor of Philosophy Degree
The University of Tennessee, Knoxville

Thomas Z Ward
December 2008

Acknowledgements

For my family, mom, dad, Mike and Jenny, it must have seemed that I would never leave school. Well, I am fairly certain that this dissertation will be the last piece of work that I ever do as a student…probably. It is their support that has allowed me to follow my many whims and finally find my passion. Without them, I wouldn't be where I am.

I have been incredibly fortunate to work with the best advisors that any student could hope for. Ward Plummer and Jian Shen are not only two of the best scientific minds that I have ever met but two of the best people who I have ever met. When applying to graduate schools, I sent out emails to groups around the country whose work interested me. Ward was the only professor who answered me directly which is truly shocking now that I know what kind of demands he has on his time. His support of his students and his unwavering dedication to science have been inspirational. Jian has been my *de facto* advisor in day-to-day research and has been an incredible influence. Words really can't express the gratitude that I feel for all that he has done for me. Thank you, Jian.

I also need to thank my committee: Elbio Dagotto, Pengcheng Dai and Takeshi Egami. I appreciate them giving me their valuable time and even more valuable guidance.

The many all-nighters that were common for me while doing the research presented in this dissertation would have surely driven me to a nervous breakdown if it weren't for my friends. It was my pleasure to be at the first meeting of T-shirt girl and

Adam Krause and to later be the best man in their wedding. Shaun Ard has also been a great friend even though he isn't very good at video games. Kelly deserves thanks too for not throwing me out when she would come home from a long night of work and find Shaun and me sitting on the couch yelling at the TV. Joyce, Tiny, Mathew, Ben, Stephen and the handful of other graduate students that weren't scared to leave the house on a Friday night have also made the long nights in the lab bearable. I have known Al, Clint, Derek, Jeff, Jerry and Nate for almost 20 years; our lives have all taken different paths, but somehow they continue to be the people with whom I have the most in common.

Doing my research at ORNL has allowed me to interact with some truly amazing people. I have been lucky to work with Paul Snijders over the last couple of years. I always enjoy his insight on science and Tennessee culture. Zsolt Marton has been "instrumental" in keeping me in the PPMS rotation. John Budai deserves special thanks for taking the time to teach me the many intricacies of X-ray diffraction and showing me how important it could be in my studies.

Playing on the Stonefingers softball team has given me hope that life as a scientist doesn't mean that I have to be a shut-in. Though we only won a handful of games, we were undefeated in post games. I appreciate all of the *advice* that my teammates gave me about options after graduation—sorry guys, but I have decided not to go to medical school. After all, surgeons don't wear Viking helmets and drink Scandinavian moonshine out of Dixie cups.

Abstract

Rare earth manganites exhibit colossal magnetoresistance (CMR). There is evidence that alloyed single crystal materials in this class can display electronic inhomogeneity in which areas with vastly different electronic and magnetic properties can form and coexist in phase separated domains ranging in size from a few nanometers to micrometers. This phase separation (PS) is of particular interest, as it has been suggested that it is the central feature that leads to CMR in manganites, the Mott transition in VO_2 and may play a role in high-TC superconductivity in cuprates. However there is debate as to its precise role.

The purpose of my research is to answer fundamental questions about the specific role of PS in complex oxides. I reduce single crystal thin films of an electronically phase separated manganite to the scale of their inherent electronic phase domains near the metal-insulator transition. Unlike transport measurements done on bulk or thin films where the electrons follow only the metallic path of least resistance, this configuration forces electrons to travel through both the metallic and insulating regions residing in the material. This has led to observations of several new phenomena such as a reemergent metal-insulator transition, ultra-sharp jumps in resistivity at the metal-insulator transition, and the first high resolution observation of single domain electronic phase transitions in the time domain.

While the manganites will be the primary focus throughout this dissertation, the spatial confinement techniques presented here are not limited to only these materials.

They can be applied to any phase separated system to probe regions resistively hidden to transport measurements.

Contents

List of Figures

Chapter 1 Introduction and Background

1.1 Introduction

When someone without a background in condensed matter physics asks me what I have spent the last 4 years doing, I ask whether they want the short or long answer. The short answer is that I have been shooting lasers, electron beams and X-rays at stuff and then trying to understand the results and predict what will happen the next time. In this dissertation, I will assume that the reader wants the fuller and much more interesting long answer.

Currently, the condensed matter physics community is devoting a great deal of attention to complexity and the nanoscale. Being *complex* means that a system can have large scale properties that emerge from many inseparable and interacting components thereby being more than a simple sum of its parts. It can be thought of as sort of ordered chaos in which slight and often immeasurable differences in a material can create vastly different physical properties. Nanoscale has become a buzz word recently but has real meaning. Nano simply refers to sizes on the order of a billionth of a meter. At this scale, there is a crossover between classical large scale physics and quantum physics. Our aim is to study the effects of reducing complex materials to smaller and smaller scales. We can expect that at some length scale the influence of the complexity that creates the emergent behaviors we see at macro scales will break down. However, it is unclear where this line lies and if there are new phenomena that can be found near or below it.

By combining nanoscale physics with complex materials we hope to find new behaviors.

1.2 Perovskites

Many materials in the metal oxide class have exotic properties such as colossal magnetoresistance and high T_C superconductivity. The reason that there is such a wide range of interesting behaviors is a direct result of the underlying crystalline structure in these materials. The ideal perovskite form is cubic with an empirical formula ABO_3--the A cations are located on the corners, the B cation is located in body center, and the oxygen occupy the faces (Figure 1-1). However most perovskite materials deviate from this perfect cubic form and exhibit distortions that make the true structure rhombohedral, tetragonal or orthorhombic.

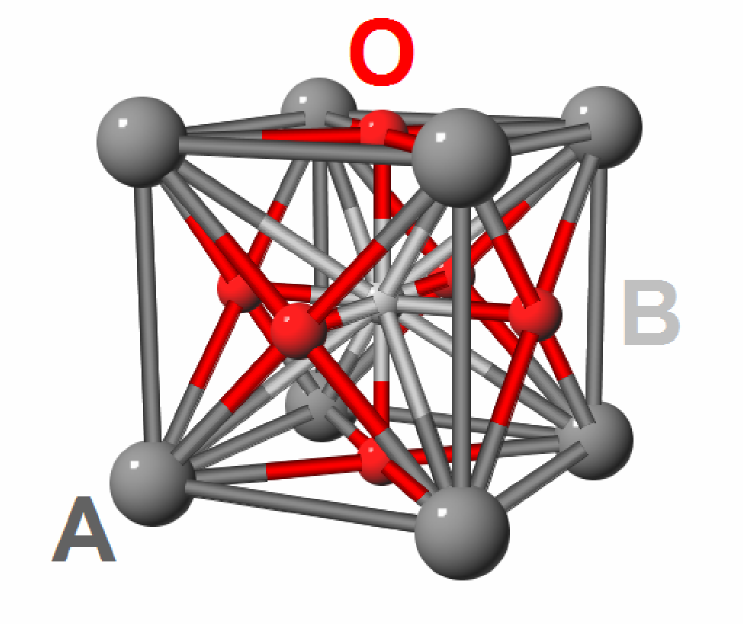

Figure 1-1: Perovskite structure. A-site shown as dark grey on corners of cubic structure. B-site shown as light grey inhabiting center of octahedra. Oxygen shown as red.

The perovskite is a very resilient structure and has a relatively high tolerance factor defined by $t = \frac{R_A + R_O}{\sqrt{2} \cdot (R_B + R_O)}$ where R_O, R_B, R_A are the ionic radii. The perovskite structure is stable when $0.78 < t < 1.05$. When t is close to 1, the structure will be cubic. With $t < 0.81$, the central octahedra will tilt to fill the space left by the reduced A site. This wide stability range means that the perovskite structure is stable under a wide mixing of A and B cations and can tolerate a relatively number of atomic vacancies without structural collapse[1]. The high degree of tolerance also allows sites to be mixed through doping of similar species. The slight changes to the crystalline structure caused by this mixing are closely linked to the electronic structure and are the foundation of the unusual and dynamic behaviors observed in many complex metal oxides. Figure 1-2 shows several examples of perovskites with different chemical compositions and their applications.

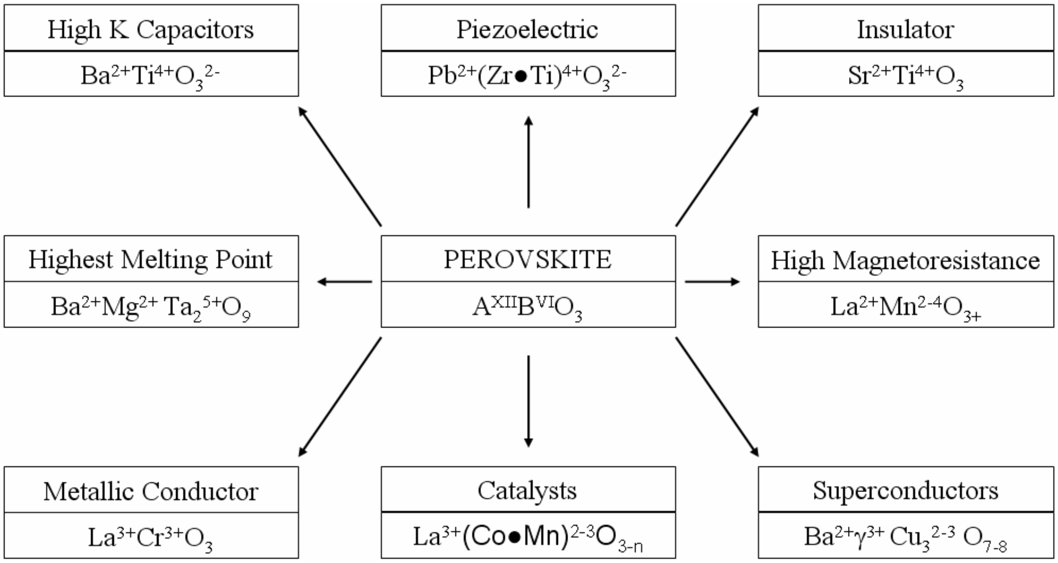

Figure 1-2: Various perovskites and their applications[1].

1.3 Magnetism and Transport in Manganites

Many of the interesting properties and seemingly disproportionate effects of small systemic changes in the doping, strain field, etc. associated with manganites can be attributed to the similar scale of the energetics contributed by the perovskite structure and the electronic structure of the atoms that inhabit it. When attempting to construct a model of manganite behavior, several components must be taken into account: atomistic degrees of freedom for the two e_g orbitals on each manganese atom, spin degrees of freedom from the t_{2g} core electrons, and phonon degrees of freedom contributed by the distortion in the central octahedral. What we find is that each of these energies is of a similar scale [Table 1-1] which leads to complex phase diagrams and tremendous sensitivity to field perturbations[2].

Table 1-1: Comparison of energy scales for degrees of freedom in manganites.

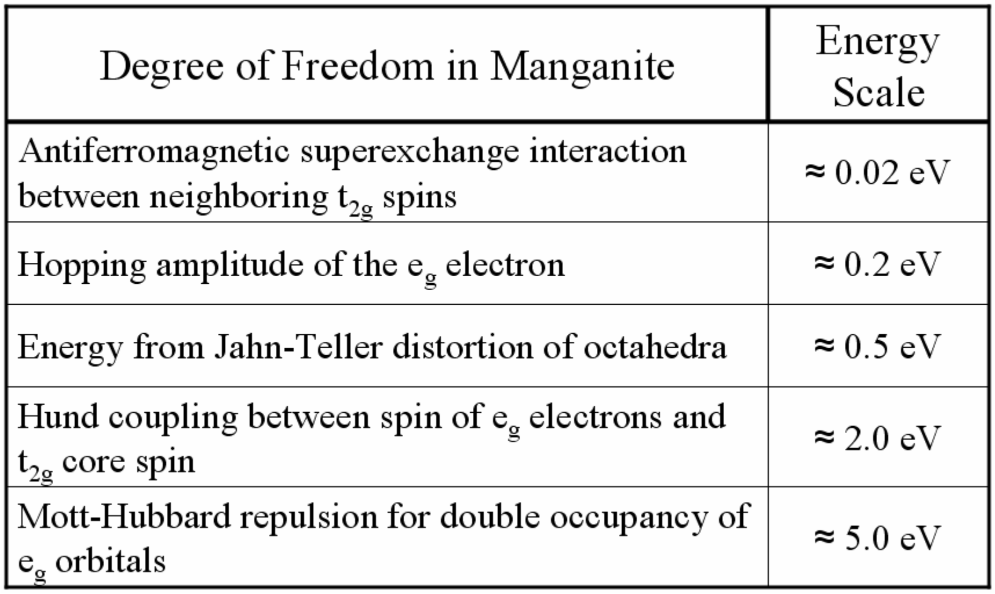

Degree of Freedom in Manganite	Energy Scale
Antiferromagnetic superexchange interaction between neighboring t_{2g} spins	≈ 0.02 eV
Hopping amplitude of the e_g electron	≈ 0.2 eV
Energy from Jahn-Teller distortion of octahedra	≈ 0.5 eV
Hund coupling between spin of e_g electrons and t_{2g} core spin	≈ 2.0 eV
Mott-Hubbard repulsion for double occupancy of e_g orbitals	≈ 5.0 eV

Complex metal oxides of a perovskite structure exhibit a range of extraordinary magnetic and electronic behaviors that are not fully understood. In order to gain understanding, a great deal of experimental and theoretical research has been conducted over the last 20 years. While there is no full description that is capable of explaining all behaviors in all conditions, it is clear that these systems can not be explained through the simple single-electron band model that is commonly and successfully used on other materials. Because of this, it has become apparent that there must be strong first order interactions, such as electron-lattice correlations and electron-electron interactions, within complex oxides that would be capable of imparting such exotic properties.

A purely theoretical understanding of the relationship between these energies and their true effects on observed systems is currently unavailable. The simple models that do exist are capable of showing multiple phases residing in a single system. One treatment that comes close to taking into account all of the involved energies is described as the two-fluid model in which electron-lattice coupling acts to split the e_g orbitals' degeneracy which creates two states at each manganese site. One state has a bare hopping amplitude while the other is polaronic which gives it a much smaller hopping amplitude[3]. This creates regions of mesoscale segregation as local Mott-Hubbard repulsion denies simultaneous residence of both states on a single site. Further, there is a preference for these states to group in mesoscale puddles to conserve the system's kinetic energy. This model proposes that manganite systems have an intrinsic preference toward phase separation based on the overriding importance of the electronic correlations.

The manganites offer an excellent example of a complex oxide with unexplained behavior. The manganite class of complex oxides exhibits colossal magnetoresistance

(CMR). A CMR material has orders of magnitude change in resistance when it is subjected to a magnetic field. Figure 1-3a shows transport data on bulk $La_{5/8-y}Pr_yCa_{3/8}MnO_3$ (LPCMO). There are several important features to note in this data. The shapes of the curves across the temperature regime show a clear onset toward a higher resistivity in all curves at ~220K. This is also the point at which hysteresis is closed and is defined as the material's Curie temperature (T_c). With increased Pr doping the maximum resistivity of the material grows and the temperature of maximum resistivity shifts lower. For all of the shown dopings, we see a transition from metallic to insulating on the warming curves (dotted lines). This is known as the metal-insulator transition (MIT). The character of this transition is clearly different depending doping—evolving from an evidently smooth transition at higher temperature for low Pr dopings to a relatively sharp transition at lower temperatures for higher Pr dopings. Figure 1-3b shows the magnetoresistance of the various dopings. This is found by taking the change in resistivity at an applied magnetic field from the resistivity at zero magnetic field and dividing it by the resistivity at the applied field. There is a several order of magnitude change in the resistivity with the application of a modest field of only 0.4T. It is this huge change in resistivity that gives manganites their *colossal* magnetoresistance. The proposed reasons for this curious behavior and our contributions to its understanding will be presented below.

It may seem surprising that such a great deal of attention has been given to understand how these materials work without any final solution being arrived at. However, what makes the manganites so interesting is also what makes them so difficult to explain. As was shown in Table 1-1, there are many different interactions within these

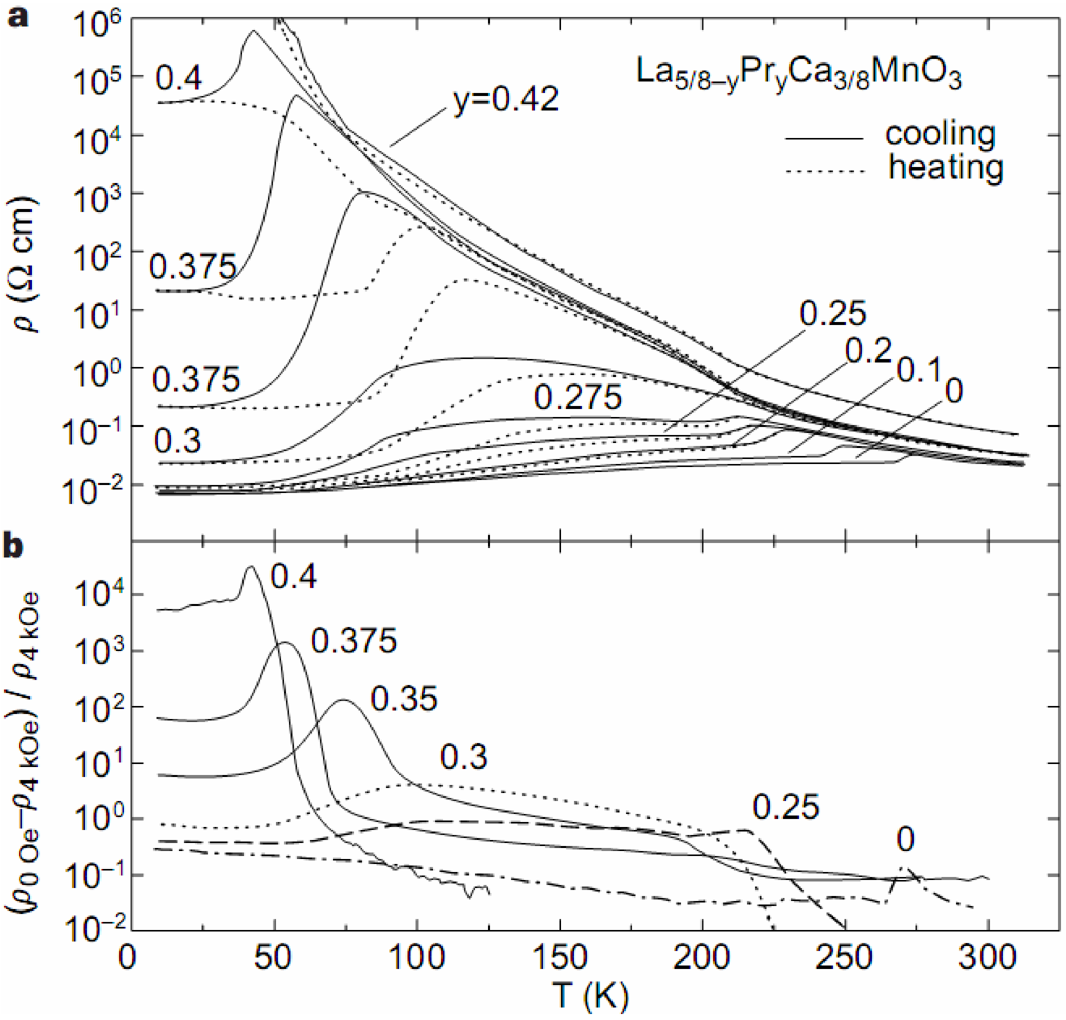

Figure 1-3: Example of Colossal Magnetoresistance in transport measurements of a manganite. (**a**)Resistivity vs. temperature measurements for several dopings of LPCMO. (**b**)Relative change in resistivity upon the application of a 0.4T magnetic field. Reproduced from Uehara, et al[4] with permission from Nature Publishing.

materials of similar energies which act to balance and interact with one another. This gives us the ability to *tune* manganites through slight manipulations of strain, chemical pressure, lattice vibrations, applied magnetic field and temperature. The long list of sensitivities offers us a model in which to study poorly understood physics in systems where small local phenomena can have global effects. It should also be noted that aside from the purely scientific desire to understand CMR, manganites are being studied for application as spin valves[5], current limiters[6], bolometers[7] and magnetic storage[5].

As discussed earlier in this chapter, the manganites are perovskites based on the ABO_3 structure. The family in this class that has received the most attention recently has been of the form $R_{1-x}A_xMnO_3$, where A is a divalent alkali—often Ba, Ca, Pb or Sr—and R is a rare earth—often La, Nd, or Pr. The central Mn^{3+} ion holds 4 out of a possible 10 electrons in its outer 3d levels. By slightly shifting the component dopings, vast changes in the overall character of the material can be observed. Though this sounds fairly straight forward, it is necessary to view these systems in an even more simplified manner. There are two important models to consider for these systems: the delocalized band model and the localized ionic depiction. Both of these have their strengths. From the standpoint of a physical interpretation, the band model offers a good understanding of the ionic overlap present in manganites. The ionic depiction is simple and can do a reasonable job of explaining observed characteristics.

Using the ionic model is applicable because of the very narrow width of the d-band in which the Fermi level is located. In Figure 1-4, we see the orbital orientations for Mn and O ions inside the octahedra. There are two e_g orbitals, $d_{x^2-y^2}$ and $d_{3z^2-r^2}$, directed toward the axis and three t_{2g} orbitals, xy, yz, and zx, which have their barbell directed toward the axis of the e_g orbitals. The manganese's e_g orbitals in d can easily overlap the oxygen's p orbitals. This overlapping is the strongest conduit for conduction in this system. Small changes away from a perfect cubic structure will therefore greatly influence transport as the orbital overlap will be influenced as the average A-site ionic radius $<r_A>$ and bond angle are modified. As the crystal structure is pushed from the cubic structure to tetragonal or orthorhombic, the degeneracy of the d orbitals changes and splits with the shift in crystal field as the physical structure of the lattice changes[8].

The crystal's orbital symmetry has a strong influence on energy splitting. Hund's coupling has an important influence in manganites. Electrons will selectively fill levels with a similar spin until all available levels are full. Even though the e_g orbitals are

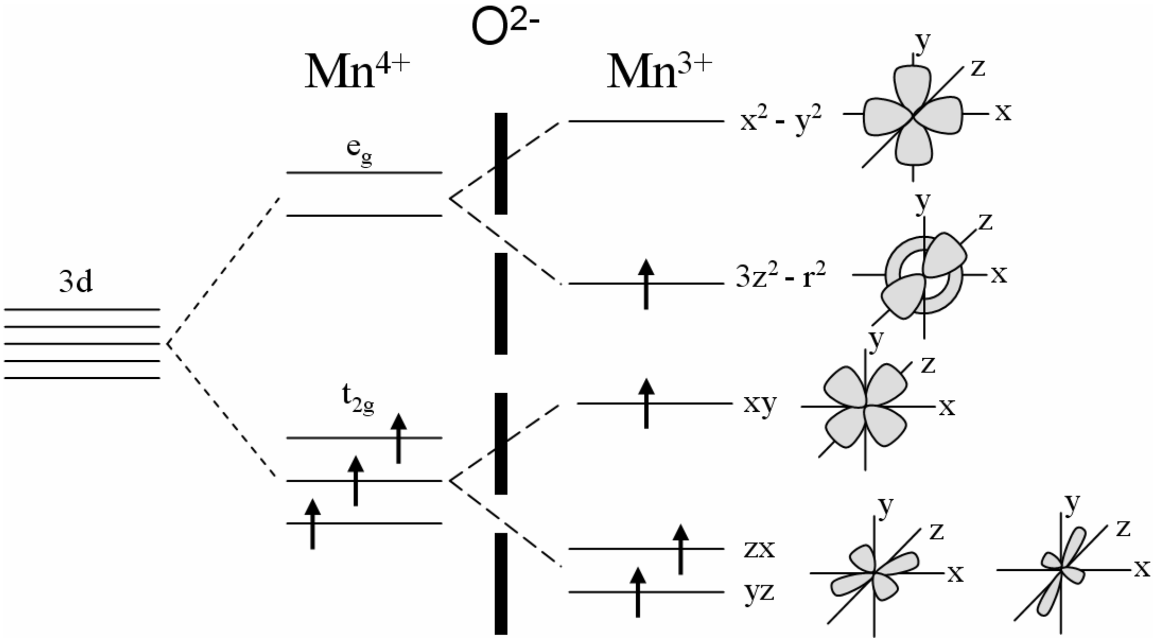

Figure 1-4: Arrangement of 3d orbitals to p orbitals.

degenerate when in a free ion form of manganese, in certain configurations, the t_{2g} orbital has only one electron in each level which will conform to Hund's rule and be filled with electrons with identical spin. Thus in order to conserve energy, the normally doubly degenerate e_g orbitals, when only containing one electron, will have a preference toward one orbital depending on the crystal field. The orbital symmetry within the crystal has an influence in energy splitting that needs to be taken in context with physical distortions in the lattice. These symmetry driven distortions are a direct result of the coulombic interactions of the electrons and are known as Jahn-Teller (JT) distortions.

As an example, when the $d_{3z^2-r^2}$ orbital is directed along the z plane and the $d_{x^2-y^2}$ orbital is in the same plane as the oxygen octahedra, a decrease in coulombic repulsion between oxygen ions is achieved by elongating the Mn-O bond in the z plane in favor of the $d_{3z^2-r^2}$ orbital. This is accompanied with an enhancement in coulombic repulsion caused by the compression of the octahedra in the xy plane [Figure 1-5]. What this means is that there is interplay between elastic strain and energy lowering for certain distortions of the crystalline structure. JT distortions can be cooperative in the case of a high concentration of the Mn^{3+} ion in the structure which creates a system in which the distortions are dependent on one another and will have a global influence. Dynamic JT distortion is found when there are a few energy minima which allow the system to choose local thermal or quantum transitions and does not show the same global influence as the cooperative case. If the charge carriers have a high enough mobility, the distribution of the Mn^{3+} and Mn^{4+} ions is dynamic and random. From this we understand that electron-phonon coupling will arise[9]. And due to Hund's coupling, magnetic polarons can also be

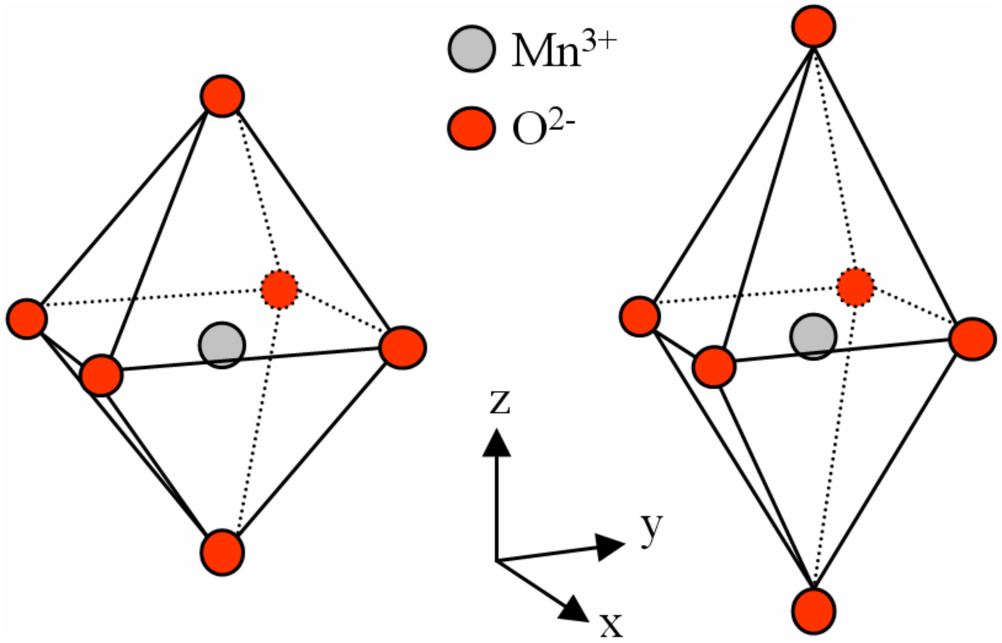

Figure 1-5: Example of Jahn-Teller distortion in oxygen octahedra. On the left the undistorted octahedra is shown. The image on the right shows the elongation of the octahedra along the z-axis and balancing compression in the y and x planes.

formed[10]. This has an important influence in transport above T_c in CMR manganites; the localization of carriers through lattice or magnetic polarons has been used to explain the activated behavior of resistivity above T_c[11,12].

Ferromagnetism is closely related to the crystallographic and band structures of manganites. In 1951, Zener proposed that ferromagnetism in these materials was caused by an indirect coupling between Mn^{3+} and Mn^{4+} through a conduction electron mediated by the oxygen ion[13,14]. He postulated that inserting a divalent ion at a rare earth position would cause the Mn ions to change their valence to a mixed state. In the $R_{1-x}A_xMnO_3$ system, where R is a rare earth and A is a divalent cation, there is an x fraction of Mn in the tetravalent Mn^{4+} with S = 3/2 state and 1-x in the trivalent Mn^{3+} with S = 2 state [Figure 1-6]. This creates a degeneracy in both the initial and final states which delocalizes the hole and carrier in the Mn sites and allows for concurrent transfer of electrons across the intervening oxygen site through the overlap of the Mn 3d orbital and O 2p orbital. From Hund's coupling, the conduction electron must be aligned with those in the acceptor site. This explanation is able to account for ferromagnetism and high conductance.

This model was later broadened to include the Mn magnetic moments. Here the core t_{2g} spins were treated classically while the e_g conduction electron was treated quantum mechanically. From this, it is possible to model a transfer probability $t = t_0 \cos(\theta/2)$ where t = 1 at $\theta = 0$ and t = 0 at $\theta = 180$ [Figure 1-6]. This gives lower exchange energy when the conduction electron's spin is in line with the total spin contributed by the Mn cores[15]. Many further modifications to this base model have been made over the past 50 years[16-19] that further strive to explain the basic transport and magnetic states present in CMR manganites. However all of these models are only able to give a qualitative explanation of transport. They are not able to map observed Curie temperatures, explain multiple electronic and magnetic phases, predict the sheer size of the CMR effect, nor can they fully explain the observed charge and orbital orderings.

To fill in the gaps that double exchange alone was not able to fill, electron-phonon coupling was proposed[20]. In this model, dynamic JT distortions are taken into account in order to link Hund's coupling and charge localization through electron-phonon coupling to create a ferromagnetic metallic phase that gives a close match to the experimentally observed behavior of manganites[21]. Here, local variations in the crystal

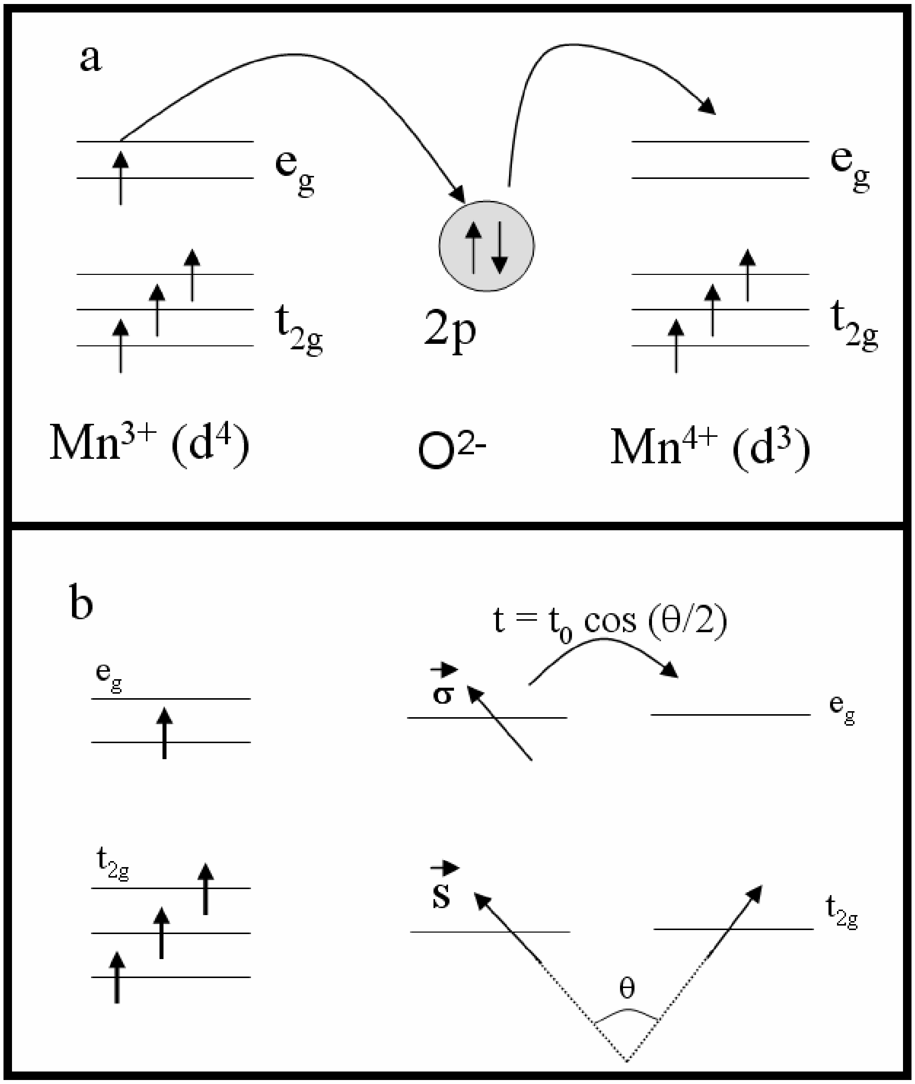

Figure 1-6: Zener's double exchange model and de Gennes spin-canted states

created by JT distortions act to locally vary the Mn-O bond lengths which then break local symmetry and split e_g degeneracy. Thus when the e_g conduction electron selects to reside in the lower energy orbital, it becomes trapped within the local lattice deformation and forms a lattice polaron. The transport of these lattice and spin distortions is known as a magnetic polaron. Temporal and spatial Jahn-Teller distortions at and above T_c can create a localization of charge carriers[20,10,22,11,9] and requires both double exchange and Jahn-Teller coupling to justify the many magnetic phases. This model gives a much closer fit to experimental observations than those models discussed in the previous paragraphs. Experimentally, carrier self-trapping through small polarons above T_c due to electron-phonon coupling induced by J-T distortions has been shown by transport measurements[23], neutron scattering[24] and optical conductivity[25]. The agreement between theory and experimental observations suggests that the lattice effects created by JT polarons have an integral part in CMR. The size of the CMR effect and a manganite's ability to undergo phase transition is directly related to the strength of the double exchange mechanism and electron-phonon coupling.

Phonon related electron hopping between Mn sites can be thought of in terms of a polaronic model. Polarons can be considered to be present when large effective masses and thermally activated carriers are observed. Polaron formation occurs when small regions of lattice distortion are created by high local densities of carriers or holes. This creates local correlations in the electronic structure that allows thermally activated transport through the lattice. In Figure 1-7a, we see a dielectric polaron which can be

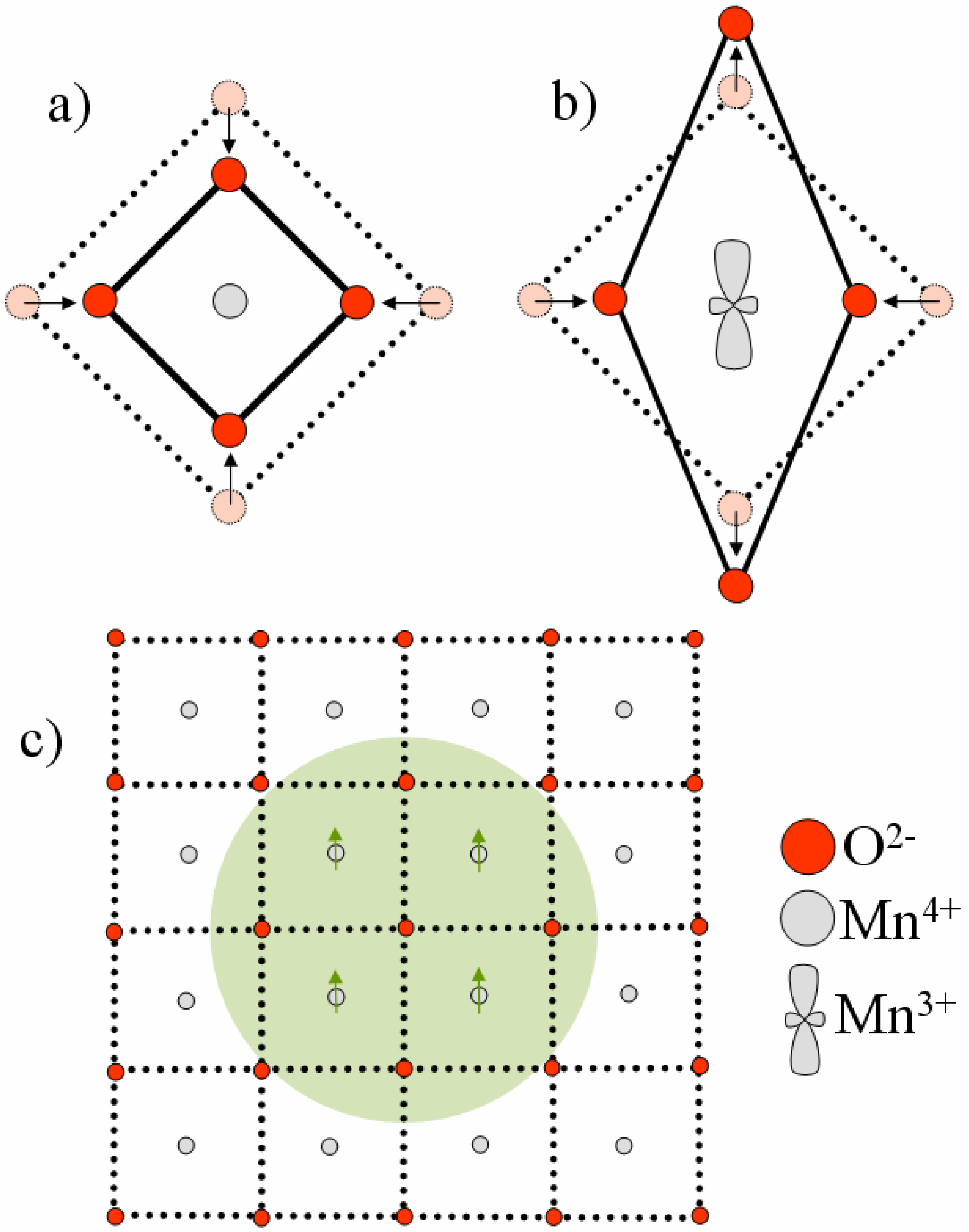

Figure 1-7: Types of polarons. (**a**)Dielectric. (**b**) Jahn-Teller. (**c**) Magnetic—shaded area denotes local correlation of spins within the polaron.

created by decreasing the $<r_A>$. The decrease in local chemical pressure effectively pulls the surrounding structure inward. Figure 1-7b is an example of a Jahn-Teller polaron. Here the lattice distortion is held and shaped by the electronic structure present at the center of the octahedra. Figure 1-7c shows a magnetic polaron. In this configuration, a region is locally correlated by spin direction. It can be noted that interpoloranic correlations have been observed but only in orthorhombic structures[26].

Charge ordering (CO) in transition metal oxides is a proposed alternative to JT distortion. CO is observed when electrons localize on specific lattice sites due to cation ordering. This ordering is often seen in transport measurements as the material taking on an insulating or semiconducting character. Possible verification of this has observed by several methods such as neutron scattering experiments[27,28]. There is evidence that this behavior has a strong dependence on the average A site ionic radius $<r_A>$. By reducing $<r_A>$ through doping, charge carriers tend to localize and find it energetically favorable to order; as in LCMO with a about ½ Ca and ½ La doping. At low temperature, this material has been claimed to show electronic ordering with stripe modulation on the scale of nanometers[29] and to exhibit AF ordering[30]. There also exists an orbital degree of freedom in the Mn^{3+} e_g electrons that can be used to create JT distortions at lower system energy. Possible evidence of charge ordering has been observed in several TMO systems. One example of this is a transmission electron microscope (TEM) study done on LCMO well below the T_c [Figure 1-8]. In this work, a stripe pattern was observed and attributed to stable $Mn^{3+} O_6$ octahedra in a strongly JT distorted region were observed in a striped configuration with undistorted $Mn^{4+} O_6$ octahedra[29]. The most interesting finding was that the periodicity of the stripes could be integer tuned through carrier dopant. This

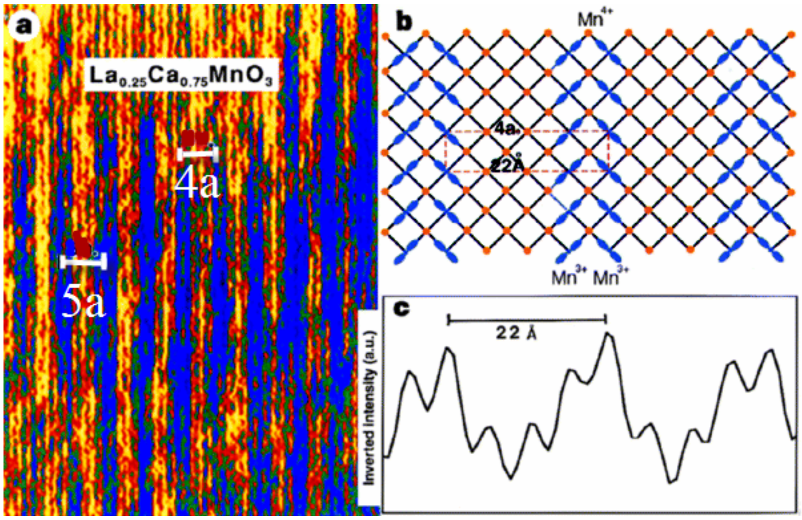

Figure 1-8: Pairing of charge ordered stripes in $La_{0.25}Ca_{0.75}MnO_3$. (**a**)TEM image taken at 95 K showing stripes with a $4a_0$ periodicity. (**b**)Diagram showing representation of proposed model comprised of three paired Jahn-Teller stripes. (c)Inverted intensity scan with same horizontal scale as (b) showing stacking fault of $5a_0$ attributed to paired Jahn-Teller stripes. Reproduced from Mori, *et al*[29] with permission from Nature Publishing.

suggests that physical lattice distortions might be the primary ingredient needed for charge ordering in manganites. There is still some debate on this, as some have suggested that CO might not be confined to regions with no sum magnetization, and could be found in ferromagnetic regions[31,32]. What seems obvious though is that when modeling these systems it is vital to take CO into account.

1.4 Phase Separation

Though single crystal transition metal oxides may be grown chemically disordered (random alloy), they are often not electronically monophasic. Frequently they exhibit electronic phase separation in which domains of different magnetic and electronic properties can coexist near transition. These domains can be on the order of nanometers to microns depending on the chemical composition of the material in question. There are several theoretical models that attempt to explain their behavior but none are successful in fully describing and predicting it.

Colossal magnetoresistance, high T_C superconductivity and metal-insulator transitions have become some of the most studied areas of condensed matter physics; however there is yet no known theoretical model that is capable of fully explaining any one of these behaviors let alone a unifying understanding capable of explaining the effects of complexity on emergent behavior as a whole. The one thing that many of the materials exhibiting these curious properties share is electronic phase separation. For this reason, it is imperative that we fully understand this new and fundamental phenomenon. Many systems with correlated electrons, such as manganites, cobaltates and cuprates, have been shown to contain inherent electronic inhomogeneity near phase transition. The shape and scale of phase separation is different for different systems and can take the form of stripes, dots or stochastic puddles with sizes ranging from a few nanometers to several micrometers. What is also of interest is that experimental probing and imaging techniques have suggested that there is not necessarily any preferred domain nucleation site under thermal cycling which suggests that the seeding of phase domains is a purely emergent phenomenon. In some systems, the inhomogeneities will always seed at the same position; but in other cases, the domains may migrate or change with changes in external conditions such as applied electronic fields, applied magnetic fields or temperature cylcing[2]. The fact that this separation is present in so many materials of such varying character raises many questions as to the true contribution from electronic inhomogeneity and the fundamental causes of phase separation.

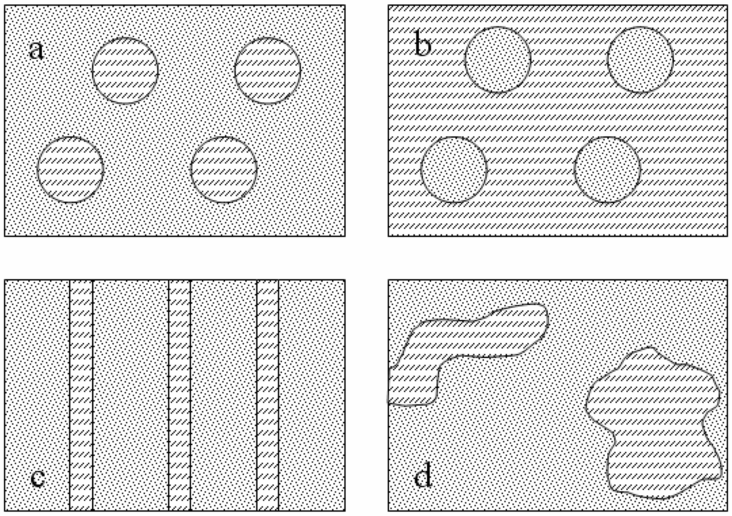

Figure 1-9: Examples of phase separation in oxides. Dotted regions represent insulating areas and thatched regions representing metallic areas. (**a**)Metallic puddling. (**b**)Insulating puddling. (**c**)Charge striping. (**d**)Mesoscopic phase separation into metallic and insulating regions.

A great deal of work has been done in an effort to probe and image phase separated domains. The various methods used are dependent on the scale and type of inhomogeneity being investigated. Nanoscopic phase separation has been proposed from observations taken with nuclear magnetic resonance imaging[33] and Mossbauer spectroscopy[34]. Physical characteristics of the lattice and its magnetic properties can be obtained using neutron[35] or X-ray[36] diffraction techniques. These diffraction techniques have a large averaging component due to their lack of spatial resolution to single nanometer scale but nonetheless have been used to speculate on the existence of phase separation. The most widely used method and the subject of most of our experimental work is in the study of transport and magnetization data. These methods, like the diffraction methods, are generally only capable of making measurements that give averaged information taken from the entire sample. However, as will be discussed in a later chapter, there are ways to improve upon these methods to probe to single domain scales.

To reduce the problems associated with averaging data taken from an entire sample, some methods have been used to claim imaging of single phase domains with nanometer resolution. This is accomplished through transmission electron microscopy[4], magnetic force microscopy[37,38] and scanning tunneling spectroscopy[39]. While these methods offer good spatial resolution, they can be limited by a relative lack in temporal resolution. This means that they are unable to do detailed investigations of domain behavior in time. For scanning methods, the probe head must be scanned across the entire area twice before any changes in domain structure can be found. This process can take up to seconds for micron scale images. Imaging nanoscale phase domains with the intent of discussing emergent phase separation is not desirable, as at that scale it is impossible to rule out chemical segregation.

The first observed example of electronic phase separation came in 1955 from neutron scattering experiments that showed evidence of ferromagnetic metal (FMM) and antiferromagnetic insulator (AFM-I) electronic phases coexisting in $La_{1-x}Ca_xMnO_3$ bulk crystals[40]. The data showed large scale inhomogeneity on the order of 100 nm, comprised of a never before seen arrangement of Mn spins divided into a charge ordered AFM phase and a disordered FMM phase.

More recently, improved sample synthesis and the evolution of advanced imaging techniques have allowed nanometer imaging of single crystal manganites. Transmission electron microscopy (TEM) was one of the first methods used in attempting to image single domains. Several interesting findings have been made using this method[29]. $La_{1-x}Ca_xMnO_3$ was found to have charge stripes of widths of roughly 3 nm. The proposed explanation for these stripes was that one component with a Jahn-Teller distorted octahedral surrounding Mn^{3+} ions and another component having a Mn^{4+} ion. This distribution of electronic phases was then attributed to quenched disorder—a relatively higher number of the La doping in one region than in the other.

Mesoscopic phase separation was reported in bulk $La_{y-x}Pr_yCa_xMnO_3$ by Uehara et al[4]. Using TEM, they observed large regions of different electronic character coexisting with domain sizes on the order of 100 nm, and assigned the regions of different contrast as FMM and COI. They used this finding to propose that LPCMO's CMR was a direct result of electronic phase separation and explained the behavior through a hopping model in which the transport across the entire sample was dictated by the spin alignment in the FMM domains. Thus, the application of a magnetic field would act to align the FMM spins which would then allow the conduction electrons to hop more easily [Figure 1-10]. They concluded from this that phase separation was the key to CMR.

A competing interpretation was published soon after when scanning tunneling spectroscopy (STS) was used to investigate the metal-insulator transition in $La_{1-x}Ca_xMnO_3$. This study found that the application of a magnetic field actually reduced the volume of the insulating domains while increasing the volume of the metallic domains[39] [Figure 1-10]. This consequence was also able to explain the sharp drop in sample resistance under applied magnetic field. However they were in agreement with Uehara that phase separation was the likely cause of CMR in the material.

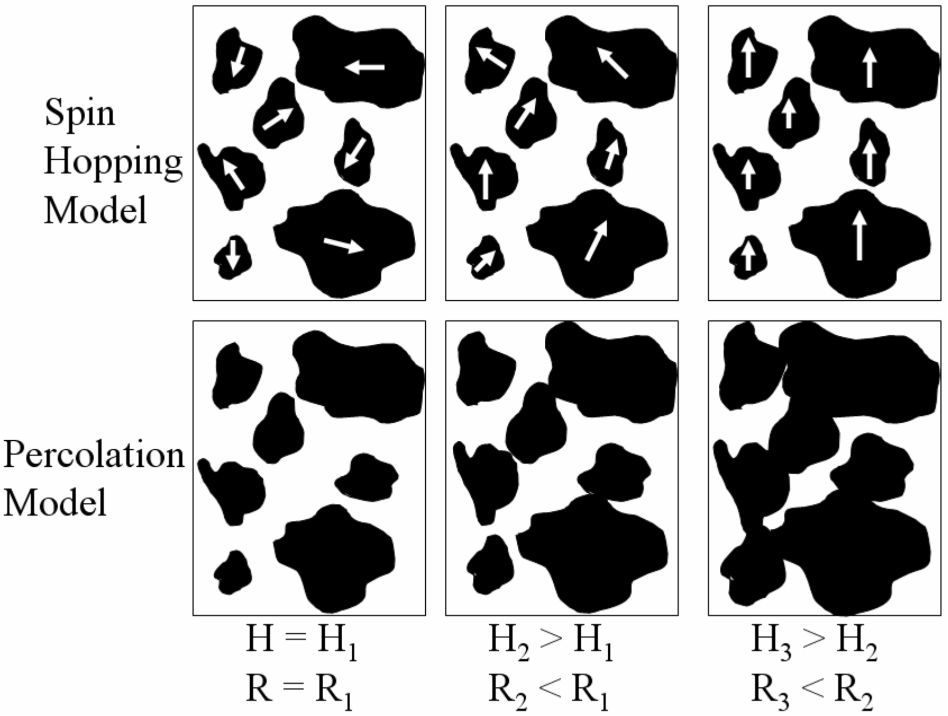

Figure 1-10: Conceptual diagram of spin model and percolation model. The dark areas represent metallic regions and light areas insulating. For the hopping model, an increase in the applied magnetic field aligns spins of metallic domains which lowers the resistance. In the percolation model, an increase in the applied magnetic field increases the size of the metallic domains at the expense of the insulating domains. Both of these models rely on the existence of phase separation to explain the observed colossal magnetoresistive response.

Observable electronic phase separation in cobaltates and high T_C cuprates has also been reported. $La_{1-x}Sr_xCoO_3$ was once thought to be a long range ordered conducting ferromagnet. However, more recent studies using Mossbauer spectroscopy have proposed that the order is not long range and that its metallic behavior could be based on phase separation into large metallic clusters and small insulating clusters[41]. Phase separation in the cuprate superconductors has also been widely investigated using STM[42,43] and neutron diffraction[44,45]. In this system, the phases are said to be separated by compositional variations in the oxygen doping which create superconducting clusters and AFM clusters. There is also evidence that chemically disordered (alloyed) systems in this class posses charge stripes and an inhomogeneous superconducting gap[2,46,47].

In Figure 1-11, we see two recent examples of data proposing direct observation of electronic phase separation. Both of these examples are for LPCMO. Figure 1-11a is taken using TEM on a bulk sample and shows clear regions of metallic(black) and insulating(white) regions on the scale of one micron[4]. Figure 1-11b shows a similar doping of LPCMO but in thin film form taken using MFM[48]. The image from Zhang shows the temperature vs. resistivity plot on warming and cooling and gives MFM images for select temperatures along these curves. What is so striking in these images is that we can see large regions apparently shifting their magnetic properties across the MIT. By comparing this phase information with their location on the transport plots, the authors speculate that we can see that the metal-insulator transition is aligned with the opening of conduction lanes in the film. Similar to those seen in bulk, the areas of differing contrast are on the order of one micron. If indeed these findings are imaging large scale electronic phase separation accompanied by such a pronounced MIT, this material would be a prime candidate for reduced dimensionality transport studies.

All of the above studies that propose to image emergent large scale electronic phase separation have drawbacks that make their results less than conclusive. To study emergent electronic phase separation it is vital to select a material that exhibits mesoscopic phase separation, as there is no growth method that is capable of growing perfect locally chemically disordered single crystals—statistically there is always the

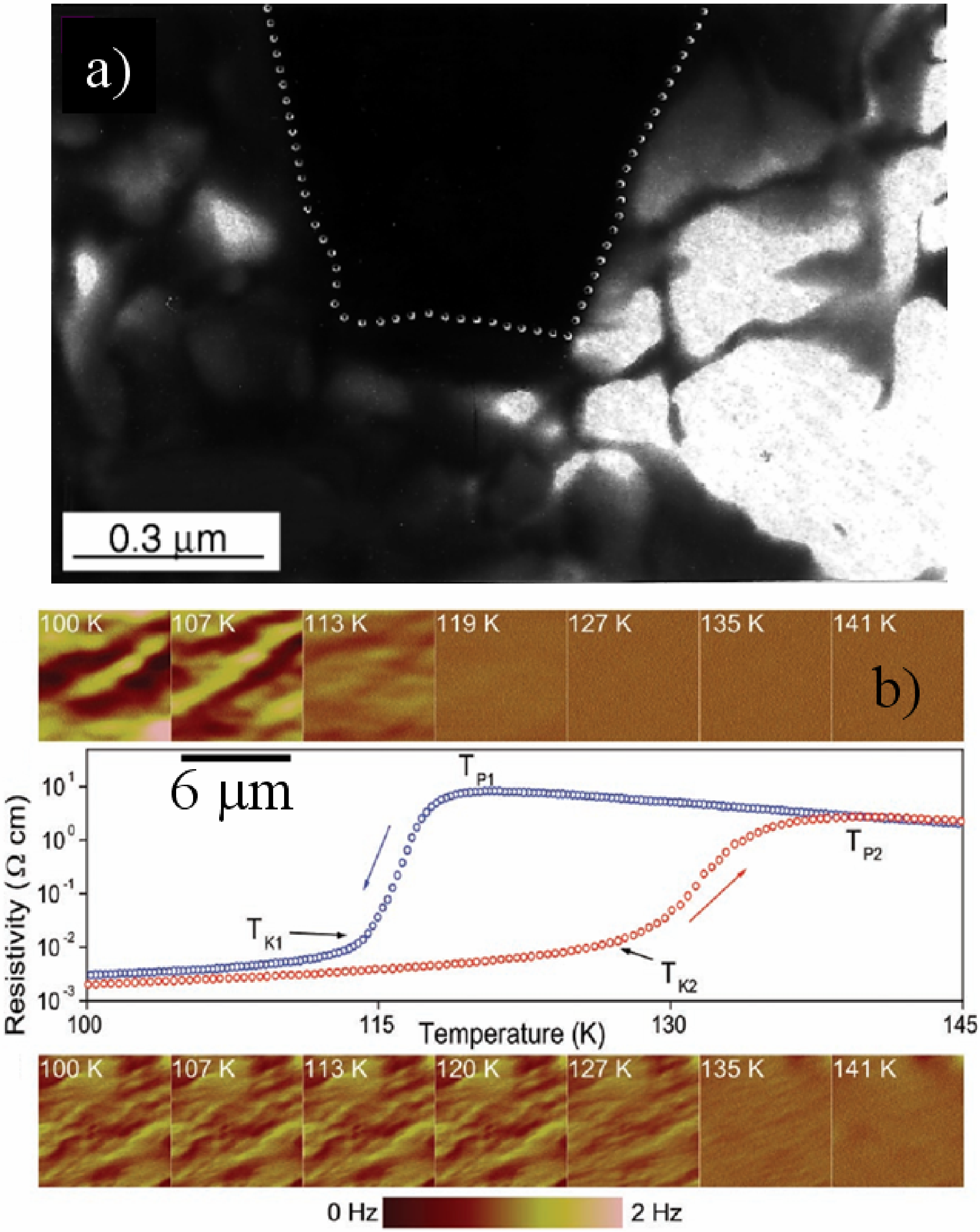

Figure 1-11: Direct observations of electronic phase separation. (**a**)TEM image of bulk LPCMO phase separation--Reproduced from Uehara, et al[4] with permission from Nature Publishing. (**b**)MFM images showing surface phase separation as it evolves with temperature--Reproduced from Zhang, et al[48] with permission from AAAS Publishing.

possibility of chemical segregation at nanometer scales. Above mesoscopic scales, chemical segregation can be ruled out as the foundation of observed domains, as several growth methods are available which can grow chemically disordered single crystal materials on this scale.

All of the scanning methods used to image surfaces can be questioned due to the fact that a material's surface is often quite different from its 3D properties, so surface studies are not the best method to prove the presence of phase separation. The perturbation attributed to the sudden termination in the periodic potential at the surface has been shown to make manganite surfaces behave differently than bulk[49-52]. TEM studies are limited by the fact that the images that they produce can not be quantified in a way that proves the presence of distinct electronic phases. Neutron diffraction, Mossbauer spectroscopy and other methods that have a large averaging component are also unsuitable for studying the dynamics of single electronic phase domains precisely because their results are based on averaging over areas larger than the inherent domain sizes. Measuring electronic transport is superior to surface scanning techniques, as the electrons travel through the sample thereby probing more than just the surface. However, transport measurements rely on averaging and are limited in that in an electronically phase separated material the probing current will follow the path of least resistance thereby leaving regions of high resistance invisible. If however we could somehow force the electrons to interact with both high and low resistance regions when both were present in a material, we could gain valuable insight into when, where and how emergent phase separation manifests itself in complex materials.

Chapter 2 Experimental Methods

2.1 Thin Film Growth

2.1.1 Overview of Methods

The most import part of any experimental work is the quality of the sample being studied. In transition metal oxides this is especially true, as the complex nature of these materials and their characters' dependence on charge, lattice and spin mean that even small deviations away from the intended crystalline structure and stoichiometry can create huge variations in the material's behavior. Even a single atomic variation can have a far reaching impact on the local lattice characteristics. The CMR effect was discovered over fifty years ago but was largely abandoned as an area of study until growth and characterization techniques matured enough to grow quality single crystal samples that could be investigated on the atomic scale. This chapter will discuss some of the growth techniques that have allowed these materials to return to the focus of many condensed matter physicists; we will also discuss our specific experimental setup and conditions.

Many techniques for thin film and multilayer growth have been developed. The key to growing any atomically pure sample is to insure that the parent materials are pure and that the sample is grown under a high enough vacuum to insure that there is no contamination. Chemical vapor deposition is the most widely used method—used almost exclusively in industrial applications. While it is capable of growing large homogenous samples it is generally not used for basic research due to contamination concerns and an inability to grow a wide range of samples from many different classes. Thermal deposition is the oldest technique but is not suitable for atomically pure samples as it is traditionally done in low vacuum; however its modern incarnation of molecular beam epitaxy (MBE) which is done in ultra-high vacuum does work for layer-by-layer growth of atomically pure samples and is widely used in basic research. Another growth technique known as pulsed laser deposition (PLD) has been shown to grow chemically homogenous samples. In this method, a high intensity laser pulse is focused onto a parent target containing the desired stoichiometry of the sample to be grown. With each pulse of the laser, a small amount of the target is ablated. The material is turned into plasma and highly energetic gas. This is directed at a substrate onto which the desired sample is to be grown. For a full review of PLD see Chrisey *et al*[53] and references within.

2.1.2 Laser Molecular Beam Epitaxy

The samples studied in this dissertation were grown using a slightly modified version of PLD known as laser molecular beam epitaxy (laser MBE). The main difference between PLD and laser MBE is with the energy of the applied laser pulse. Whereas, PLD uses laser energies high enough to create plasma, laser MBE uses a slightly lower laser fluence which ensures that the material ejected from the target is an energetic gas but does not enter the plasma state. This is particularly important for complex transition metal oxide growth, as in the plasma state the constituent materials are stripped of their electrons which translates into the growth on the substrate being more likely to enter an undesired growth mode and produce a rougher surface. With laser MBE, the parent elements are ejected at high enough energy to stick to the substrate with their ionic properties intact.

The sample preparation chamber used to grow samples presented in this dissertation will now be presented. Owing to the extreme sensitivity of TMOs to atomic doping, it is necessary to ensure that only the desired compounds are present during growth. To accomplish this, all growth is done in an ultra-high vacuum (UHV) chamber with a base pressure 1 x 10^{-10} Torr. For perspective, this is about the same pressure as that experienced on the surface of the moon[54]. Attached to this chamber, there are several key components: a reflection high energy electron diffraction (RHEED) system, a KrF excimer laser, a sample heater, an ozone source and a control computer [Figure 2-1].

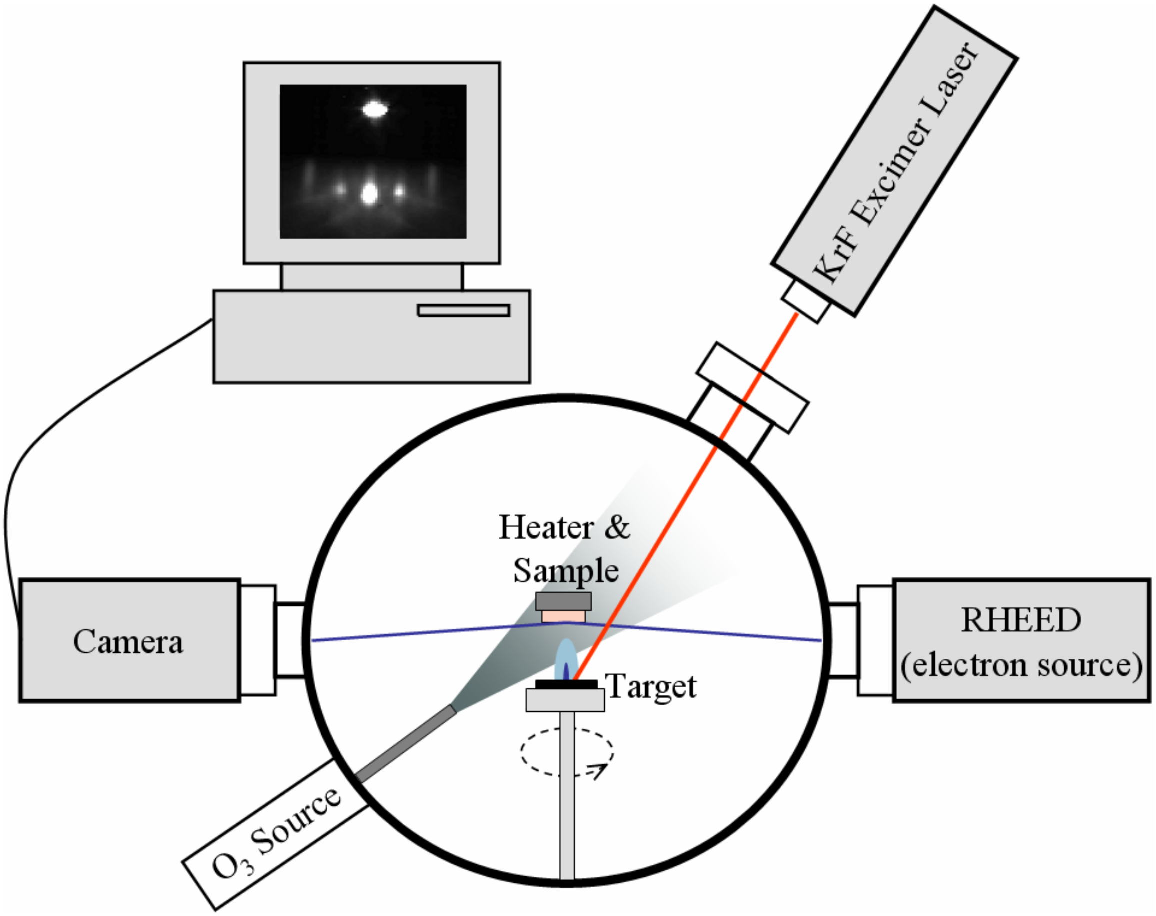

Figure 2-1: Schematic of laser molecular beam epitaxy system.

The excimer laser gets its name from the combination of the words excited dimmer. When an inert gas and a reactive gas—in our case Kr and F—are combined and energized in a large electric field, they create a highly energized pseudo-molecule with a metastable electron band in the ultraviolet region. This type of laser is widely used for eye surgery, semiconductor manufacturing and other applications where high energy photons are needed to ablate surfaces without damaging the underlying structure. Their high power allows for very short bursts to have great effect without unwanted heat transfer. The excimer laser that we use is a Lambda Physik model with an output wavelength of 248 nm and pulse duration of 30 ns. We optically focused the beam to a spot size of about 1 mm^2 which gives a fluence of about 1 J/cm^2. By adjusting the optics, we are able to tune the fluence and thus adjust the power/area administered to the target.

2.1.3 Target Preparation

The targets are created by mixing parent compounds, pressing and annealing. As an example, if we would like to grow a thin film of $La_{5/16}Pr_{5/16}Ca_{3/8}MnO_3$, we are first required to make a stochastically matched target. To do this, we start by mixing La_2O_3, Pr_6O_{11}, $CaCO_3$ and MnO_3 in proper proportions. In order to find the correct ratios of parent compounds, we need to balance the chemical equation and then mix the desired amount of each material.

$$(3)La_2O_3 + (1)Pr_6O_{11} + (6)CaCO_3 + (6)MnO_3 = (6)La\ PrCaMnO_3 + (6)CO_2 + (10)O_2$$

After doing this, we find that we are given LPCMO with by-products of carbon dioxide and oxygen. Next, we calculate the amount of the parent materials that need to be mixed. This is done by taking the product of the desired doping concentration, the molar mass the parent compound and the molar multiplier found in the balanced chemical equation.

$$La_2O_3 \Rightarrow (5/16)\bullet(325.8\ \mathrm{g/mol})\bullet(3\ \mathrm{mol}) = 305.4\ \mathrm{g}$$
$$Pr_6O_{11} \Rightarrow (5/16)\bullet(1021.4\ \mathrm{g/mol})\bullet(1\ \mathrm{mol}) = 319.2\ \mathrm{g}$$
$$CaCO_3 \Rightarrow (3/8)\bullet(100.1\ \mathrm{g/mol})\bullet(6\ \mathrm{mol}) = 225.5\mathrm{g}$$
$$MnO_3 \Rightarrow (1)\bullet(86.9\ \mathrm{g/mol})\bullet(6\ \mathrm{mol}) = 521.2\ \mathrm{g}$$

This gives us the proper ratio of mass for each compound to include in the target. After careful measurement, the materials are mixed using mortar and pestle for 30 to 60 minutes or until there is a uniform consistency and color. The mixture is then pressed into disk pellets and annealed in an oxygen environment of about 1.2 atm at 1100 C for 12 hours. After a second mixing and annealing process to ensure proper integration of all materials, the target is ready to be placed in the chamber.

The UHV chamber allows for up to four targets to be placed on a rotating target holder at one time. This reduces the need to vent the chamber to put in new targets and allows us to grow multilayer materials. The target carousel also allows us to control target spin which ensures an even ablation of the target.

2.1.4 Reflection High Energy Electron Diffraction

The RHEED system is used to monitor layer-by-layer growth and surface quality. Here an electron beam is reflected off of the growth surface and collected on a phosphor screen. A camera collects the image from the screen and transfers it to a computer which monitors pixel intensity. By monitoring the intensity of the reflected electrons, it is possible to observe layer-by layer growth. Figure 2-2 is a representation of progressive stages of a single monolayer growth. From top to bottom, we see that as a layer is being grown the reflected spots in the RHEED pattern change. The second order spots are weakest when there is a half unit cell of growth—the less intense the spots, the rougher the surface. By looking at the intensity of the spots, we can estimate how close to a single unit cell has been grown. Figure 2-2 shows what a typical intensity plot of the second order spot would look like during growth. Each oscillation represents one completed unit cell. The three intensity fluctuations (high to low to high) represent three layers.

The RHEED works by collecting electrons that have reflected from the surface of a material. The diffracted electrons constructively interfere at specific angles. These angles are dependent on the crystal structure (size and spacing of atoms) at the surface and the wavelength of the incident electrons. Both dynamic and kinetic scattering take place; though we are only concerned with the kinetic scattering that takes place when an incident electron undergoes a single elastic scattering event on the crystal's surface. It is the constructive interference from these events that are observed on the phosphor screen and analyzed by the computer. They can be treated as typical Bragg diffraction. Another valuable use for RHEED is in analyzing the growth mode.

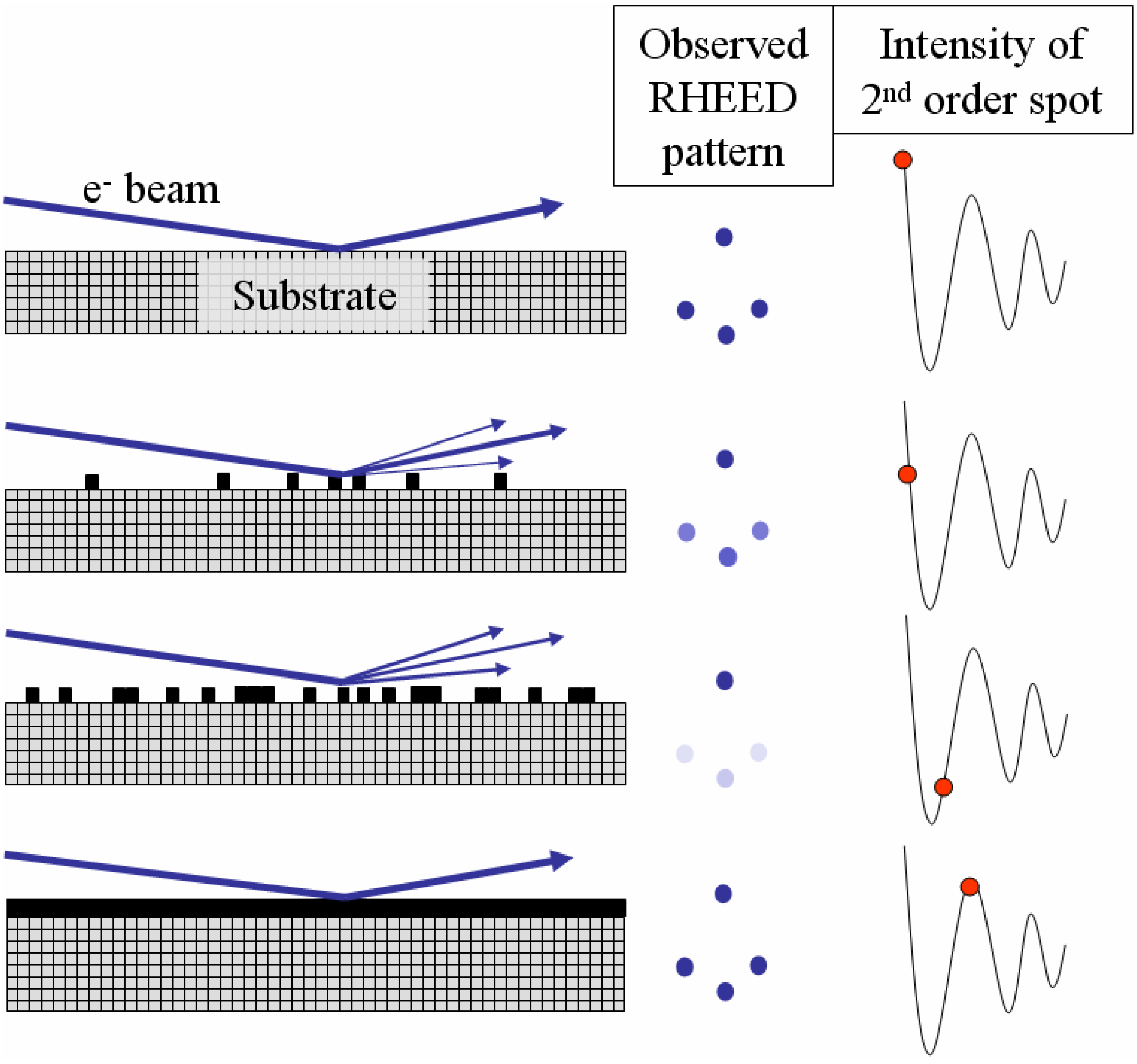

Figure 2-2: Diagram of RHEED data for progressive stages of single monolayer growth.

2.1.5 Growth Modes

Figure 2-3 shows examples of three growth modes. Under perfect growth conditions step-flow growth can be achieved. In this mode, adatoms seed along the step edges and uniformly move across the substrate surface. The RHEED images for this mode show a constant intensity in the second order spots throughout the growth. This mode gives the best quality films however judging the growth thickness can be difficult due to the lack of fluctuation in RHEED intensity. The example given in Figure 2-2 is step-flow with 2D islands. In this growth mode, some islands can seed on the step plateau while growth continues to cover the substrate in a 2D sweep. This method is the most commonly observed mode when growing lightly strained films over the first few monolayers. From this, it is possible to record the number of laser pulses required to form one unit cell thickness. This will ensure that if the growth mode switches to step-flow it is still possible to control film thickness. One danger of this mode is that step bunching can occur if an island relaxes or tilts and meets a step edge. Finally, under less than ideal growth conditions, 3D islands can form on the step plateaus. This creates a very rough surface and possible step bunching. The RHEED images from samples grown in this mode will show many spots as the different levels from the islands will create a much more complicated diffraction pattern. There is no fluctuation in intensity if the sample is left to grow in this mode too long. Since the majority or our work focuses on basic research requiring nearly perfect sample epitaxy and surface flatness, we typically discard samples that enter this mode, as the large islands add further complexity to the system in the form of step bunching, increased surface relaxation from roughness and imperfect thickness.

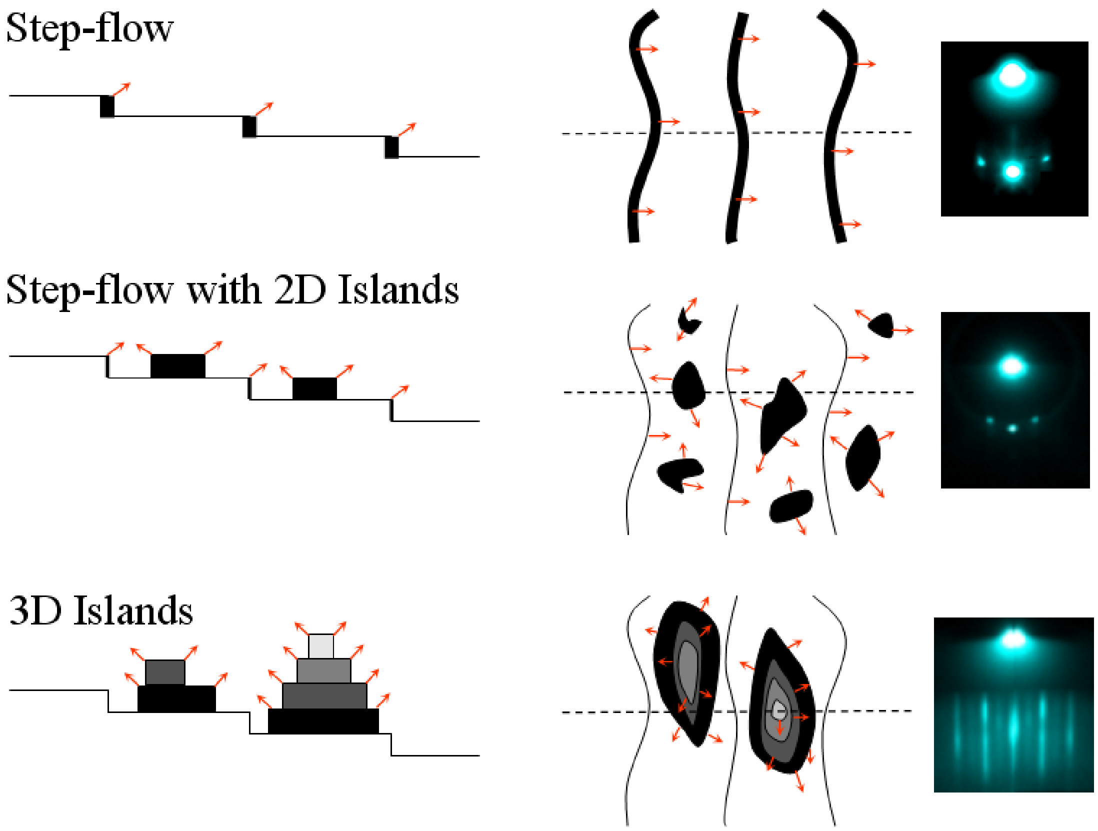

Figure 2-3: Examples of 3 growth modes and their RHEED signatures. Left column shows side view taken at dotted line in middle column. Red arrows indicate direction of growth. Right column shows typical RHEED images for each growth mode.

2.1.6 Growth Parameters

To this point we have not discussed three very important growth parameters that must be carefully tuned for good film growth. The first is sample temperature. To control this, we mount the substrate onto which the film will be grown on a home build heater. The heater is made of wound Ta wire—though recently we have switched to Pt due to its lower likelihood of oxidation—encased in a low out-gassing ceramic. The temperatures needed for sample growth vary from between 760 C for LSMO to 825 C for LPCMO. Another important factor is the application of ozone during growth. This has two effects. Manganites are susceptible to oxygen deficiency due to the high growth temperature, so adding reactive oxygen helps to fill these holes. Also, by tuning the pressure of O_3 in the chamber it is possible to change the kinetic energy of the target gas as it travels to the sample. Generally, the pressure is held between 3 x 10^{-5} Torr to 1 x 10^{-4} Torr. Finally, an often overlooked setting is the target to sample distance. To change this setting the chamber must be vented and the target carrousel adjusted. This setting can be somewhat counterbalanced with O_3 pressure during growth but should never be closer than about 4 cm and never further than 6 cm.

While we strive for perfect film epitaxy and surface flatness, we have found that it is possible to create self-organized structures on the surface under certain growth conditions. Figure 2-4 shows optical microscopy images of several examples of self-organized surface structures. Figure 2-4a is a high quality crystal with no large surface structures. By increasing the temperature 30 to 40 C above optimal growth temperature and reducing the ambient O_3 pressure, small micron scale dots organize into parallel stripes along the surface [Figure 2-4b]. Under growth temperatures 50 to 80 C above optimal growth conditions, it is also possible to seed long rods hundreds of microns in length [Figure 2-4c]. These rods are often found near the clamped edge of the substrate suggesting that they are influenced by surface strain induced by the uneven pressure applied by the clamps. Damage to the growth surface can also be used to seed dot formation. In Figure 2-4d, the substrate was mechanically scratched prior to growth which caused dot formation along the defect line. In this scenario, the dots do not align along the underlying crystalline structure into parallel or perpendicular lines; instead they follow the damaged region of the substrate. Initial studies with XPS on these structures seem to indicate that they have the same composition as the film. It might be possible to remove these structures from the growth surface. This could have possible uses for applications and should be further studied.

Once all settings are made, the sample growth is fully automated through a home built Visual Basic driver that controls laser pulse rate, laser energy, target spin, selected target, growth times, and anneal times. The source code can be found in Appendix A. It is necessary to balance all of the growth parameters to ensure a quality sample. Specific details for each experiment presented in this dissertation will be given in the chapter dealing with experimental results.

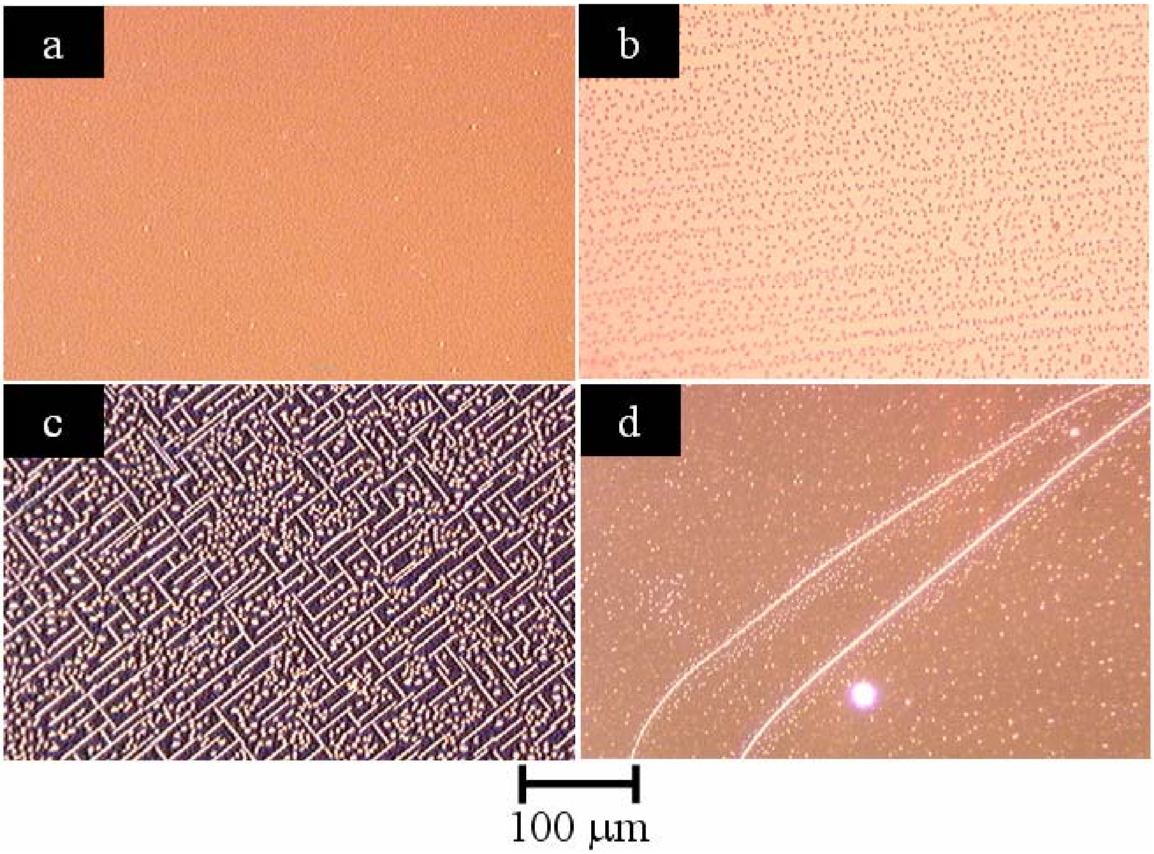

Figure 2-4: Self-organized macroscopic surface structures. (**a**)Typical film surface at optimal growth conditions. (**b**)Micron size islands in a lateral alignment. (**c**)Large self-organized wires and dots. (**d**)Surface defect seeding dots.

2.2 Characterization Methods

2.2.1 Scanning Tunneling Microscopy

Scanning tunneling microscopy (STM) is a well developed method of imaging surfaces with atomic precision. Developed in 1981 by Binnig and Rohrer at IBM, it took only 5 years for their work to win a Nobel Prize in Physics which speaks to the immediate importance that this technique found in science[55]. The STM does not image the true location of atoms; instead it probes the density of states of a material at its surface. This means that it is actually imaging the electronic structure. Resolutions of 1 angstrom in-plane and 0.1 angstrom out-of-plane are fairly standard in vacuum.

A modern STM is comprised of several components: an atomically sharp conducting tip, a piezoelectric controlled 3-axis scanner, a coarse sample-to-tip controller, a vibration isolation stage and a control computer. An atomically sharp tip of conducting metal is needed for good image quality. We generally use electrochemically etched tungsten. The resolution of the image is directly limited by the radius of curvature of the scanning tip so the sharper the tip the better the image. Vibrations within the system can ruin image quality. This negative contribution can be greatly reduced by isolating the sample stage from the surrounding environment; this is generally accomplished with fairly simple spring systems. The computer also plays an important role in generating quality images. It is used to raster the tip with high accuracy, acquire data and process images.

The mechanism that STM relies on is quantum tunneling. By applying a voltage between an atomically sharp conducting tip and a metallic or semiconducting surface, quantum tunneling can occur if they are brought near enough to each other (figure 2-5). The electrons tunnel though the energy barrier created by the tip-surface gap. The number of electrons that make the jump across the tunnel can be tuned by bringing the tip closer to the surface or increasing the bias. The resulting current is related to a sample's local density of states at the Fermi level. Scanning the tip across the surface gives an image of the electronic properties of the material not the physical structure. There are two scan modes that can be used.

Constant height mode holds both the height and bias constant while the current is measured with x and y positions to form an image of charge density across a surface. This mode is relatively fast as current can be measured more quickly than piezo position.

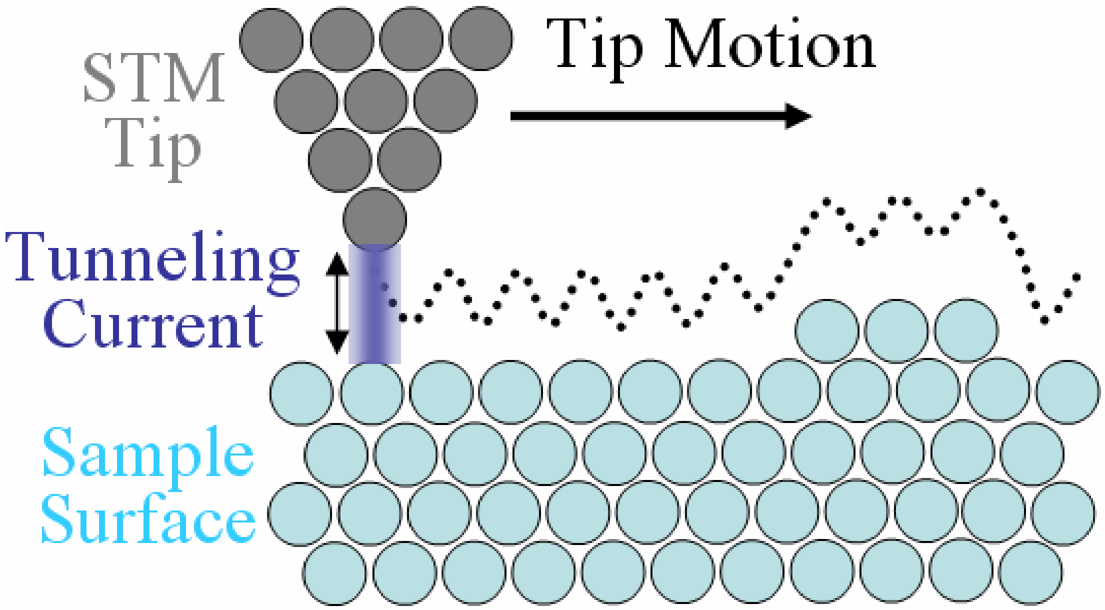

Figure 2-5: Diagram of STM surface imaging.

Constant current mode is used to image *variations* in charge density across a surface. In this mode, the STM electronics adjust the tip distance to maintain constant current as the tip is scanned. This gives an image based on height variations where the differences in image are due to the change in the current as the tip moves across the surface.

A fairly new application of the STM is in the form of a 4-probe STM. The main use of this system is to do nanoscale transport measurements. With atomically sharp tips, it is possible to directly measure nanoscopic features' transport properties. Figure 2-6 shows the circuit diagram for a constant current 4-probe transport measurement and its relation to probes in an actual experiment. From the SEM image, we see that the geometry is the same as for any 4-probe transport measurement with sourced current on the outer probes and measured voltage across the inner probes. In electronic phase separated materials, the ability to selectively probe different areas of the sample is quite powerful. Studies are currently underway placing phase separated materials at the MIT to determine whether it is possible to probe individual domains and across domain walls. This technique might also make it possible to map domains as they seed and annihilate.

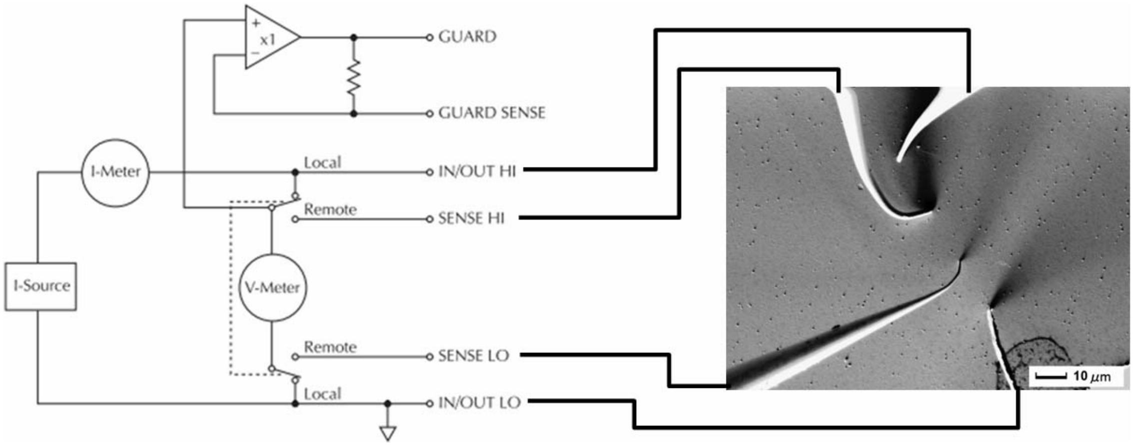

Figure 2-6: Circuit diagram of 4-probe STM transport measurement.

2.2.2 Atomic Force Microscopy

Another scanning probe method for surface characterization is atomic force microscopy (AFM)[56]. Though having the word "microscope" implies something visual, the AFM actually images through mechanically interacting with a surface. A cantilever of many microns with a probe tip having a radius of curvature of several nanometers can be used to *see* a surface when brought near enough to it. What makes the AFM useful to many fields of study is that the probe tip can interact with the surface through many different forces. For our studies, Van der Waals force and magnetic force are of interest; however capillary forces, chemical bonding forces and electrostatic forces can also be detected with this method. This versatility is possible since the tip can be coated in materials with different reactive properties and the cantilever can function in an aqueous solution as well as in air or vacuum.

Figure 2-7 shows a block diagram of a typical AFM setup. When the tip is brought close to the sample surface, the cantilever will deform. Its deflection is the result of the forces between the tip and surface as discussed above. To measure the bending of the cantilever, a laser is reflected off of the cantilever's surface and focused on an array of photodiodes. The cantilever's deflection can then be recorded on a computer. There are two primary modes of scanning a surface—contact mode and dynamic mode.

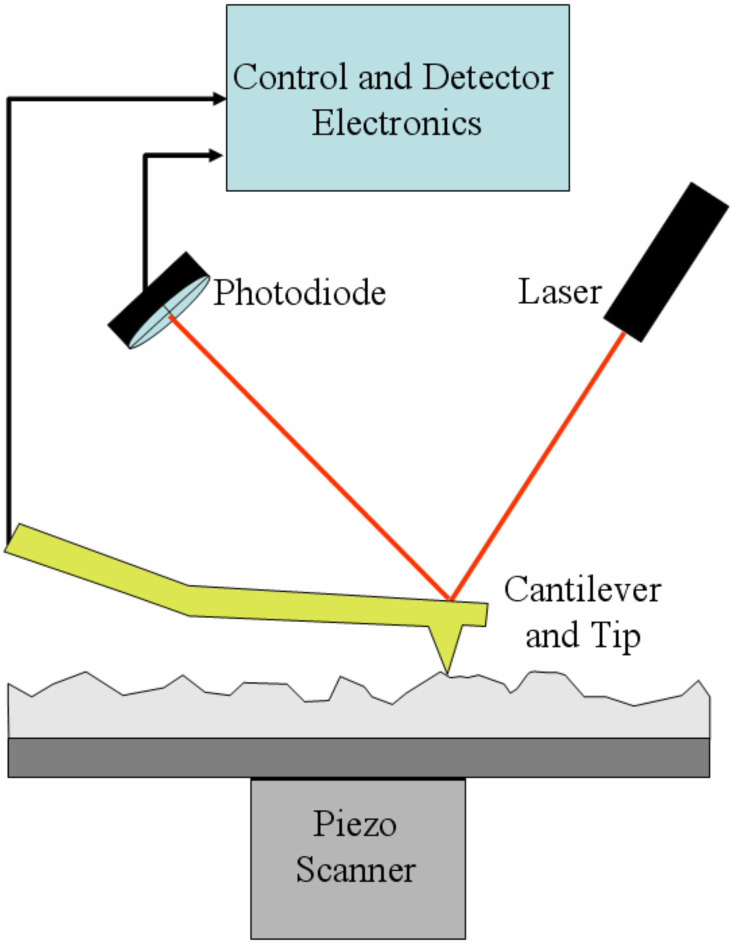

Figure 2-7: Diagram of AFM in contact mode.

In contact mode, also called static mode, the static tip is used as a feedback signal. Its deflection is measured as the surface interacts with the tip. To reduce the risk of the tip snapping into contact with the surface, it is best to use this mode when the forces are repulsive. The force between the tip and surface are held constant as the cantilever bends to maintain a constant force. This method uses a fairly flexible cantilever and is prone to tip damage.

Dynamic mode uses stiffer cantilevers so can operate much closer to the sample surface and is the better option for high resolution imaging in UHV. Here the cantilever is oscillated at its resonance frequency. As the tip and surface interact, the resonance frequency, phase and amplitude change. By analyzing these changes as compared to an external reference oscillation, it is possible to extrapolate surface structure. Since frequency modulation can be measured with a high resolution, frequency differences are most commonly used as a measure of surface structure. Amplitude modulation can be combined with changes in the phase oscillation to recognize different types of material on a surface.

2.2.3 Magnetometry

Determining a sample's magnetization is accomplished using a superconducting quantum interference device (SQUID). Specifically, we use a Quantum Design MPMS. Due to the small volume of our samples and the inherent need for precision, this model has several key features that make it ideal for our purposes. It can apply magnetic fields of up to ±7 T with a precision of ±0.05 G, has a stable temperature range between 5 K and 400 K, and has a sensitivity of 2×10^{-8} emu.

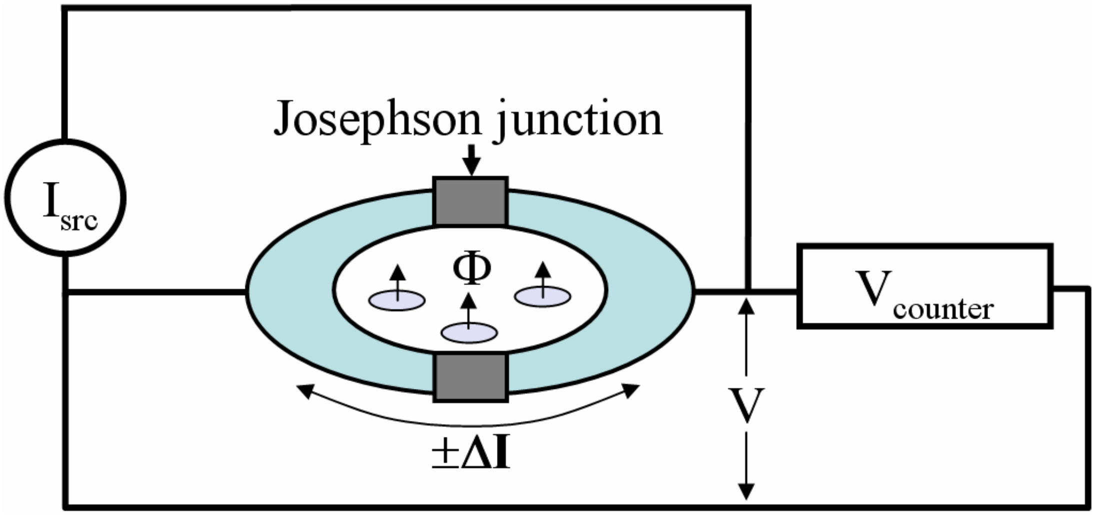

Figure 2-8: DC Superconducting quantum interference device (SQUID).

Figure 2-8 shows a simple diagram of a SQUID. The system is based on two half rings of a superconducting material joined by Josephson junctions (JJ). A JJ is an insulating bridge that connects two superconductors. In these devices a current will tunnel through the junction when there is no applied voltage. When a voltage is applied, the current will decrease and oscillate proportionally with the voltage. The relationship between oscillation frequency and applied voltage is so precise that it is now the measure by which the standard volt is defined. By placing these devices into a ring configuration, any change in the central magnetic field will have a very noticeable effect on the signal voltage.

Driving a constant sourced current across the ring parallel to the JJ will give a system in which the current across each junction will be equal when there is no applied magnetic field and thus no voltage will be read at the counter. Any value of magnetic flux (Φ) can be applied, but only a multiple of the flux quanta is able to pass through the ring opening. A single flux quanta is defined as $\Phi_0 = h/(2e) = 2 \times 10^{-7}$ G cm^2, where h is

Planck's constant and e is the electron charge. This is the case due to the fact that excess, non-multiple flux will be cancelled by the fractional flux quanta created by the circulating current traveling around the ring. So by linearly changing the flux passing through the ring the circulating current will react with a sinusoidal signature. The change in current is detected by the counter in the form of voltage pulses. Every voltage peak equates to an increase in one flux quanta. This is what makes this device so incredibly sensitive to magnetic fields. By holding the flux constant and passing a sample through the ring, the material's magnetization can be found easily.

Here we will discuss some types of magnetism and their signatures in the SQUID. Diamagnetism is the most common behavior and is manifested as having a magnetization proportional and opposite to the applied magnetic field. This is a very weak form of magnetism and is explained by the response of orbiting electrons to Lenz's law—induced emf and flux change have opposite signs. This type of magnetism shows no hysteresis on field cycling since it is non-permanent and is only present when there is an applied magnetic field. All materials show some degree of diamagnetism.

More interesting magnetic behaviors can be found in material systems that have magnetic properties based on unpaired electron interactions. These are particularly interesting in the study of the manganites as these forms are typically found in transition metals and lanthanides stemming from their unpaired d and f electrons. There are three specific types that we will focus on [Figure 2-9]. Paramagnetism has randomly arranged unpaired electrons. Ferromagnetism has aligned unpaired electrons. Antiferromagnetism has neighboring unpaired electrons aligned opposite to one another.

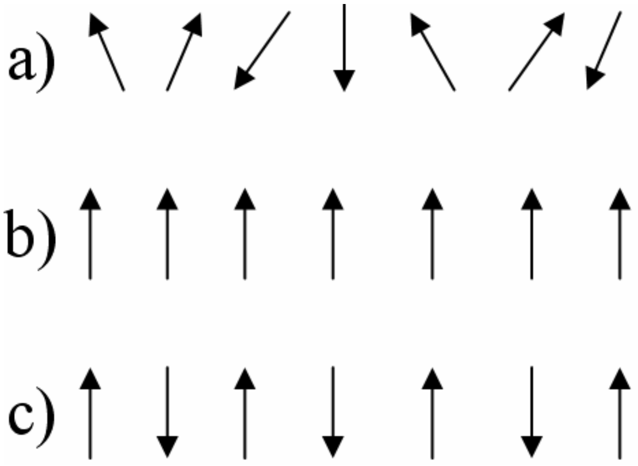

Figure 2-9: Types of magnetism in unpaired electronic systems. (**a**)Paramagnetism. (**b**)Ferromagnetism. (**c**)Antiferromagnetism.

Paramagnetic materials are similar to diamagnets in that they have no hysteresis response. They differ in that their magnetization is proportional to and reinforced by the applied field. This effect is caused by non-coupled dipoles in the material. Ferromagnetism has the largest magnetization. This type of magnetism is caused by strong coupling between magnetic dipoles in a material. They can be recognized by a sharp change in magnetization at a specific temperature known as the Curie temperature (T_c)—the temperature above which thermal energy is high enough to break the coupling between neighboring dipoles. Ferromagnets also possess a remnant magnetization that can be recognized as a hysteresis in field scans taken below T_c. This remnant magnetization can be overcome by applying a high enough coercive magnetic field to break coupling and force alignment into a paramagnet-like behavior which can also be a useful piece of information. Finally, there is antiferromagnetism. This type also has a critical temperature—the Neel temperature—and can be overcome by a coercive field however it differs from ferromagnetism in that the dipole couplings between moments act to balance each other through ordering their direction opposite to their neighbor instead of inline as with the ferromagnets. The magnetic susceptibility of an antiferromagnet will typically be at a maximum at the Neel temperature before it transitions to a paramagnet—diverging in a stepped fashion once past the transition. A ferromagnet's susceptibility will diverge instantly at T_c as it transitions to a paramagnet.

2.2.4 X-ray Diffraction

X-ray diffraction (XRD) is used to determine a sample's overall crystalline properties[57]. X-rays are photons of much shorter wavelength and much higher energy than what we are able to see with our eyes. What makes X-rays so useful in determining crystal structure is that their wavelength is generally on the same order as crystal lattice spacings. As photons, they can be treated using Bragg's law—even though Bragg himself argued that X-rays were not electromagnetic radiation[58]. Bragg's law is defined as $2d \sin(\theta) = n\lambda$ where d is the spacing between atoms in a lattice, θ is the angle between the incident beam and the scattering plane, n is an order determined integer, and λ is the wavelength of the incident photon [Figure 2-10].

When an atom is struck with X-rays, the atom's electron cloud is perturbed. As the cloud normalizes, it reradiates waves with the same frequency as the incident photon which is referred to as Rayleigh scattering. In essence, the lattice forms an array of point light sources, each radiating spherically outward. This allows us to treat the crystal as a diffraction grating. The reemitted waves constructively or destructively interfere with each other as dictated by Bragg's law. In-phase sources will constructively interfere and

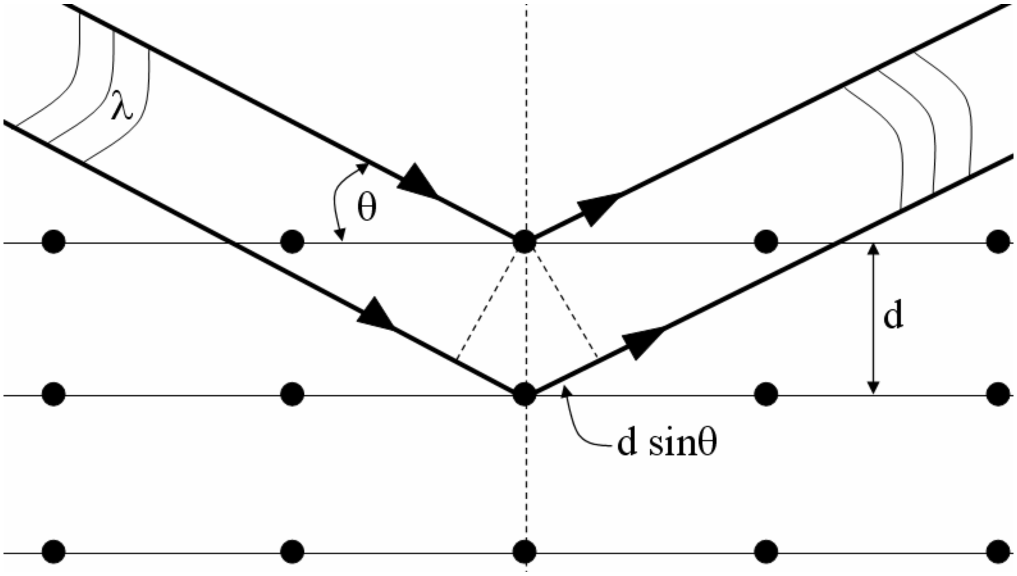

Figure 2-10: Bragg diffraction at sample surface.

out of phase sources will destructively interfere. From the diffraction pattern, we can then reconstruct crystalline structures.

An X-ray diffractometer has three primary elements: an X-ray source, a rotating sample mount and an X-ray detector. To produce X-rays, electrons are accelerated in a cathode ray tube toward a target. With high enough energy, the electrons will kick out inner shell electrons into highly excited orbits in the target material. As the electrons drop back to unexcited states, they release photons in the form of X-rays. The exact wavelength is determined by the target material. There is a spread in wavelength but the most common are K_α and K_β. To filter out other wavelengths and leave just these two, foil or crystal monochrometers are used. K_α and K_β are very close in wavelength and both pass the monochrometers; because of this, a weighted average is used during data analysis. For our manganite samples, we typically we use wavelengths in a range of 0.1 Å and 2 Å. This translates to an energy range of between 100 eV and 100 keV.

Once the monochromated X-rays leave the tube, they are directed toward the sample, Raleigh scatter outward, and are collected by the X-ray detector. Figure 2-11 gives an illustration of a 4-circle goniometer. The four circles refer to the four angles θ, χ, Φ, and Ω that dictate the relation between X-ray source, crystal lattice and X-ray detector. This setup essentially gives us the ability to look at any position within the diffraction pattern sphere. A typical pattern can contain thousands of unique reflections within that sphere created by the many different (*hkl*) planes within a sample crystal. The solution of a crystal structure's unit cell in real space can then be computed from the pattern's reciprocal Fourier transform.

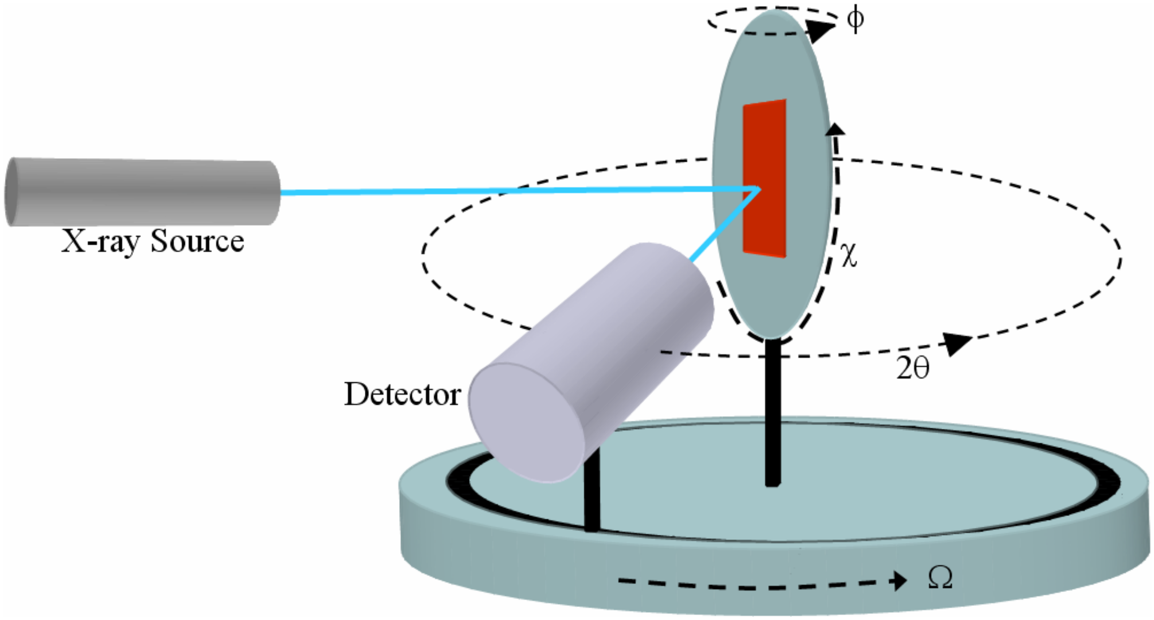

Figure 2-11: Illustration of 4-circle X-ray diffractometer.

We have been fortunate to also have access to the Advanced Photon Source at Argonne National Laboratory. This facility is capable of producing many orders more photons across a spectrum of X-ray wavelengths. Two beam lines have been of particular interest to us. On the 33BM beamline, a temperature control stage allows us to vary temperature from 300K to 77K. This combined with the monochromatic high intensity beam is allowing us to probe very thin manganite samples for structural phase transitions below T_c. On the 34ID beamline, a polychromatic incident X-ray beam can be focused to an area of a few hundred nanometers. This could be very useful in studying phase separation in manganites. It is well established that there is large scale electronic phase separation in these materials, but the role that local lattice distortions play (if any) in creating PS is less well understood. The microdiffration should be able help shed light on this question; a fuller description of these experiments is given in Chapter 4.1.

2.2.5 Transport Measurements

Manganites are highly sensitive to temperature and magnetic field. In order to investigate this behavior we need to be able to measure resistivity under variable magnetic fields and across a wide temperature range. This is accomplished using a Quantum Design Physical Properties Measurement System (PPMS) model 6000.

The PPMS can apply magnetic fields of up to 14 Tesla with a control resolution of 0.03 mT from 0 T to 1.5 T and 0.3 mT from 1.5 T to 14 T. We are also able to control temperature from 5 K to 400 K in standard mode and down to 1.9 K with the Helium-3 insert. Above 10 K, there is a temperature accuracy of ±0.02%. Below 10K, the accuracy is 0.2%. We can also access transport dependence on field direction using the sample rotator option. This add-on allows us to rotate the sample with respect field during measurements to determine easy-axis magnetic direction in samples. The PPMS uses the standard 4-probe measurement technique to calculate resistance. Figure 2-12 shows a diagram for this technique. The inner contacts are used to sense voltage while the outer contacts are used to source current. In this configuration, contact issues are eliminated.

Since we are interested in materials that show large electronic phase separation that can exhibit strong insulating behaviors, it is necessary to use contact pads on the sample surface that are larger than the inherent domains. This ensures that at the contact points there will be many transport channels open to view so that only the geometry of any spatially confined structures between the voltage pickups will dominate the measurement. To produce large, highly conducting pads, we evaporate 20 nm of Ti or Cr

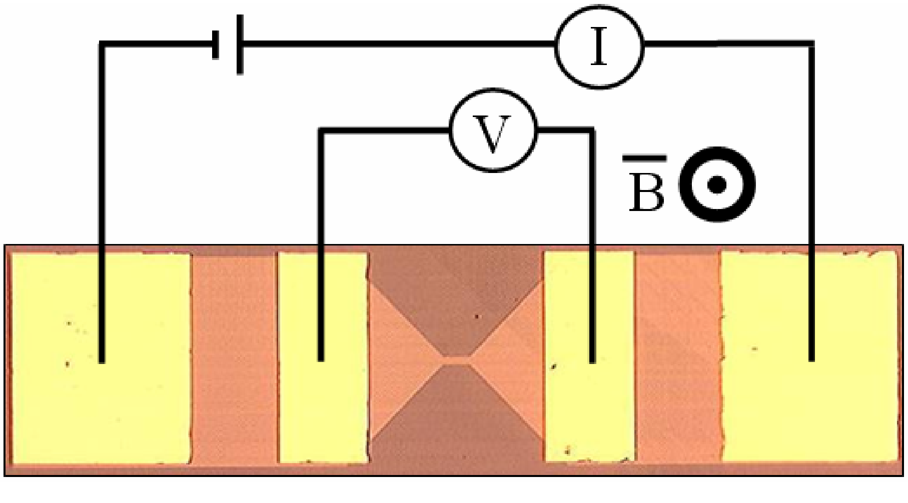

Figure 2-12: 4-probe resistivity measurement diagram.

as a buffer layer and then an additional 100 nm of Au. The buffer layer is necessary to help the Au adhere to the surface. It should be noted that magnetization and XRD measurements need to be completed before this step.

Once the pads are in place, the sample is placed on the PPMS sample puck. The puck has three sets of 4-probe contacts. The sample contacts are then wire bonded to the puck using Al wire. Once this step is completed the puck can be placed in the PPMS for measurement. While the PPMS offers a very nice set of control electronics that are capable of low noise and high precision in measuring resistance, it is not capable of high resolution time scans nor certain I-V measurements. For these measurements, it is possible to use a break-out box to connect external electronics to the sample.

2.3 Spatial Confinement Techniques

2.3.1 Overview and Motivation

By reducing complex materials to smaller scales, even well studied complex systems such as the manganites might exhibit new and unexpected phenomena. By employing novel lithographic techniques to spatially confine single crystals of phase separated materials to the scales of their inherent electronic phase separated (PS) domains, it could be expected that striking differences in the electronic transport properties should occur. The results of these measurements could allow us new insights into the underlying balance of spin-charge-lattice interactions while increasing our knowledge of the formation of and interplay between domains. Though this dissertation will focus on just a few PS systems, this technique should offer similar rewards on other

PS materials; and with the current trend of reducing device sizes, this type of study will be critical for applications as well.

Rare earth manganites exhibit CMR. There is general consensus that chemically disordered single crystal materials in this class can display electronic inhomogeneity in which areas with vastly different electronic and magnetic properties can form and coexist in phase separated domains ranging in size from a few nanometers to micrometers. This phase separation (PS) is of particular interest, as it has been suggested that it is the central feature that leads to CMR. However there is debate as to its importance and precise role.

The purpose of spatial confinement on PS materials is to answer fundamental questions about the specific role of PS as it applies to larger characteristics such as CMR. We expect to find new information on local and long range ordering effects with this technique, because it allows us to probe regions of different electronic properties that reside in the same material simultaneous. We reduce single crystal thin films of an electronically phase separated manganite to the scale of its inherent electronic charge ordered insulating (COI) and ferromagnetic metal (FMM) phase domains. Unlike transport measurements done on bulk or thin films where the electrons follow only the metallic path of least resistance, this configuration forces electrons to travel through both the metallic *and* insulating regions residing in the material [Figure 2-13]. This has led to observations of several new phenomena such as a reemergent metal-insulator transition[59], ultra-sharp jumps in resistivity at the metal-insulator transition[60], and the first high resolution observation of single domain phase transitions in time. These behaviors will be discussed in detail in the experimental results chapter.

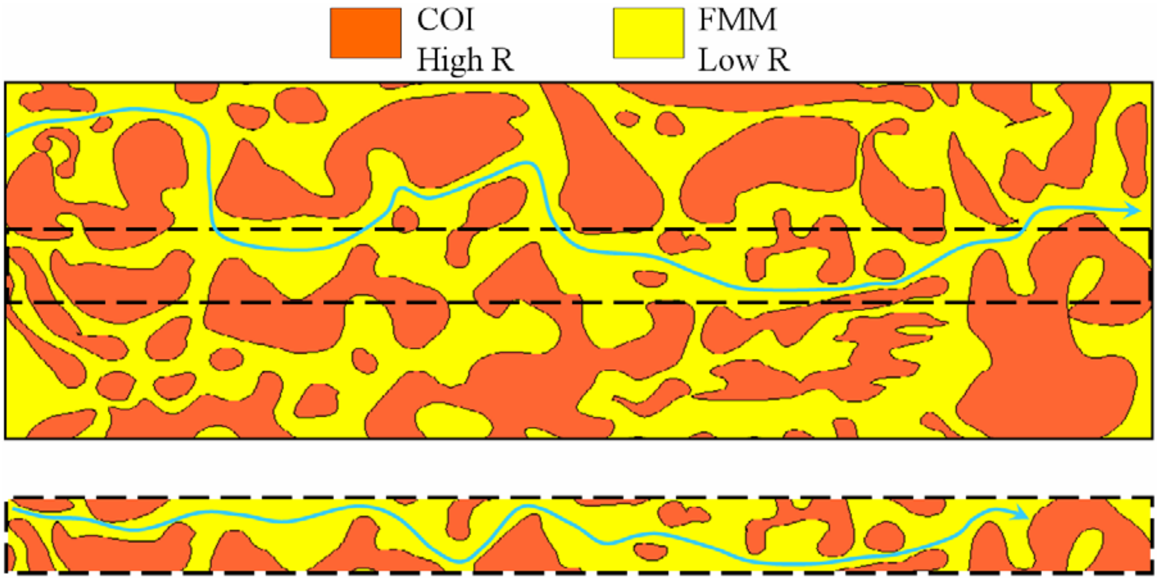

Figure 2-13: Comparison of conduction paths through PS film and PS wire. In this model, a reduced area creates fewer transport lanes for electrons to follow which forces probing of multiple regions. The blue lines indicate possible conduction paths.

There are several methods at our disposal to spatially confine thin films. These methods include: optical lithography, focused ion beam milling (FIB), electron beam lithography (e-beam), direct laser writing, and atomic force microscopy (AFM) lithography. These types can be broken down into three categories: 1) those that require a mask for photoresist development followed by etching to remove the developed region, 2) those that use directed photoresist development without the use of a mask followed by etching to remove the developed region, and 3) those that use direct mechanical means to shape the film into desired geometries.

2.3.2 Photolithography

The most widely used and fastest method to create confined structures is photolithography [Figure 2-14]. In this method, the single crystal film is grown on a

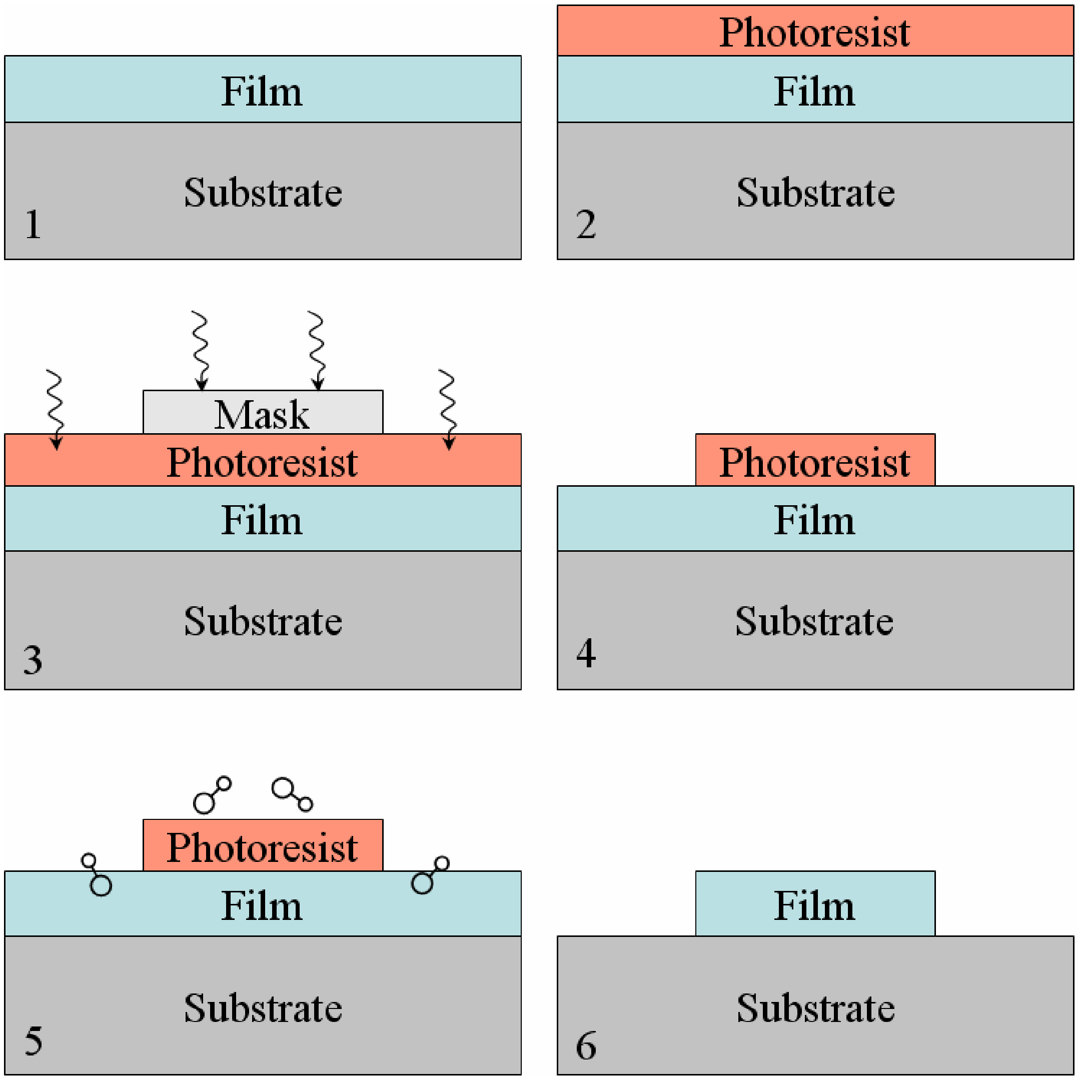

Figure 2-14: Representation of standard wet-etch lithographic technique.

lattice matched or slightly mismatched substrate. A layer of photoresist is applied to the film. This layer is reactive to UV light. A metallic mask having the desired geometry is placed on top of the photoresist layer and exposed to a UV light source. This creates a patterned photoresist layer on the film. The structure is then placed in an etching solution. For the manganites, a KI solution is generally used. The etchant removes the exposed film while leaving the film under the photoresist layer. The remaining photoresist layer is then removed using a solvent and leaves the confined structure without damage. This method is only capable of creating structures larger than about 500 nm and limits the geometry to the predefined parameters of the mask used. To create new geometries, a new mask must be made.

2.3.3 E-beam lithography

E-beam and laser writing are similar to the photoresist method except they do not require a mask. This increases the flexibility to quickly create new geometries without the need to fabricate new masks. The photoresist layer is applied; but, instead of using a mask to block a wide area application of developing photons or electrons, the developing source is selectively applied by scanning a very small beam across the surface on only the areas that will be removed. This takes far longer to complete but allows for the creation of much smaller structures. The limiting factors are the wavelength of the photon or electron and the beam width. Structures of 10-100 nm can be created depending on these factors. Once the photoresist is developed in the desired geometry, the sample can be chemically or plasma etched to remove the exposed film in much the same way as in the photolithography method.

2.3.4 Focused Ion Beam Milling

The FIB and AFM methods mechanically remove atoms and do not require a mask or photoresist layer to be put down. AFM lithography uses direct probe tip contact to mechanically remove material. This technique can shape down to 10 nm however it is very slow—taking days to fully etch a 1 mm x 1 mm sample—and there is a danger of disrupting the crystalline structure of the film. FIB milling is based on a system very similar to SEM; but, instead of using focused electrons, it uses a beam of focused Ga ions. The ions are accelerated under high electric field and used to sputter the film from the substrate. This method is relatively slow and can have some Ga contamination issues; its resolution of 10's of nanometers makes it a good candidate for creating very small structures.

Figure 2-15 shows the effects of FIB etching on samples. The top image shows a 5 μm wire of LPCMO on an SLGO substrate. The temperature vs. resistivity plot was taken with no applied field. The 5 μm wire plot is given in black and shows a typical, smooth MIT. The red plot shows the resistivity after the wire is further confined to 1 μm using the FIB. There is a slight decrease in the maximum resistivity and the MIT occurs at a slightly higher temperature.

While we would expect the maximum resistivity to increase, the decrease could be caused by Ga implantation and surface contamination. To attempt to remove the Ga, the wire is then annealed at 400 C. This is high enough to evaporate Ga but too low to

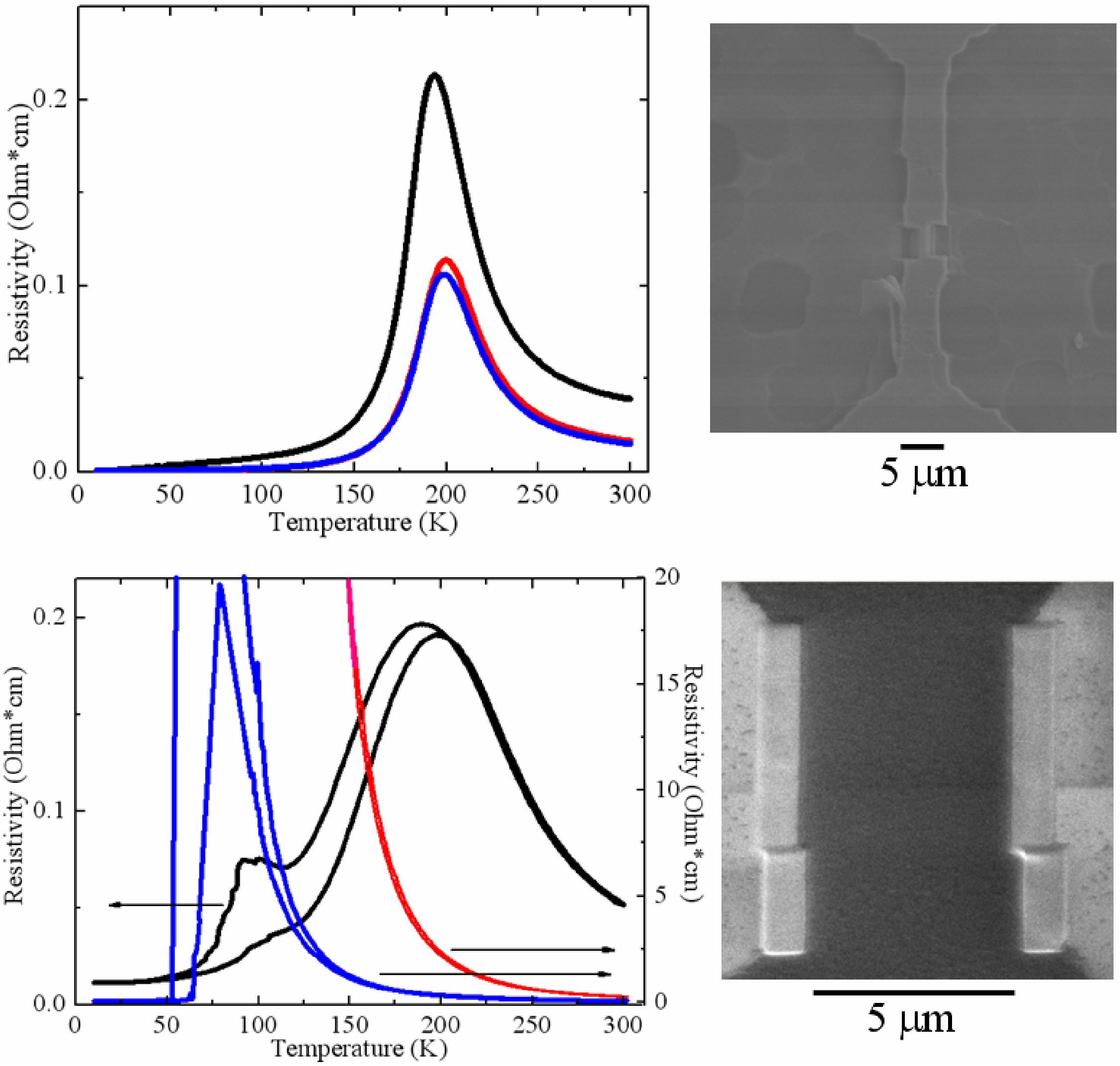

Figure 2-15: Effects of FIB etching on transport. **Top**: LPCMO on SLGO 5 µm wire (black), wire etched with FIB to 1 µm (red), 1µm FIB etched wire after anneal (blue). **Bottom**: LPCMO on LAO 5 µm wire (black), wire edges smoothed with FIB (red), smoothed wire after anneal (blue). SEM images show wires after FIB treatment.

effect the LPCMO structure. The blue line shows the results to be another slight decrease in resistivity while the MIT temperature shifts lower. These results are unexpected and suggest that it may not be Ga contamination alone that is affecting the transport data. It seems more likely that the FIB process has changed the wire's conducting properties through a modification of either doping or strain relaxation. During chemical etching, slight edge roughening can occur. The bottom panel in Figure 2-15 shows the effects of using FIB to smooth the edges of a chemically etched wire of LPCMO on an LAO substrate. The temperature dependent transport data was taken under a 2 T magnetic field and shows warming and cooling curves of the wire before smoothing (in black), after FIB smoothing (in red), and after FIB smoothing with a subsequent anneal at 400 C (in blue). After the FIB is applied the resistivity jumps by orders of magnitude and there is no hysteresis to indicate the ferromagnetic phase. This is strange since we would expect any Ga contamination on the surface to reduce the measured resistivity of the sample; and without it, there should still be hysteresis. After annealing, the hysteresis between warming and cooling returns. There is still an orders higher resistivity at the MIT, but at around 50K, we see that the resistivity returns to nearly what it was before the edge smoothing. This means that the magnetoresistance has been greatly improved. Whether this is from Ga implantation or the removal of edge roughness is unclear. Future work should be done to clarify this.

Chapter 3 Experimental Results

3.1 Spatial Confinement on Electronic Phase Separated Manganite

3.1.1 Introduction and Motivation

Despite having a single crystal structure, transition metal oxides (TMO) often have exotic electronic and magnetic properties. These properties have been attributed to electronic phase separation (PS). Some theoretical background on PS has been given in Chapter 1.4. In this work, we show that by reducing a PS manganite to the scale of the electronic PS domains that reside within it the metal-insulator transition (MIT) can be observed with a much greater degree of accuracy. The MIT observed in a resistivity vs. temperature scan for a typical bulk or thin film manganite sample is very smooth and gradual across a relatively large temperature window of roughly 100 K[4,61-63] Whereas a spatially confined manganite wire has a much more narrow MIT window.

The observed gradual MIT seen in transport measurements on bulk or thin film phase separated materials has been explained through a percolation model[64,65]. For such large samples the gradual change in character can be understood as many small transport channels opening or closing across a wide temperature range. By reducing the scale of the material to the order of the electronic phase domains within, it can be expected that that single domain transitions would become much more dominant in transport measurements. We find that this is indeed the case. By systematically reducing the width of a thin film we observe the onset of single domain percolation in the form of ultra-sharp steps in the resistivity vs. temperature scans.

3.1.2 Experimental and Theoretical Considerations

$La_{1-x}Pr_xCa_{3/8}MnO_3$ was selected as the model system for these experiments because of its well known micron scale PS into charge ordered insulating (COI) and ferromagnetic metal (FMM) domains[4]. A 70 nm thick film was grown with laser MBE in ultra high vacuum with an ambient O_3 pressure of 4×10^{-5} Torr using a 248 nm laser with a fluence of 1 J/cm^2. To confirm film quality and epitaxy, AFM, XRD and Rutherford Backscattering experiments were conducted after growth. The results showed that the film was epitaxial with an atomically flat surface having regular terrace widths of 50 nm.

For consistency, several LPCMO wires were fabricated using optical lithography from a single thin film of LPCMO (x = 0.3) epitaxially grown on (100)-oriented $LaAlO_3$ (LAO). This ensured that subtle changes in growth conditions would have no influence on the results, as all structures were shaped from the exact same film. Five wires of varying widths between 20 μm and 1.6 μm were etched using standard wet-etching techniques [See Chapter 2.3.2]. 500 μm x 400 μm current contacts and 500 μm x 200 μm voltage contacts of Au were evaporated onto each wire. These pads were then wire bonded to the PPMS sample puck using 20 μm Al wire. During transport measurements, the magnetic field was always applied along the easy magnetization axis which for these samples was perpendicular to the film plane.

3.1.3 Experimental Findings

Resistivity (ρ) vs. temperature plots under a 3.75 T magnetic field for three wire widths are shown in Figure 3-1a. We see that for a 20 μm LPCMO wire the MIT is smooth and closely resembles what would be expected for either bulk or thin film forms.

The 5 μm wire has a fairly smooth MIT though the peak resistivity is slightly higher and shifted to a lower temperature. We also see that there is a very small discontinuity in the MIT at about 100 K. The 1.6 μm wire exhibits a very different behavior at the MIT. Not only is the overall wire resistivity much larger at its peak, but its transitions from insulator to metal on the cooling curve and metal to insulator on the warming curve are much sharper. The ultrasharp jump in resistivity is five times the total change in ρ as that seen in the 20 μm wire while the MIT is completed over a much smaller temperature window.

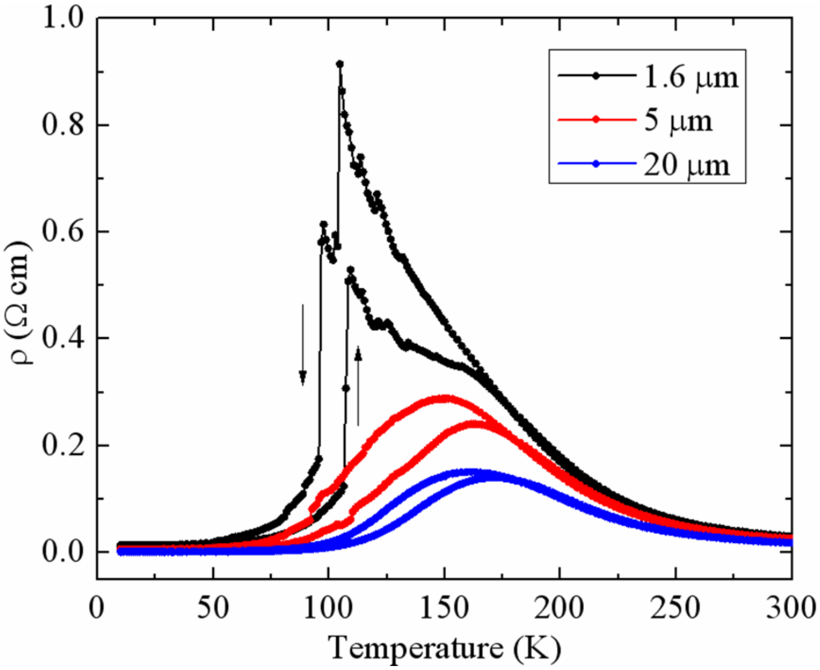

Figure 3-1: Temperature dependent resistivity plots for varying wire widths. Transport data for three wire widths under 3.75 T applied field on warming and cooling—indicated by arrows.

The fact that the 1.6 μm wire shows two very noticeable drops in ρ across a 20 K window while the other two wires do not is particularly interesting. Since all wires are fabricated from the same film, we can state that the change in the observed MIT is directly related to spatial confinement effects. Since the 1.6 μm wire is on the order of the inherent electronic phase domains, it is reasonable to assume that the huge jumps in resistivity are a direct result of single domains undergoing a MIT that opens or closes a conducting channel in the wire. This is consistent with the model shown in Figure 2-13. In the wider wires or a film geometry, a local first order phase transition from FMM to COI would have a very small effect on the overall observed ρ. The smooth transition seen in the 5 μm and 20 μm wires are consistent with having many conducting channels for current to pass through. The blockage of one channel would not have a huge effect on the global properties. The sharp jumps in the 1.6 μm wire's transport data can be explained as being caused by these same local first order transitions from FMM to COI having a much more dominating effect since there are far fewer conduction channels present in the spatially confined geometry. The opening or closing of a single conduction channel would have a much greater influence on the overall observed resistivity.

While such jumps in resistivity and magnetization have been observed in some other TMO systems[66-69], the origins of these jumps were all attributed to mechanisms other than a first order electronic phase transition at the MIT. Since the large jumps in ρ that we observe are seen at a stable field above 1 T, we can be assured that they are not caused by the Barkhausen effect or magnetic domain fluctuations. Also, the single crystal nature of our wires eliminates the possibility of these jumps being caused by the domain wall effects seen in polycrystals. Finally, the ultra sharp jumps are seen well above 10 K below which low temperature field effects have been observed.

We would expect that the domain formation process would be random in a true single crystal. Figure 3-2 shows the MIT for the 1.6 μm wire on three different cooling cycles. The jumps representing single domain transition from COI to FMM occur at different temperatures and have different influences on the overall wire ρ. This suggests that edge roughness effects and quenched disorder are not seeding points for the electronic phase domains in the wire. If they were, we would observe jumps of equal size and location in temperature for each scan.

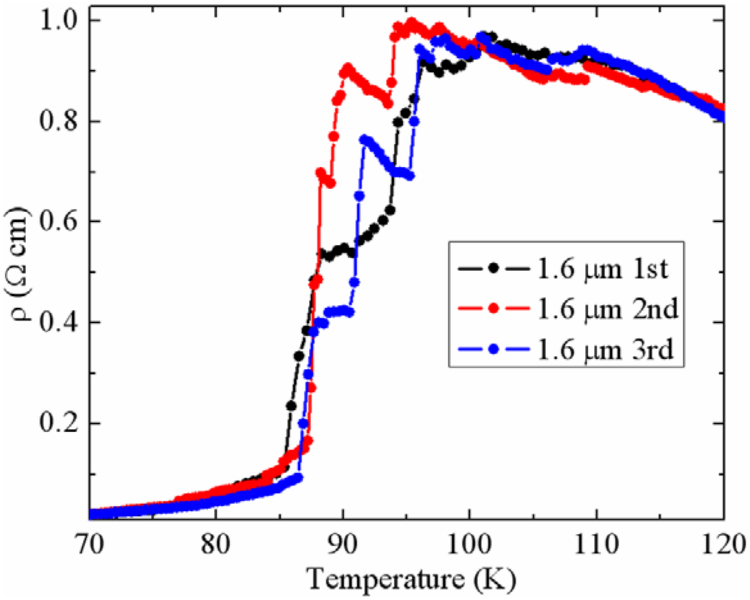

Figure 3-2: Cooling curves at MIT for the 1.6 μm wire on three repeated cooling cycles.

Magnetic field dependence (not shown here) was also observed to have an effect on the jump height. By substantially increasing the applied magnetic field, the jumps disappeared. This is consistent with melting of the COI phase.

This work demonstrates that a percolation model is a reasonable way to treat transport in manganites while suggesting that quenched disorder may not be the correct interpretation of phase domain creation. Most importantly, it opens the door to new studies in which single domains can be studied using transport measurements to *see* local electronic phase transitions.

3.2 Reemergent Metal-Insulator Transition Exposed

3.2.1 Introduction and Motivation

The metal-insulator transition is characterized as a single peak in the temperature-dependent resistivity measurements; exceptions to this have never been seen in any single crystal material system. We find that by reducing a single crystal manganite thin film to a wire with a width comparable to the mesoscopic phase-separated domains inherent in the material, a second and robust metal-insulator transition peak appears in the resistivity vs. temperature measurement. This new observation suggests that spatial confinement is a promising route for the discovery of emergent physical phenomena in complex oxides.

The striking transport properties of perovskite manganites, manifested in exotic behaviors such as their colossal magnetoresistance (CMR), are believed to be caused in large part by their intrinsic tendency toward the coexistence of competing orders[4,64,70], a phenomenon often referred to as phase separation (PS). For manganites, PS and its associated percolative transport are generally considered to be responsible for their unusually high magnetoresistance[4,64]. If the spatial dimension of these materials is artificially reduced to the characteristic PS length scale, dramatic changes in their transport properties could occur. For instance, discrete steps in resistivity have been observed in the metal-insulator transitions (MIT) in systems of manganite wires[71,72].

Recent experimental and theoretical investigations have shown that the nanometer is the most typical length scale for PS in manganites[73-78,65]. However, sub-micrometer scale PS has also been observed in $La_{1-x}Pr_xCa_{0.375}MnO_3$ (LPCMO) system where ferromagnetic (FM) metallic and charge ordered (CO) insulating domains coexist[79,80]. Although the driving mechanisms that cause large scale PS is still under investigation[81-83], the LPCMO system provides an ideal system for studying the effect of spatial confinement as it can be easily accessed by conventional lithographic fabrication processes[72,84]. In this work, we show never before observed emergent transport properties in LPCMO wires that differ vastly from bulk and thin films of the same material. We have found that by reducing a single crystal LPCMO thin film to a wire with a width comparable to the mesoscopic phase-separated domains inherent in this material, a second and robust MIT peak appears in the resistance vs. temperature measurement. This phenomenon can be theoretically modeled by describing the system as a resistive network created by local modifications of bandwidth or strain. These findings are anticipated to lead to further experimental and theoretical studies in exploring novel emergent behavior while potentially leading to new functionalities in, not only manganites, but any material where phase competition plays an important role in determining bulk properties.

3.2.2 Experimental and Theoretical Considerations

$La_{1-x}Pr_xCa_{3/8}MnO_3$ wires were fabricated from epitaxial thin films using optical lithography. The parent thin film was grown on a single crystal substrates of $SrLaGaO_3$ (100), $LaAlO_3$ (100) and $NdGaO_3$ (110) using laser (248 nm, 1 J/cm^2 fluence) molecular beam epitaxy in an ultrahigh vacuum chamber (base pressure $< 1 \times 10^{-10}$ Torr). The high quality of the epitaxy was confirmed by atomic force microscope (AFM), X-ray diffraction, and by Rutherford Backscattering (RBS)/channeling experiment in a 2 × 1.7 MV Tandem accelerator using 2.1 MeV alpha particles. Wires were then fabricated using wet etch optical lithography, as described in chapter 3. The results discussed in this work were obtained on 10μm wires. The electrical connections between the Au pads and the puck of a Physical Property Measurement System were made using a Kulicke and Soffa wire bonder (model 4123) with twenty microns diameter Al wires being directly engaged without using any paint or solder. This removes all possible contact problems for the transport measurements. The magnetic field was applied along the easy magnetization axis, i.e. the direction perpendicular to the substrate surface during the transport measurements.

Transport measurements were conducted by the Quantum Design Physical Properties Measurement System (PPMS) with a temperature precision of 0.01 K and a magnetic field precision of 0.1 Oe. Measurements were done using standard 4-probe measurements with the PPMS electronics with scan speeds of 3 K/min. With a maximum allowable current of 0.05 μA and a maximum allowed power of 1000 mW.

Some details of the theoretical study are here presented: (1) In the effective resistivity analysis, the resistivity vs. temperature of the individual components were obtained from Uehara[4], using hundreds of points taken from their Figure 1a for an accurate description, as opposed to a simple polynomial fitting. (2) The pair of Pr compositions 0.3 and 0.4 emphasized in the text, and the relative amount 0.0003% of 0.4, leads to a deep valley in between the resistivity peaks, in agreement with experiments. Several other compositional pairs were tried, such as 0.375 and 0.3, but it was not possible to reproduce such a deep valley, although the effective resistivity also had two peaks as in the experiments. Other pairs, such as 0.325 and 0.20, can again produce two peaks but it is difficult to have those peaks at the correct temperatures or with the correct intensities to match experiments. It is in this sense that the results presented are considered to be optimal to reproduce the experimental resistivity vs. temperature curve.

3.2.3 Experimental Findings

Figure 3-3a shows an optical image of a typical $La_{1-x}Pr_xCa_{0.375}MnO_3$ wire fabricated from an epitaxial thin film using conventional wet-etch optical lithography. Figure 3-3b and Figure 3-3c show the temperature-dependent resistivity of a 70 nm thick LPCMO film grown on $SrLaGaO_4$ (100) (SLGO) and a LPCMO wire with dimensions 70 nm x 10 μm x 50 μm on SLGO both having a 0.3 Pr doping which translates to an $<r_A>$ of 1.339 Å. The film (Figure 3-3b) shows the typical MIT expected in CMR thin samples. The CO insulator phase develops and coexists with the low-T FM metallic phase which results in the observed thermal hysteresis. By increasing the magnetic field strength, the transition temperature increases while the magnitude of the warming/cooling hysteresis decreases. In Figure 3-3c, the 10 μm wire exhibits a similar behavior but with a notable addition. With cooling, a MIT occurs at roughly the same temperature (~150 K) as in the film, but after entering a region of metalicity (~125K), the resistivity rebounds and forms a *second* MIT (~75K). The resistivity difference between cooling and warming (Figure 3-3insets) illustrates the dramatic benefits of using spatial confinement in PS materials in order to observe concealed properties.

Though not as dramatic, this behavior is also seen in more narrow wires (Figure 3-4). In this instance, the reemergent peak is present but is not as noticeable due to the dominance of the higher temperature resistance peak which is much broader than that seen in the 10 μm wire. This can be explained by two important facts: 1) the 1 μm wire has the same 1/5 width/ length ratio as the 10 μm wire shown above so that it has a lesser probability of having as many step bunches on the underlying substrate and 2) the domain blockages across the wire will be more complete thereby creating a spreading of the primary MIT that overlaps the reemergent transition. That is to say, that a 1 μm wide domain in the 10 μm wire will not fully dominate the resistivity measurements; because when it transitions, it will not completely block or unblock the wire. Only very large domains would be seen. However, in the 1 μm wire, any number of 1 μm domains with very slight differences in transition temperature would create full blockages that would cause the resistivity measurements to *smear* across the temperature domain. This is why we see the resistivity jumps in Figure 3-4a. Each of these jumps represents a single domain as it transitions. This concept of single domain transitions across a wide range will be explored further in the next chapter.

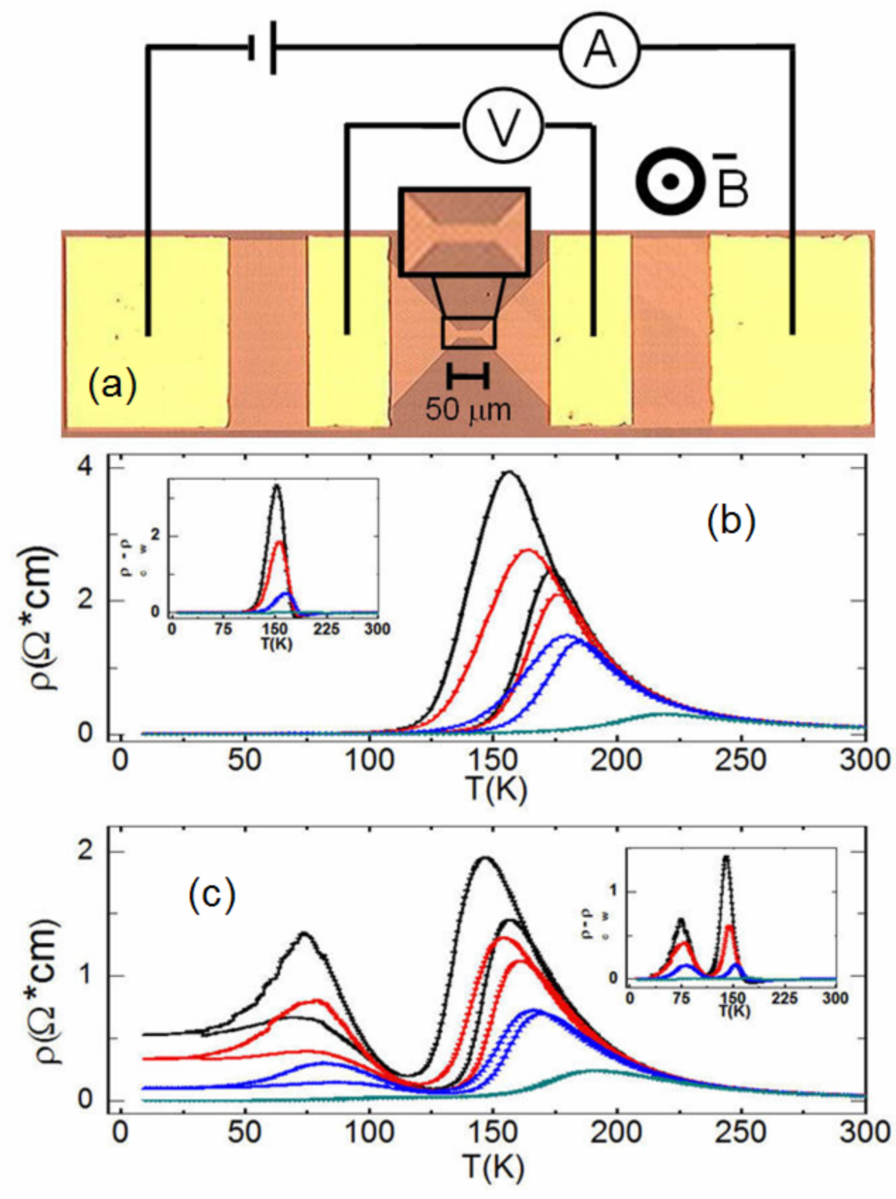

Figure 3-3: Reemergent metal-insulator transition. Transport and magnetic properties of 70 nm La0.325Pr0.3Ca0.375MnO3 thin film and wire with $\langle r_A \rangle$ of 1.339 Å on lattice matched SrLaGaO4 on heating and cooling (indicated by arrows) under increasing magnetic fields. (**a**) Optical image of 10 μm geometry with expanded view of wire and legend of applied magnetic field direction and 4-point probe configuration. (**b**) Comparison of temperature dependence of resistivity in film at 0 T (black), 0.4 T (red), 1 T (blue), and 3.5 T (green). The film shows a single MIT peak. (**c**) Comparison of temperature dependence of resistivity in 10 μm wire at 1.5 T(black), 1.75 T(red), 2.25 T(blue), and 3.75 T(green). The wire shows a reemergent, low temperature peak in ρ that is not present in the film. (**Insets**) Show differences in resistivity between warming and cooling curves.

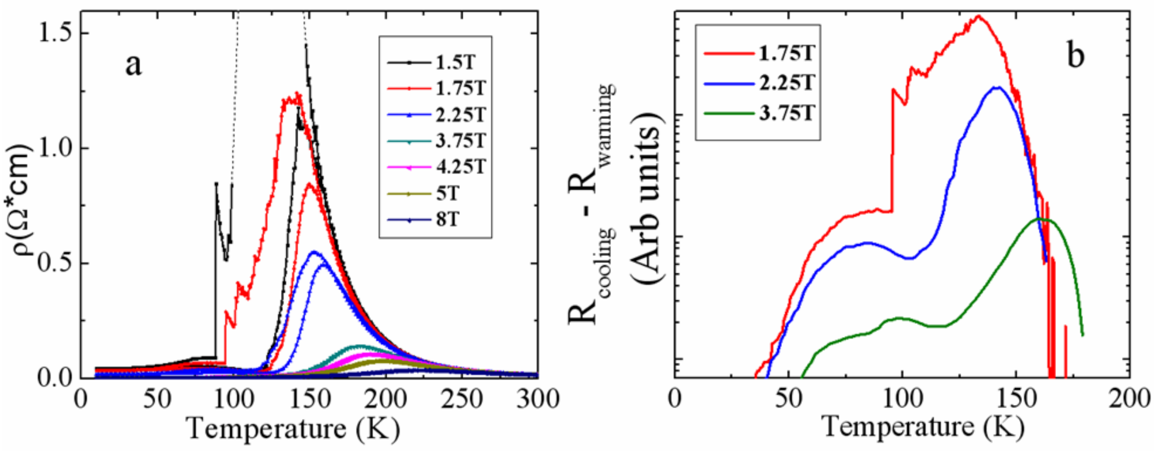

Figure 3-4: 1μm wire transport. Transport and magnetic properties of 70 nm $La_{0.325}Pr_{0.3}Ca_{0.375}MnO_3$ wire with $<r_A>$ of 1.339 Å on lattice matched SrLaGaO4 on heating and cooling. (**a**) Comparison of temperature dependence of resistivity in 1 μm wire under various fields. The wire shows a weak reemergent, low temperature peak in ρ. (**b**) Differences in resistance (log) between warming and cooling curves.

The reemergent MIT behavior has never been observed in manganite materials in any single crystal bulk or thin-film form and, to our knowledge, has not been observed before in any other single crystal compound[85,86]. There are bulk manganites that have large magnetoresistance at two very different temperatures, but only one of these temperature regions presents a canonical CMR with a resistivity peak. The other large magnetoresistance region is at low temperature and is caused by a first-order transition. It has been observed that extrinsic factors such as grain boundary effects[87,88] and chemical defects[89] can seed a low temperature peak in resistivity in polycrystalline samples. Polycrystalline $La_{0.67}Ca_{0.33}Mn_{1-x}Ru_xO_3$ has been shown to exhibiting a second peak in resistivity, but the underlying cause is debated[90] and cannot be confirmed as truly intrinsic without a full study on single crystal samples. Both resistivity peaks in the wire are strongly sensitive to magnetic fields. With increasing fields, the intensities of both peaks decrease, while the peak positions shift toward higher temperatures.

Since a reemergent MIT has never been documented in either bulk or thin film form, it is reasonable to assume that this effect is made visible due to the spatial confinement in the wire geometry. In LPCMO, FM and CO phase separation and percolative transport are generally accepted as the governing mechanisms for the observed MIT[64,4]. Within this context, the simplest way to understand a reemergent MIT is to assume that there are two types of regions in the system with their MIT's occurring at distinctly different temperatures. Interestingly, the LPCMO system exhibits a sharp change in the MIT temperature in the vicinity of a critical $\langle r_A \rangle$[4,91]. While the $\langle r_A \rangle$ value can be tuned by Pr-doping, it has been shown that the effects of lattice strain act comparably to this "chemical pressure" in influencing the perturbation of the Mn-O-Mn bond angles[92,93]. Considering this fact, a slight spatial variation of Pr-doping or lattice strain can lead to two types of regions with distinctly different MIT temperatures assuming that the effective $\langle r_A \rangle$ has been preset to be close to the critical point, which is the case in our system.

For the LPCMO wire prepared by laser MBE, a spatial variation of Pr doping is rather unlikely to occur due to the nature of the atomic deposition process. However, a slight spatial variation of lattice strain in the LPCMO wire is highly possible due to the presence of steps that are inherent in all thin films. The lattice strain in the regions at the step edges is, in general, slightly different from that at the terrace with the former being only a small fraction of the latter. In the following, we devise a simple model to test if such a spatial variation of strain can indeed give rise to the reemergent MIT behavior.

In this model, a resistive series was created using the known bulk LPCMO resistivities[4] and plotted as $R_t = a\, R_1 + (1 - a)\, R_2$ where R_t is the total resistance of the series, and R_1 and R_2 are resistances of LPCMO for two similar Pr-dopings (Figure 3-5). It is important to point out that, while we justify the existence of R_1 and R_2 by a small fluctuation in the $<r_A>$ forming a gate across the wire, R_1 and R_2 are likely caused by local modifications of epitaxial strain as mentioned above. Figure 3-3a shows a simple schematic for this model where the unmodified film can be represented as a two-dimensional resistive network, while the etched wire geometry effectively reduces the system to a serial network. The resistive differences of these two dopings can be attributed to the chemical pressure differences resulting from the change in $<r_A>$[94]. Figure 3-5b shows R_t for a serial LPCMO system comprised of 99.9997% LPCMO with an $<r_A>$ of 1.339 Å and 0.0003% LPCMO with a smaller $<r_A>$ of 1.334 Å. These were selected due to the fact that, while the $<r_A>$'s only differ by 0.002%, their transport properties are vastly altered[4,91]. This configuration produces hysteretic differences at 45 K and 125 K, and we can plainly see a double-peak formation similar to that experimentally observed. Markedly, only a very small amount of the component with the smaller $<r_A>$ is needed to create the reemergent MIT, as a larger percent would totally dominate at low temperatures. This is consistent with the fact that the regions associated with the step edges are only a small fraction of the whole wire.

The pair of LPCMO compositions ($<r_A> = 1.339$ Å and $<r_A> = 1.334$ Å) emphasized here, and the relative amount 0.0003% of the composition with the smaller $<r_A>$, leads to a deep valley in between the resistivity peaks, in agreement with experiments. Several other compositional pairs were tried, such as 1.336 Å and 1.339 Å, but it was not possible to reproduce such a deep valley, although the effective resistivity also had two peaks as in the experiments. Other pairs, such as 1.338 Å and 1.344 Å, can again produce two peaks, but it is difficult to have those peaks at the correct temperatures or with the correct intensities to match experiments. It is in this sense that the presented results are considered to be optimal to reproduce the experimental resistivity vs. temperature curve.

Due to strain effects, it may be suspected that the wire's edge is the likely location for phase differences that vary from the bulk. Moreover, investigations of nano-size manganites have identified a difference between the surface and the center of those clusters[95], again suggesting that the edge could behave differently from the wire's center. If this is the case, a parallel configuration of resistances for two different $<r_A>$ compositions could describe the manganite wire. However, the reemergent MIT peaks do not occur if R_1 and R_2 are in parallel since the charge will always flow through the lower resistance; the parallel combination will only exhibit a MIT at the highest temperature. Therefore, it is understandable why the reemergent MIT behavior has never been seen in thin films, nano-scale clusters, or bulk.

In these systems, the electrons would have more lanes of lower resistivity to follow. But, by limiting the dimensions of the film to be comparable to the PS scale, we force the electrons to travel across both high- and low-T MIT regions in the center of the wire. So while the wire in the experiment is 10 μm wide, edge effects reduce the true lane of electrical transport down to a scale that is of the same order as the inherent phase

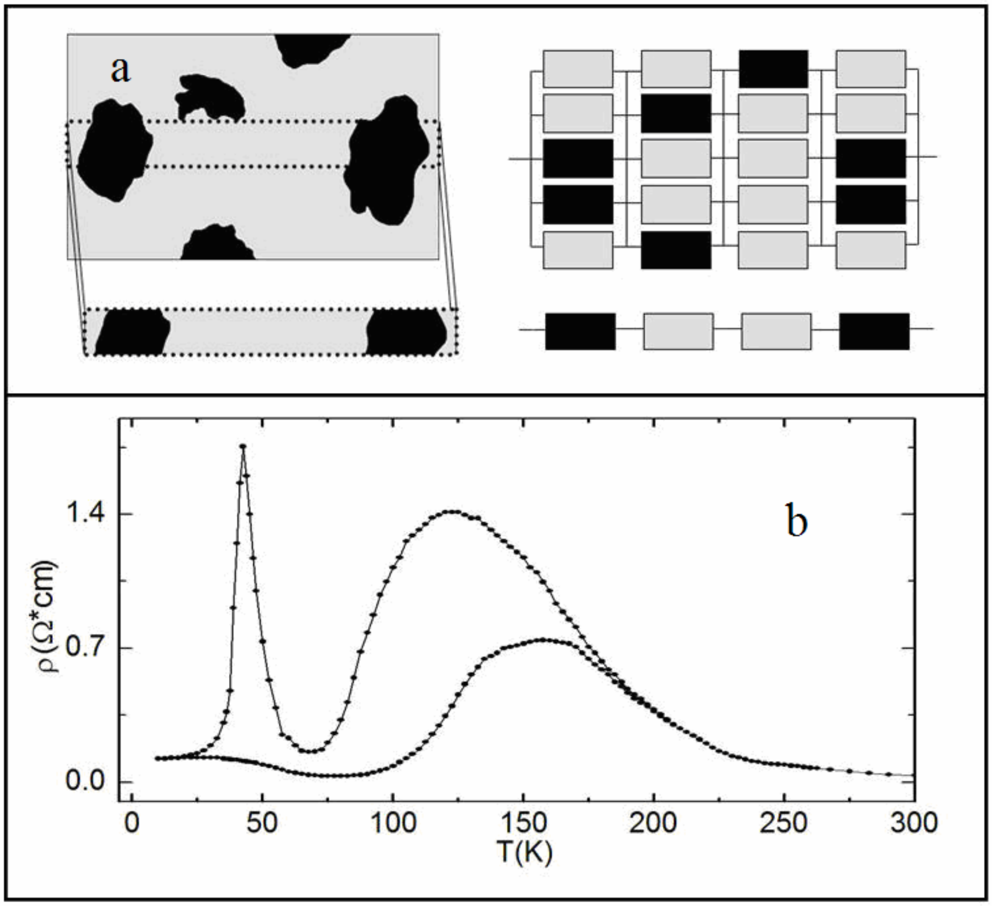

Figure 3-5: Theoretical model for LPCMO wire's reemergent MIT. (**a**) Schematic diagram of film and wire with corresponding resistive networks. Black and grey areas represent regions of differing resistivity with independent MIT temperatures. (**b**) Model data for the LPCMO resistivity in a serial resistive network using LPCMO with constituent $<r_A>$ of 1.334 Å and 1.339 Å. The resistivity at 125 K is dominated by the larger $<r_A>$, while the low-T peak is contributed by the smaller $<r_A>$.

domains. This unveils the reemergent MIT which provides us with a view of otherwise hidden regions that can only be seen by reducing the electronic transport lanes to a serial resistive network. Previous theoretical work remarked on the potential importance of quasi one-dimensional manganite systems[96]. Since bulk quasi-1D manganites do not exist, our LPCMO confined configuration is the closest to a realization of those theoretical expectations.

Since chemical pressure and epitaxial strain both act comparably within this system[92,93], one would expect a strong variation of the reemergent MIT behavior when either the $<r_A>$ or the substrate induced strain is varied. Indeed, when $<r_A>$ is increased from 1.339 Å to 1.342 Å, the LPCMO wire on SLGO only exhibits a single MIT. However, if the epitaxial (compressive) strain in the wires is systematically increased by fabricating the wires on $NdGaO_3$ (110), $SrLaGaO_4$ (100), and $LaAlO_3$ (100) substrates, with nominal LPCMO lattice mismatches of +0.5%, <0.1%, and -1.6%, respectively, the reemergent MIT *reappears* in the wire under the higher compressive strain of the LAO substrate (Figure 3-6a-c).

In previous work, LPCMO with $<r_A> = 1.339$ Å was grown on $LaAlO_3$ (100) and spatially confined to similar scales as that used in this work without a double peak in the temperature dependent resistivity measurements[71]. Taking this data with what has been presented above, we can see that the reemergent MIT appears to arise in a narrow window of strain which could be created by a balance between the chemical pressure related to $<r_A>$ and the epitaxial strain contributed from the substrate[92,93]. The double

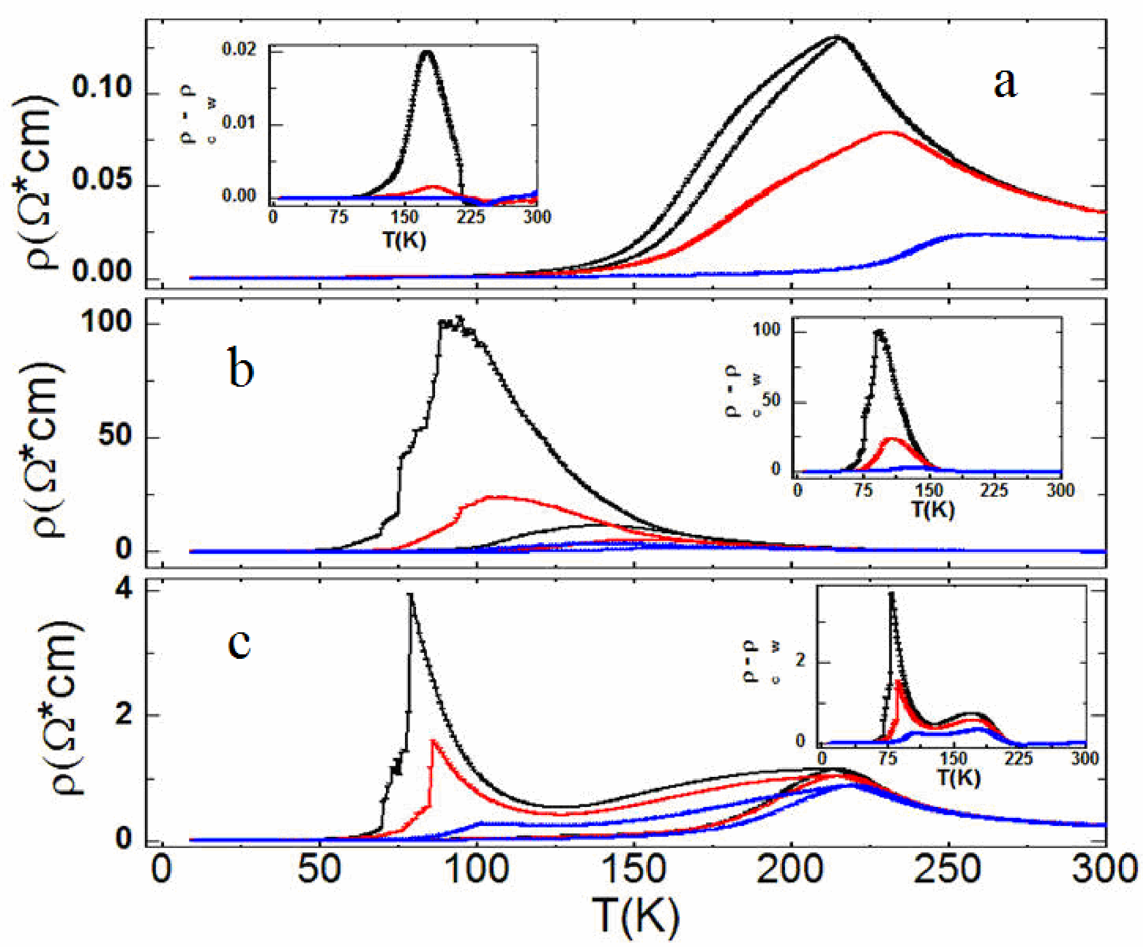

Figure 3-6: Reemergent transition tuned through strain. Transport and magnetic properties of 10 μm $La_{0.391}Pr_{0.234}Ca_{0.375}MnO_3$ wires with $<r_A>$ of 1.342 Å on substrates of varying compressive strain. (**a**) LPCMO wire on $SrLaGaO_4$ (<0.1% lattice mismatch) for 0 T (black), 1. 5 T (red), and 3 T (blue). Hysteretic behavior is never present at lower temperature and is quickly suppressed with application of magnetic fields. (**b**) LPCMO wire on $NdGaO_3$ (+0.5% lattice mismatch) for 2.5 T (black), 2.75 T (red), and 3 T (blue). The slight increase in tensile strain pushes the MIT to a lower temperature but does not spawn a clear separation into two distinct MIT areas, which could be due to overlap. (**c**) LPCMO wire on $LaAlO_3$ (-1.5% lattice mismatch) for 0 T (black), 0.2 T (red), and 0.4 T (blue). Independent metal-insulator transitions are visible at both high and low temperatures with some overlap. (**Insets**) show differences in resistivity between warming and cooling curves.

peak observed in the wire on the SLGO substrate at $<r_A>$ = 1.339 Å can be destroyed by increasing the $<r_A>$ of the LPCMO wire which increases the internal chemical pressure. LAO exerts a compressive strain on the wire with $<r_A>$ = 1.339 Å and shows no reemergent behavior; but by increasing $<r_A>$ to 1.342 Å, the change in internal chemical pressure acts to counterbalance the strain and push the transport properties into something roughly similar to those observed on SLGO with a larger $<r_A>$. This suggests that there is a critical regime in which the reemergent MIT resides which can be reached through a subtle balancing of strains.

While the effects of edge roughness were shown to be relatively unimportant for wider wires in transport data as discussed in Chapter 2.2.5. It is reasonable to assume that smaller wires would be more susceptible to edge effects from roughness. To test this, we smooth a 1 μm x 5 μm wire of LPCMO with an $<r_A>$ of 1.342 Å on LAO using FIB. We can reduce the edge roughness by shaving 50 nm from each side of the wire and then annealing for 3 hours at 400 C to remove Ga contamination. Figure 3-7a-c shows the wire edges before and after the smoothing process.

We see that the average roughness is about 50 nm before treatment and that it is greatly reduced after FIB smoothing. The temperature dependent resistivity plots show that transport data for the as etched wire is much higher than that observed in the 10 μm wire but still shows the reemergent behavior. After smoothing, the resistivity is orders lower and is actually less than that exhibited by the 10 μm wire while still showing the reemergent behavior. While there is the possibility that some of the drop in resistivity can be attributed to Ga implantation, it seems somewhat unlikely, as we have sputtered

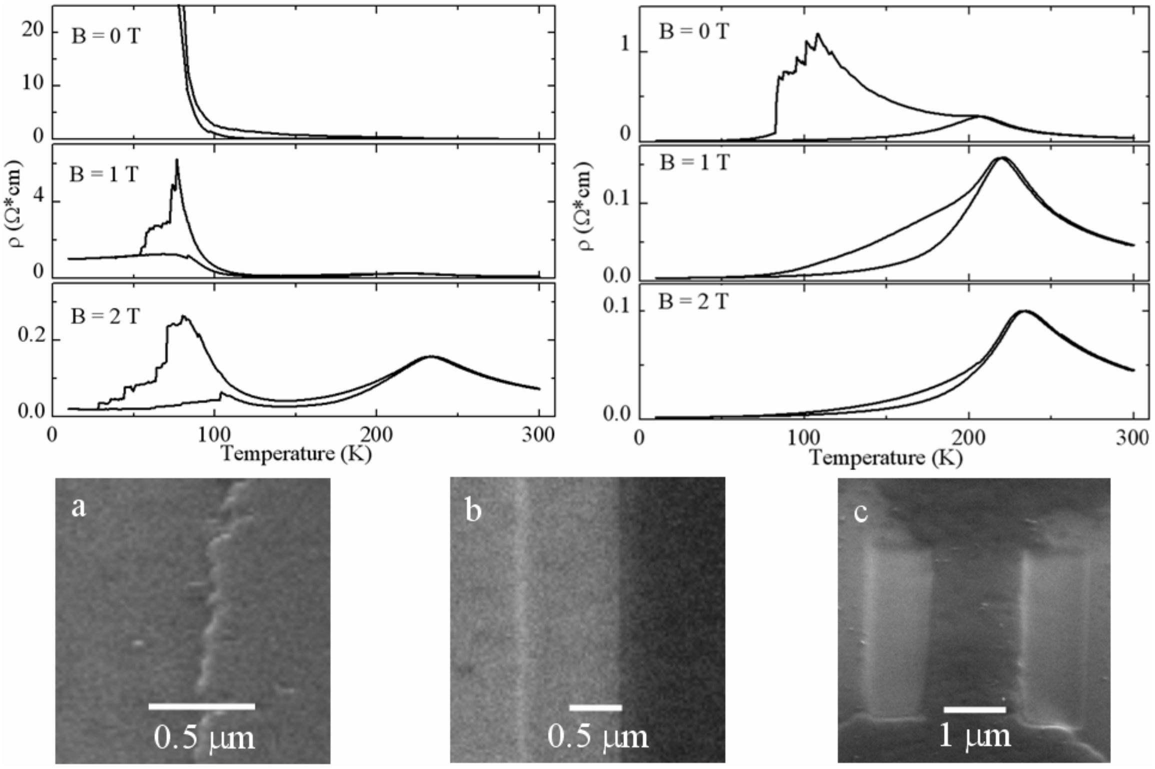

Figure 3-7: Comparison of transport before and after edge smoothing. Transport plots to left are 1 μm wire before edge smoothing. Plots to right are after FIB smoothing. At bottom are SEM images of: (**a**) Edge before FIB treatment. (**b**)Edge after treatment--dark area is wire. (**c**) 1 μm wire after FIB smoothing.

Ga onto an LPCMO wire and annealed it under the same conditions (results not presented) with no change in the resistive properties. These results suggest that while edge roughness can be a factor in smaller wires, they are not the cause of the reemergent peak.

While the underlying mechanism of the proposed simple model needs to be confirmed using imaging techniques and more refined theoretical calculations, our experimental findings already demonstrate the usefulness of reduced dimensionality for the study of PS systems. By forcing electrons to travel through multiple phases, a fuller view of all the phases residing in a material can be obtained via transport measurements. This can effectively be thought of as increasing the "resolution" of electronic transport measurements in phase separated materials. These developments can be applied to improve our understanding of PS in CMR materials and to establish new functionalities for potential uses in oxide electronics. More generally, for any material with an intrinsic length scale on the order of tens of nanometers, quasi-one-dimensional behavior could be observed by the spatial confinement analysis employed here, which could render properties substantially different from those in bulk and thin film forms.

3.3 Time Resolved Phase Transitions

3.3.1 Introduction and Motivation

At the critical point of a first-order electronic phase transition, fluctuations between the competing phases are often a dominant phenomenon. The direct observation of these fluctuations in electronic phases is vital to revealing the microscopic details of the phase transition. This is especially true in strongly correlated transition metal oxides, in which a diversity of electronic phases coexist and are closely connected to several remarkable properties such as high-Tc superconductivity and colossal magnetoresistance[64,2]. Here we report a novel and generic approach that directly records the fluctuations of the electronic phases at the critical point of the metal-insulator transition, using a manganite system as example. In our approach, we reduce a single crystal thin film of $La_{5/8-x}Pr_xCa_{3/8}MnO_3$ to the scale of its inherent electronic charge ordered insulating (COI) and ferromagnetic metal (FMM) phase domains and conduct high resolution resistance vs. time measurements within a critical regime of temperature and magnetic field at the metal insulator transition (MIT). Within this window, we are able to observe individual domains as they fluctuate between COI and FMM.

In strongly correlated transition metal oxides, it is well known that electronic phase separation exists even in chemically disordered (alloy), single crystalline samples[2,97]. Although the sizes of the phase separated domains can vary from a few nanometers to micrometers depending on the materials, they are small enough that individual domain fluctuations at the critical point of the phase transition are unobservable when probed by spatially averaged techniques. While this problem could potentially be solved by imaging a single domain, imaging techniques with high enough spatial resolution such as transmission electron microscopy[4], magnetic force microscopy[37,38] and scanning tunneling spectroscopy[39] all lack the ability to complete a full scan of the area under scrutiny with the time resolution necessary to monitor the phase fluctuations found in complex oxides. In order to fully image a single area of several microns the probe must be scanned across the sample. Because these imaging techniques rely on the spatial scanning of the sample which would require the probe tip to move across the entire sample area, this technique is limited by the speed of the piezos driving the probe head. The temporal resolution is then based on how long it would take for two full images to be taken so that they could be compared. This gives a timescale on the order of seconds, which is much slower than the transition times.

To directly observe phase fluctuations in complex oxides with a high time resolution, we have developed a method that allows a small number of electronic phase domains to be probed simultaneously, whereby phase fluctuations produce the dominant signal in transport experiments. Specifically, we spatially confine a single crystal thin film of $La_{5/16}Pr_{5/16}Ca_{3/8}MnO_3$ (LPCMO) grown on $SrTiO_3$ to a wire geometry of a width of 10 μm which is on the order of the intrinsic ferromagnetic metal (FMM) and charge-ordered insulating (COI) domains residing in the material. In such a spatially confined system, only a very limited number of phase domains can be hosted which effectively removes the problems associated with spatial averaging methods in conventional transport measurements[59,72]. If this system is set at or very near the critical point of the metal-insulator transition, single domain fluctuations will show a clear signature in time-dependent resistivity measurements.

3.3.2 Experimental and Theoretical Considerations

$La_{5/16}Pr_{5/16}Ca_{3/8}MnO_3$ wires were fabricated from epitaxial thin films using optical lithography. The parent thin film was grown on a single crystal substrate of $SrTiO_3$ using laser (248 nm, 1 J/cm^2 fluence) molecular beam epitaxy in an ultrahigh vacuum chamber (base pressure $< 1 \times 10^{-10}$ Torr). The detailed growth procedure has been described elsewhere[71]. The high quality of the epitaxy was confirmed by atomic force microscope

(AFM), X-ray diffraction, and by Rutherford Backscattering (RBS)/channeling experiment in a 2 × 1.7 MV Tandem accelerator using 2.1 MeV alpha particles. Wires were then fabricated using wet etch optical lithography, as described elsewhere[71]. The results discussed in this work were obtained on a 10μm wire, though the phase fluctuating behavior was also seen in 1μm, 3μm, and 5μm wires when held at their respective transition temperatures. The electrical connections between the Au pads and the puck of a Physical Property Measurement System were made using a Kulicke and Soffa wire bonder (model 4123) with twenty microns diameter Al wires being directly engaged without using any paint or solder. This removes all possible contact problems for the transport measurements. The magnetic field was applied along the easy magnetization axis, i.e. the direction perpendicular to the substrate surface during the transport measurements. To solve the change in resistivity, we used the collected voltages and source current to solve for resistance and then applied the known dimensions of the device being studied.

Transport measurements were conducted in a Quantum Design Physical Properties Measurement System (PPMS) with a temperature precision of 0.01 K and a magnetic field precision of 0.1 Oe. Initial low time resolution measurements were done using standard 4-probe measurements with the PPMS electronics. Low and high resolution measurements were done using external electronics consisting of a Keithley 2400 power supply, National Instruments DAQ-card 6036E and homebuilt LabView drivers for control and data collection. 2-probe measurements were compared to 4-probe; there was no difference in data collected with either method, so the data presented here was collected with the 2-probe method. Both constant current and constant voltage were tested with the fluctuations seen in both cases. Constant current was used in this work. It should also be noted that we tried many different voltage and current strengths; all of which showed the fluctuations. All data that we present in this work was obtained under constant current at 500 nA.

The random resistor network for simulation is generated in a similar manner as a carbon nanowire network[98]. Unlike random networks used in previous studies where a large number of resistors are used, in our case only a few resistors may be present in the network. Using a regular lattice with only a few nodes is not appropriate because it will likely introduce artifacts due to the underlying symmetry of the lattice. Instead, we randomly generate the coordinates of the nodes inside the geometry of the nano-bridge. Random connections between pairs of the nodes are then made to form a network. Hundreds of different network configurations are randomly generated. Those with no connected paths from the anode to the cathode are discarded. For the simulation, each node is treated as a switch, randomly switching between the open and the closed positions with a frequency distribution inversely proportional to the frequency. For the small network simulated here, we observe discrete resistivity jumps similar to the experiment. In the body of the paper, we show a typical configuration that exhibits a time-dependent voltage that nearly reproduces all the features of the experiment. Due to the random generation of nodes, running this simulation for a much longer time would produce an even closer match to experimental data.

The noise spectrum of a 2D film is simulated with a large random network generated in a similar manner. In this case, we used 1,000 nodes between the anode and the cathode, and invoked the periodic boundary condition in the transverse (y-) direction to simulate an infinite film. The random switching of the nodes follows the same algorithm as in the case of the wire.

3.3.3 Experimental Findings

Figure 3-8a shows the wire's resistivity as a function of temperature on warming under a 3.75 T magnetic field. This field is sufficient to align the ferromagnetic domains without melting the charge ordered phase which allows us to probe only the electronic domains without interference from magnetic domains[99]. The metal-insulator transition is clearly visible across a 2 K window centered at 83 K as an ultrasharp peak in resistivity (ρ) with a Δρ/ρ of 3,200%. This is contrasted with the same sample but in a film geometry (Figure 3-8a inset) which shows a smooth transition from metallic to insulating across a 150 K window. The extremely large Δρ/ρ ratio results solely from the wire geometry's ability to remove the effects of spatial averaging in transport measurements. By setting the temperature of the LPCMO wire precisely in the middle of the 2 K window found in the temperature dependent resistivity scan, it is possible to study the microscopic details of the transition in both space and time.

Figure 3-8c and Figure 3-8c show the time-dependent resistivity while the wire is held at the transition temperature. Figure 3-8b has a relatively low time resolution of 10 seconds and is characterized by a stable competition between two states with resistivity jumps of 46%. By increasing the time resolution from 10 s to 22 μs, the true nature of this volatility becomes clear Figure 3-8c.

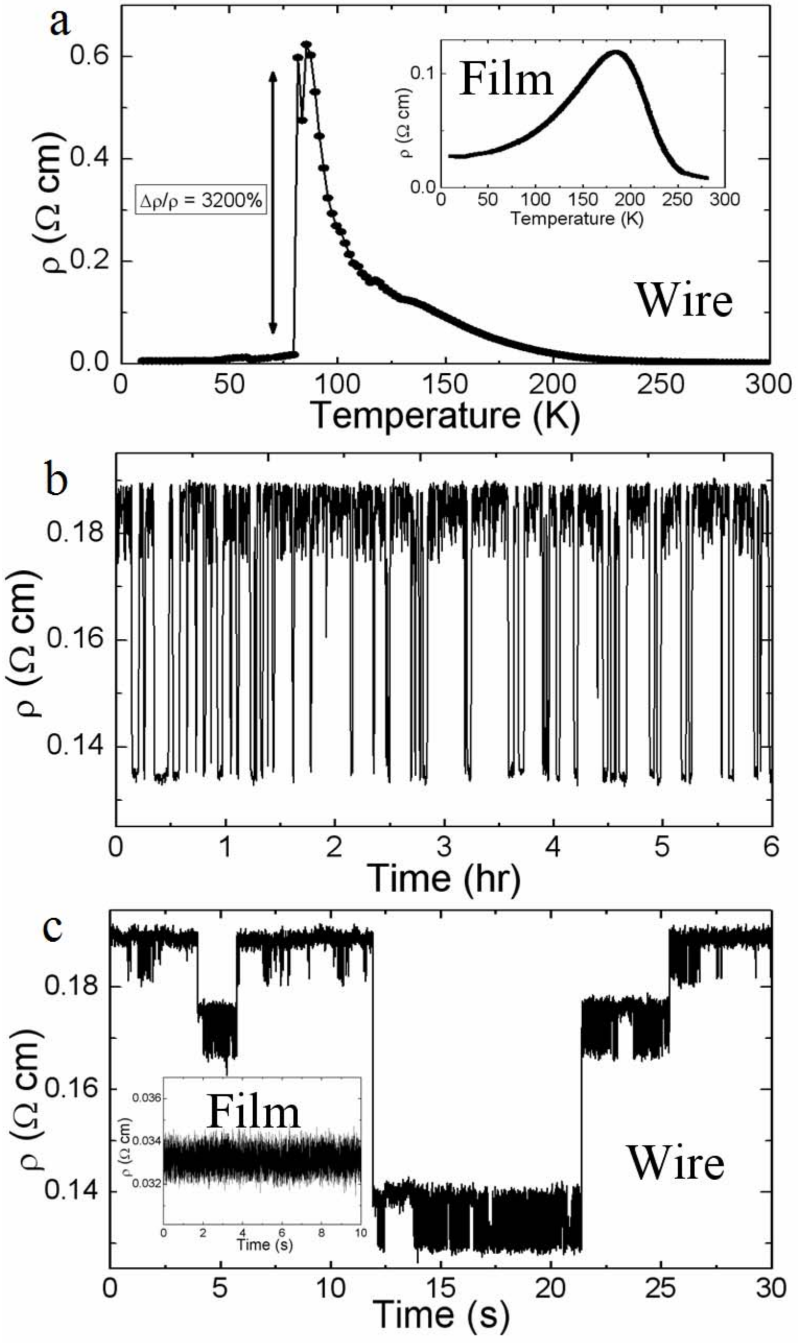

Figure 3-8: Transport measurements for 10 μm wire. (**a**) Temperature dependent resistivity plot for a 10 μm LPCMO wire under 0.5 μA constant current (**inset**: Temperature vs resistivity plot of the same sample in a thin film form.) (**b**) Long scale, low sample frequency resistivity vs. time plot for wire held at 83 K. (**c**) Wire's resistivity vs. time plot at the transition temperature taken at 45 kHz (**inset**: Films resistivity vs. time plot under the same conditions.)

The apparent two-state system is actually comprised of a much richer multi-state system. There are three inherent resistivity levels, each containing a further two-state fluctuation. In unconfined structures, such as film (Figure 3-8c inset) or bulk, this behavior is not observable under the same conditions, nor is it seen in the wire geometry outside of the metal-insulator transition 2 K window.

These data clearly show that fluctuations that change the electrical resistance exist in these phase separated manganite wires. The fluctuations only exist near the transition temperature where electronic domains are fluctuating between FMM and COI and are not individually observable in films or bulk. From this, we conclude that these fluctuations are a direct signal of the microscopic fluctuations in these phase domains at the transition temperature. The comparable dimensions of the inherent domains to the wire result in a large change in wire resistance when a single domain fluctuates from one phase to another.

Figure 3-9 shows the ln(R) vs 1/T plot for the wire. By taking the slope of the line, we can deduce the energy gap in the material. We see for a linear fit between 220 K > T > 180 K there is an activation energy of 0.27 eV which is in agreement with the average optical gap of about 0.2 eV found on a similar LPCMO doping[100]. However whereas previous studies see a continuous transition in gap energy below 180 K for surface studies of thin film LPCMO[101], we see a very different behavior in the wire. Below the MIT temperature seen in the film geometry, there are two transitions in the measured gap energies before the wire's MIT temperature is crossed. More curious is that the temperature range dominated by insulating domain blockages shows a lower energy gap than the region with more clear conduction channels. These facts seem to suggest that this treatment may be too simple for our system. It has been suggested that the onset of a pseudogap near the phase transition could be possible near the MIT[102]. Further, variable range hopping (VRH) is also a possibility[103]. In this description, electron hopping is between Anderson localized states where hopping distance is correlated with the energy difference between the states. Further work needs to be done to assess whether any of these treatments of activation energy are applicable when transport is dominated by dynamic inhomogeneous current channels.

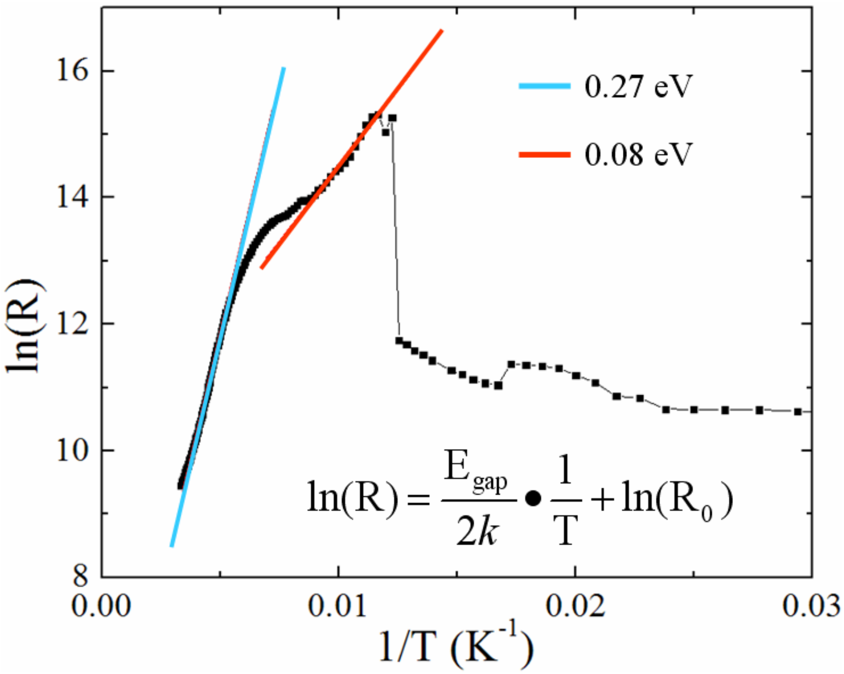

Figure 3-9: ln(R) vs 1/T showing activation energy fits for 10μm wire. Blue line is extrapolated from fit between 220 K and 170 K. Red line is extrapolated from fit between 115 K and 88 K. Fit lines extrapolated to show divergence points from linearity.

If the electronic phase domains are a truly emergent phenomenon based on the fine balance of spin-charge-lattice energies and not caused by seeding on large defect sites, we would expect that thermally cycling the wire would result in the fluctuations having a different character. This would be the case if the electronic phase domains were randomly seeded. Raising the temperature above the MIT would allow the thermal energy to, in effect, erase the emergent seeding locations. If the electronic domains were seeded on a large defect site whether from edge roughness, quenched chemical disordering, etc, the energy landscape of the wire would be such that the electronic phase domains would always seed at the same positions and have very similar character. As we discussed in Chapter 3.1, the location and character of the ultrasharp jumps at the MIT were shown to change with thermal cycling.

Now that we are capable of probing the transition of single electronic phase domains, we would expect that after thermal cycling the size and character of the fluctuations that we observe in time would be different. This would signal that the conduction channels had been rearranged. Figure 3-10 shows the effects of observed fluctuations under thermal cycling. This data shows resistivity vs. time scans at 85 K held at 3.75 T for three different thermal cycles. One thermal cycle is completed when the temperature is zero field cooled from 300 K to 10 K, magnetic filed is applied, temperature is raised to 85 K, and allowed to rest for 10 minutes before a resistivity vs. time measurement is conducted (shown in black). After 1 hour (shown in red), the same fluctuators are still visible and have the same characteristics. The three scan all show some form of fluctuator.

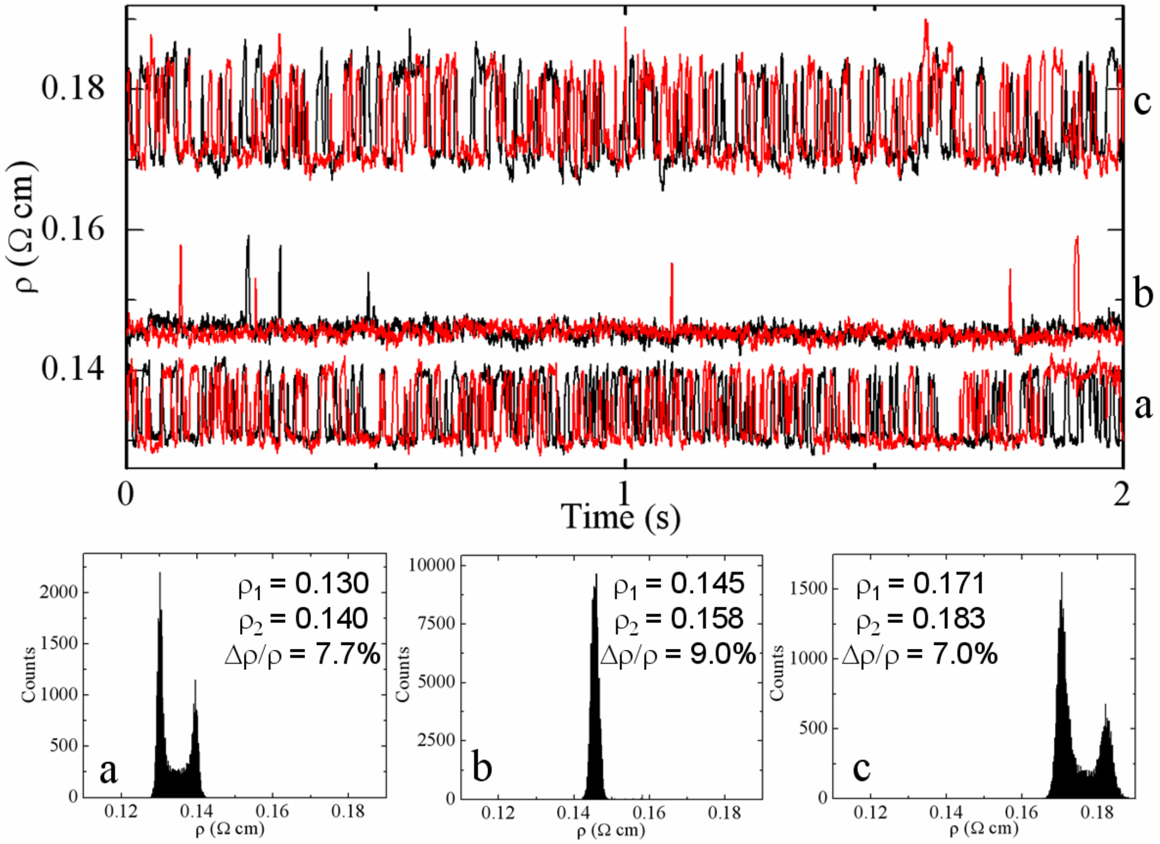

Figure 3-10: Effects of thermal cycling on fluctuators at 85 K. (**Top**) Wire resistivity at 85 K under 3.75 T magnetic field on three consecutive temperature cycles. Black plots show first scan. Red plots show scan after 1 hour. (**Bottom**) Binned values for both scans on each of three thermal cycles. The change in fluctuator character suggests that the formation of electronic phase domains is emergent and not due to large defects which would seed identical domains on every thermal cycle.

Though the measurements are taken at exactly the same temperature and field, the high and low resistivity values of the fluctuators are different as are their attempt frequencies for domain phase transition. This can be attributed to the observed fluctuating domains having different characteristics. By binning the values of the scans before and after 1 hour at the MIT, we see that they are still stable. The difference in Δρ/ρ found on each cycle is most likely caused by the fluctuating domains having different sizes—larger domains having bigger Δρ/ρ. The change in flipping attempt frequency suggests that the precise MIT temperatures of the observed domains are slightly different. Also the average ρ for each of the cycles is different which tells us that the conduction paths outside of the individual domains that are seen to fluctuate are also different. These differences allow us to reasonably assume that the formation of the observed domains is an emergent phenomenon based on the system's complexity and not from large seeding defect sites.

To better understand the observed resistance jumps in this system, we employ a random resistor model, which is widely used in modeling low-frequency resistance fluctuations[104,105]. Our system can be understood using only a few fluctuating resistors because only a small number of phase domains reside in the wire[98] (Figure 3-11a). In the simulation, nodal coordinates are randomly placed in a simulated wire and randomly linked by conductive connections. Subsequently, each of these nodes is assigned a random probability of switching between the open and closed state to simulate individual domain fluctuation. Figure 3-11b shows one such simulation in time-dependent resistivity. There is a clear 3 level fluctuation with a nested fluctuation in each level which is very similar to our experimental observations. This method was also used to simulate a 2D film by increasing the number of nodes to 1,000 and setting a periodic boundary condition in one direction perpendicular to the current to simulate an infinite film; it closely resembles our experimental data for the film (Figure 3-8b inset). The simulation confirms that the fluctuating resistance of the wires is a direct result of individual domains fluctuating between the metallic FMM phase and insulating COI phase.

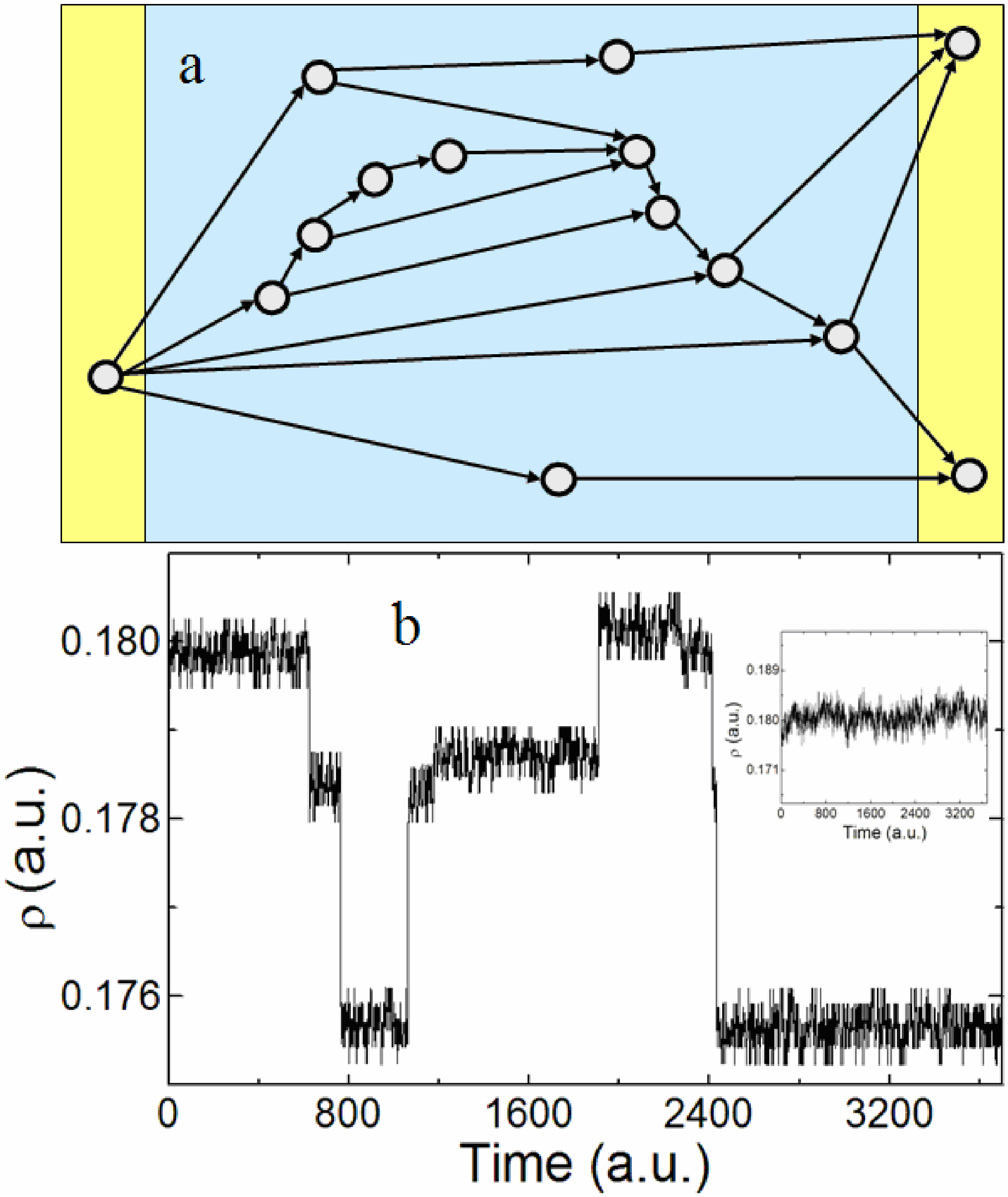

Figure 3-11: Random resistor network model. (**a**) Diagram of the model using a few node switches to simulate the random transition flippings of phase domains in a wire geometry. (**b**) Modeled data for the wire geometry showing discrete fluctuations that closely resemble the experimental data (**inset**: modeled network containing 1,000 nodes that closely matches the experimental results corresponding to films.) Note: arbitrary units are used.

The robust nature of these domains is illustrated in Figure 3-12 which shows two 10 second scans, taken 5 hours apart, with a resolution of 22 μs. The perfect consistency of these resistance traces show that even after > 5 hrs at the transition temperature, the exact same microscopic parts of the material are still fluctuating between the COI and FMM phases--intermittently blocking and opening local conductivity paths. Moreover, the very same two-level fluctuator still randomly switches between its two states that are apparently degenerate within k_BT. Thus, both the global configuration of COI and FMM domains and their microscopic configuration are in (thermal) equilibrium.

A more detailed look at the resistivity fluctuations shows that the jumps can be characterized by an inverse exponential shift between states (Figure 3-8b). This is true for all observed phase fluctuations--the three large shifts and the two level fluctuations nested within them. The lifetimes of all transitions are between 1 and 2 ms. The transition time is similar regardless of the magnitude of the resistivity change. It should be pointed out that these transition times are far longer than the response time of the electronics used to collect the data. Capacitive charging within the system can also be ruled out since these measurements are done using constant current which would result in a linear charging characteristic (V(t)) in a RC system. Clearly, the intrinsic switching speed of individual domains between the two respective phases is accessible in this experiment.

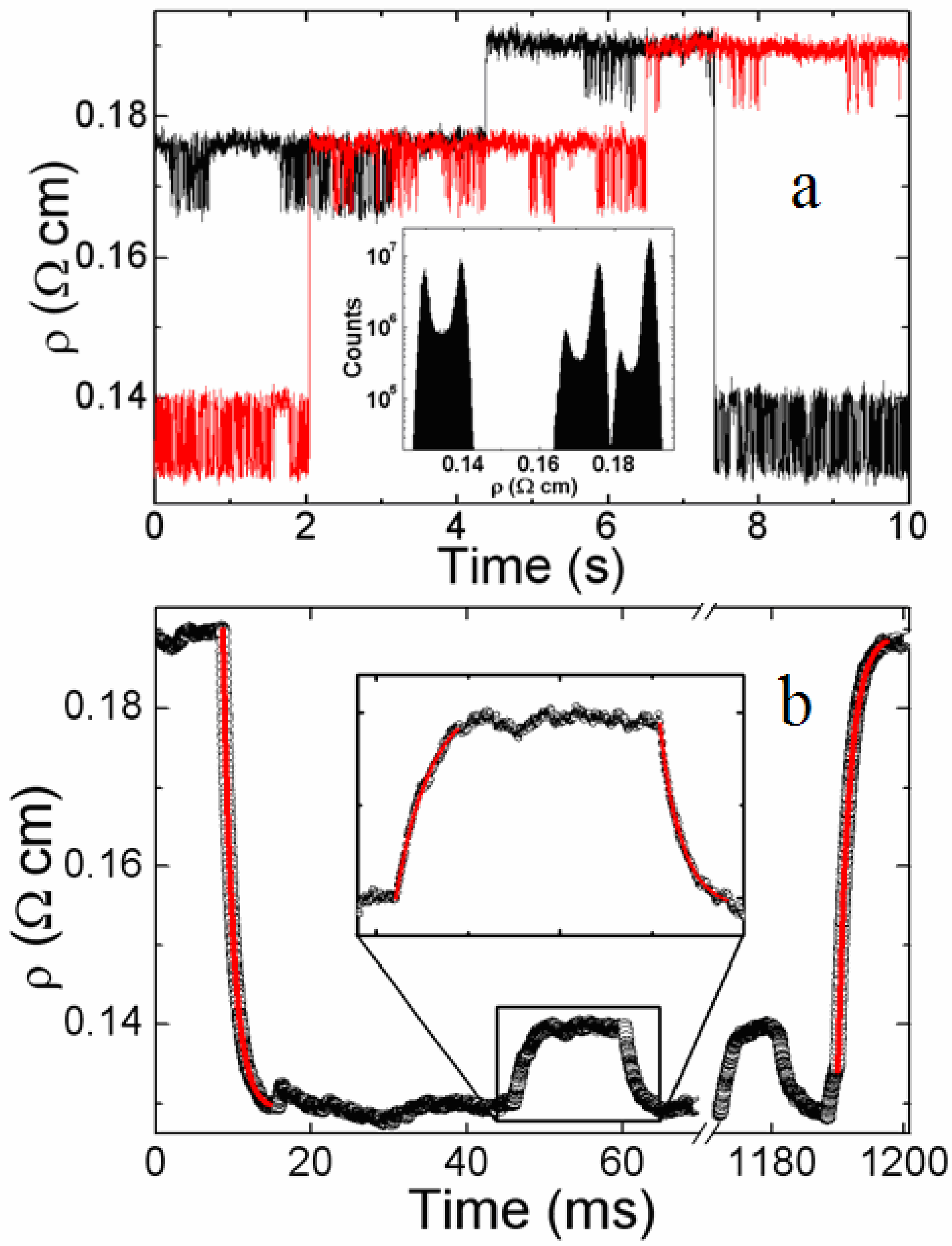

Figure 3-12: High frequency transport data on 10 μm wire held at MIT. (**a**) Comparison of 10 seconds worth of data taken 1 hour after the critical temperature was reached (black) and 6 hours after the critical temperature was reached (red) (inset: histogram of all data points taken over a 7 hour period.) (**b**) Examples of transition behaviors for both large and small fluctuations. Red lines indicate inverse exponential fits.

By binning all recorded resistivity values taken over a 6 hour period, a more precise view of the three distinct fluctuation levels and the nested two-state fluctuations can be obtained (Figure 3-12a, inset). The nested two-state fluctuation is created by a single domain that is actively fluctuating with a higher frequency throughout the measurement process than those that cause the larger changes in resistivity. Further, the data show that the nested two-state fluctuations have a changing asymmetric preference that is dependent on the state of the other domains in the wire. The microscopic fraction of material that fluctuates in the two level system spends a greater amount of time in the high resistance COI phase when other domains are also in the charge ordered insulating phase. This correlation between domains is most likely mediated by changes in the strain field. Changes in the strain field within manganites are known to cause changes in the transition temperature[4,59,61]. Indeed, the change in observed asymmetry is consistent with what would be expected if a single domain's transition temperature was to change very slightly while the system was held at a constant temperature. The symmetry breaking of the structure of the unit cell associated with the transition from one phase to another could explain the observed asymmetry in occupancy of the two-level fluctuators. As one domain fluctuates to a different phase, it induces a change in the local strain field that either modifies the total energy of a nearby phase domain or produces asymmetric energy barriers associated with a fluctuation in this nearby domain. This resembles the behavior of nanoscale metallic systems in which a single or few correlated atomic defects acting as fluctuators can generate abrupt changes in resistance[106,107].

The presence of two state fluctuations has been reported in other manganite systems[108-114]. These fluctuations are in some cases attributed to single electronic phase domain fluctuation. The large fluctuations that were reported in polycrystalline and single crystal thin films of LPCMO[111] were attributed to percolation; however the two state fluctuators were only observed with no applied magnetic field. Without an applied field over 1 T, magnetic domains are still present and were the most likely cause of the observed fluctuations[109]. In our work, we see no evidence of large fluctuations in the single crystal film geometry under an applied magnetic field over 1 T. Work done of LCMO[110,112] wires of varying widths ranging from 200 μm to 2 μm have also shown relatively large jumps in resistivity that were attributed to single domain fluctuations blocking the conduction lanes. There are several differences between these systems and our LPCMO wires. The electronic phase domains in half doped LCMO are typically on the order of 10 nm which is much smaller than the width of the wires used in the LCMO studies[115]. Considering relative wire width to domain size, the 2 μm LCMO wire would be roughly the equivalent of a 200 μm LPCMO wire. We do not see any fluctuators in such large LPCMO wires. The 2-state fluctuators in LCMO are also observed over a much wider temperature range between 15 K and 167 K. We do not see any fluctuators outside of the MIT window between 90 K and 70 K. This suggests that the fluctuations observed in LCMO are different than those observed in LPCMO and may not be the result of single electronic domain fluctuation.

The two state fluctuations that we observe can be and, in other manganite systems, often are treated in terms of random telegraph noise (RTN). RTN has been widely studied as a means of understanding background 1/f noise in electronic devices. RTN in metallic and semiconductor systems is caused by the capture and emission of individual carriers in defect sites which leads to the characteristic discrete switching between high and low resistive states[116]. After reducing the active electronic volume of metal or semiconducting devices, it is possible to isolate a single defect with a small number of carriers. This technique has not only been used to understand defect interactions at interfaces but to show that RTN could be the fundamental ingredient in 1/f noise in macroscopic devices. While clear 2-state RTN behavior is only seen in very small device sizes in metals and semiconductors, electronic phase separated materials can exhibit RTN in much larger systems and at much greater magnitude. Its source is attributed to domain fluctuations as discussed above. In the works on manganites that use the RTN treatment, the fluctuations are treated as random telegraph noise and analyzed using the normalized power spectrum of the Fourier transforms of recorded signals at specific fields and temperatures. Along these lines, our results are even more impressive, as the largest $\Delta\rho/\rho$ between two state fluctuators observed under a high magnetic field in other studies is less than 0.5% and have normalized power spectral densities on the order of 1×10^{-7} Hz^{-1}. As shown in Figure 3-8c, we have observed regular $\Delta\rho/\rho$ values of up to 46%. Taking normalized power spectral densities of the two state fluctuators residing in each of the three main resistive levels, we find values on the order of $1\text{x}10^{-5}$ Hz^{-1}. These values are orders higher than any reported metallic system or single crystal oxide thin film exhibiting giant random telegraph noise[110-112,116] and might therefore require a new designation as colossal random telegraph noise [Figure 3-13].

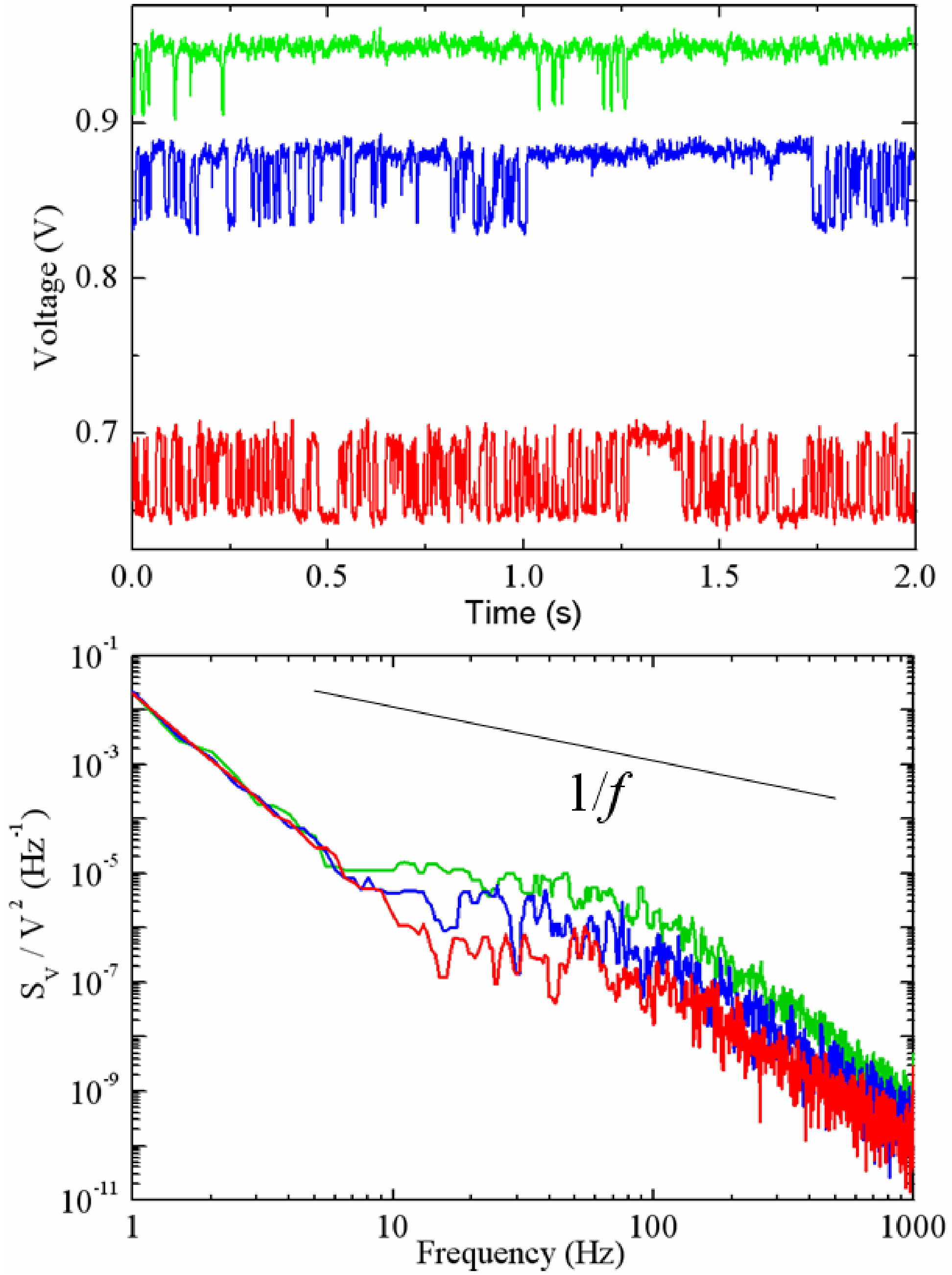

Figure 3-13: Comparison of the two state fluctuator on each of the three resistive levels and their respective normalized power spectral densities.

These experimental findings shed light on the nature of phase formation and behavior during phase transitions. We have made several new observations. All of the reported behaviors are only seen within a narrow window balanced at the transition temperature in narrow wires containing a small number of phase domains. It appears that the metal-insulator transition is not a smooth process in which all domains undergo a universal and smooth transition; instead finite regions individually flip from the metallic to the insulating phase. The asymmetric occupancy of the nested fluctuations shows that there are correlations between domains which could be mediated by asymmetries induced in the local strain fields created by phase fluctuations in neighboring domains. These observations should help us further understand the underpinnings of phase separation and first order phase transitions in complex oxides. Finally, the generic quality of our spatial confinement technique means that it is not limited to the model system presented here; it should be equally useful in studying other systems where phase separation plays a role in influencing unusual electronic properties.

Chapter 4 Ongoing and Future Work

4.1 Lattice Distortions at MIT

The strong spin-lattice-charge interactions in transition metal oxides are well documented and can lead to magnetic and electronic phase separation (PS) despite having a single crystal structure. In the work presented in previous chapters, we investigated the nature of PS through transport measurements on spatially confined structures. We were able to find very compelling evidence that chemical pressure and lattice strain could be varied to effectively tune the MIT of electronic phase domains. From this, it is necessary to do a more detailed study of the physical structure of the lattice and the role of physical changes to the lattice that may take place in the film or the substrate at or near MIT. To do this we are currently using two beamlines at Argonne National Laboratory's Advanced Photon Source.

To obtain high resolution scans across a wide temperature range, we are using the 33BM beamline. Here, a monochromatic X-ray beam with an energy of 8.4 keV is used with a standard Huber 4-circle diffractometer and a diplex cryostat capable of sample temperature control down to 10 K. This gives us the ability to recognize physical phase transitions that occur in either the film or substrate across a wide temperature range.

Initial results show that both STO and LAO substrates undergo orthorhombic distortion upon cooling. The fact that both STO and LAO are widely used to study the effects of strain on manganite films makes this information vital in understanding the mechanisms of phase separation. Figure 4-1 shows that near the MIT the STO substrate undergoes orthorhombic distortion which adds additional in plane and out of plane strain to the LPCMO film. The H-L mesh scan in reciprocal space shows that the film is not commensurate in-plane with the STO substrate—having a difference of ~1%. We also see that the LPCMO film is slightly orthogonal with a c/a value of roughly 2%. In polycrystalline LPCMO, a natural tendency to distort along the a and c axes at the MIT has been shown[117]. The transport and magnetic properties of manganite films are known to be linked to the type of substrate onto which they are grown[61]. In order to better understand the basic mechanisms at play in influencing PS and the MIT we must take into account all influences from the substrate, as distortion in different planes will have various effects on the transport between octahedra.

X-ray diffraction is a powerful tool in mapping crystalline structure; however it is limited by the fact that it takes its measurements as averages over relatively large regions of several millimeters. Beamline 34ID at the APS uses lensing to reduce the beam size to about 500 nm. Since the size of the electronic phase domains in LPCMO are on the order of microns, the reduced beam size offers us a possible method of recognizing local variations in lattice structure that can then be tied directly to variations in transport properties arising from PS.

For the preliminary results discussed here, the incident beam size was roughly 1 μm in diameter. Future measurements will reduce the beam size by roughly ½. We used tunable Si double-crystal monochromator to reduce the polychromatic incident X-ray beam to a single monochromatic beam of 8 keV. This was necessary, as polychromatic light creates Laue diffraction patterns that are too strongly dominated by the substrate

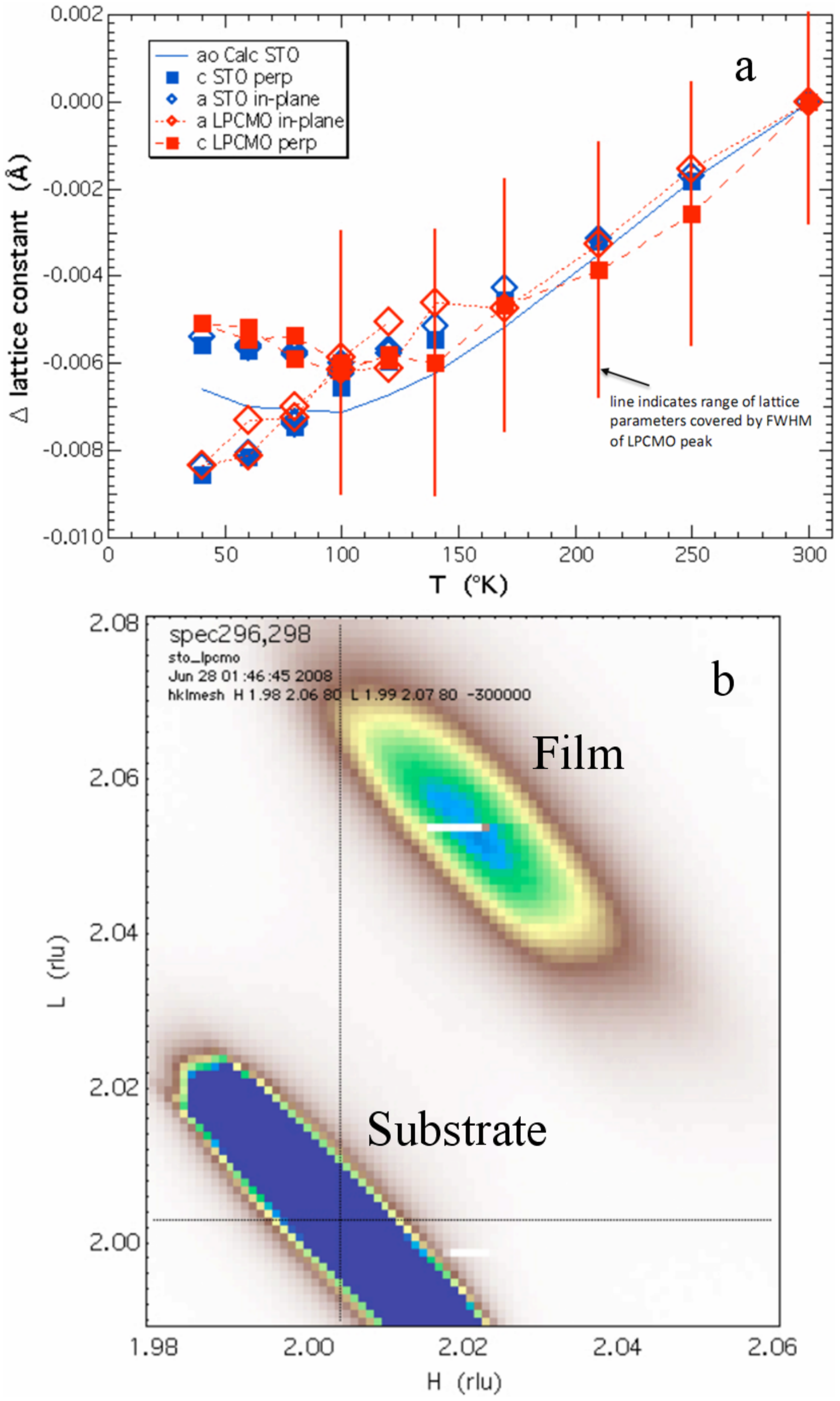

Figure 4-1: LPCMO on STO change in lattice parameters across temperature. (**a**)Shift in lattice parameters across temperature. (**b**)H-L mesh scan in reciprocal space for LPCMO on STO taken at 60 K.

peaks to separate out the weaker film peaks. The samples were mounted on a Joule-Thomson gas expansion cryostage capable of temperatures down to 80 K with liquid nitrogen.

Spatial maps of LPCMO (004) on SLGO were made at room temperature and 84 K [Figure 4-2]. Though there were no measurable variations in the lattice parameters between the temperatures, the Bragg peaks at low temperature were weaker and showed angle broadening. Typically, a crystal will have stronger and sharper Bragg peaks at lower temperature from the reduction of atomic vibrations—Debye-Waller factor. From this, we surmise that the there are local variations of strain that take place at low

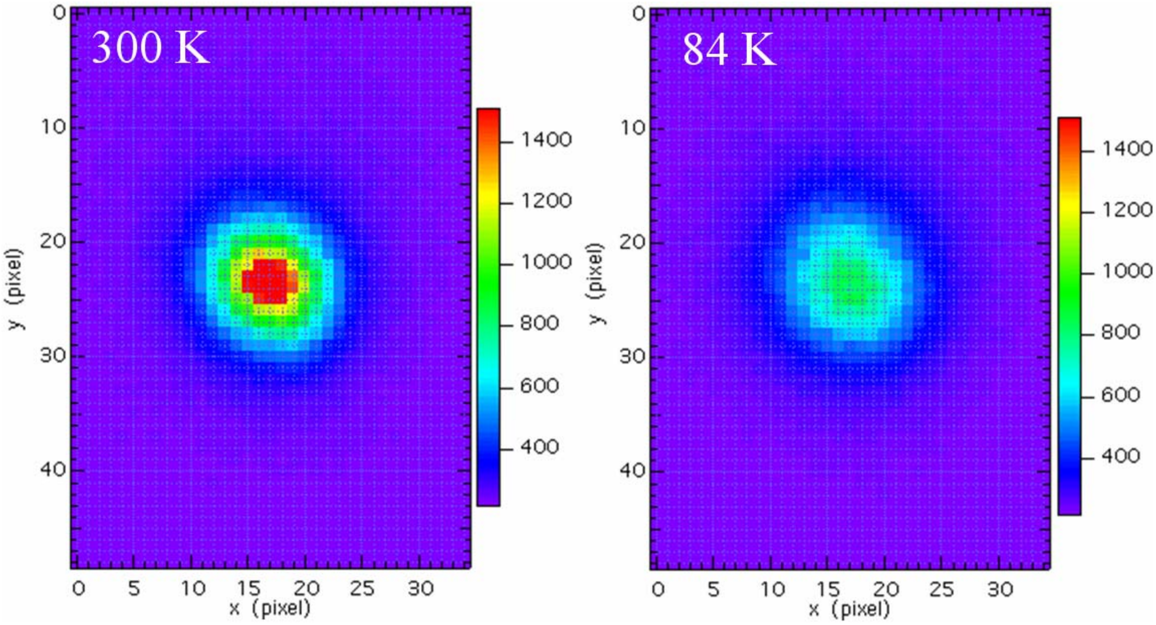

Figure 4-2: 15 μm LPCMO dot imaged using microdiffration XRD. Each pixel is equivalent to 1 μm. The color gradient indicates the number of counts at a set angle and wavelength. The low temperature measurement shows a spread in angle and a decrease in intensity.

temperature but that the resolution of the beam was not quite adequate in these initial results to directly resolve them. Future scans with improved resolution are planned.

Continued work with the APS promises to help us further understand the structural contributions from lattice as it relates to PS and CMR. The results to this point, though not complete, suggest that substrate effects and physical phase transitions in the film may play a larger role in thin film TMO's electronic and magnetic properties than current models take into account.

4.2 Controlled Interfacial Doping Effects

To study disorder of charge carrier dopants and self-organization caused by intrinsic elastic energy, we have grown epitaxial superlattice structures of $La_{1-x}Ca_xMnO_3$ (LCMO) / $Pr_{1-x}Ca_xMnO_3$ (PCMO) for comparison to the known bulk properties of $(La_{1-y}Pr_y)_{1-x}Ca_xMnO_3$. We have experimented with both traditional superlattice structures and a novel approach of creating vertical superlattices [Figure **4-3**].

Our intention is to probe the interplay of carrier dopants and inherent elastic energy between materials to help us more fully understand the subtle balance and competition between the different electronic phases. For the traditional superlattice structures, we varied stacking period depths in $La_{5/8}Ca_{3/8}MnO_3$ / $Pr_{5/8}Ca_{3/8}MnO_3$ by an integer number. We selected this doping since T_c is optimized for x = 3/8 in $La_{1-x}Ca_xMnO_3$. For comparison, we also created disordered $La_{5/16}Pr_{5/16}Ca_{3/8}MnO_3$ having the same overall film thickness as the superlattice structures. Growing superlattice structures of LCMO/PCMO with varied stacking periods but equal overall stoichiometry to

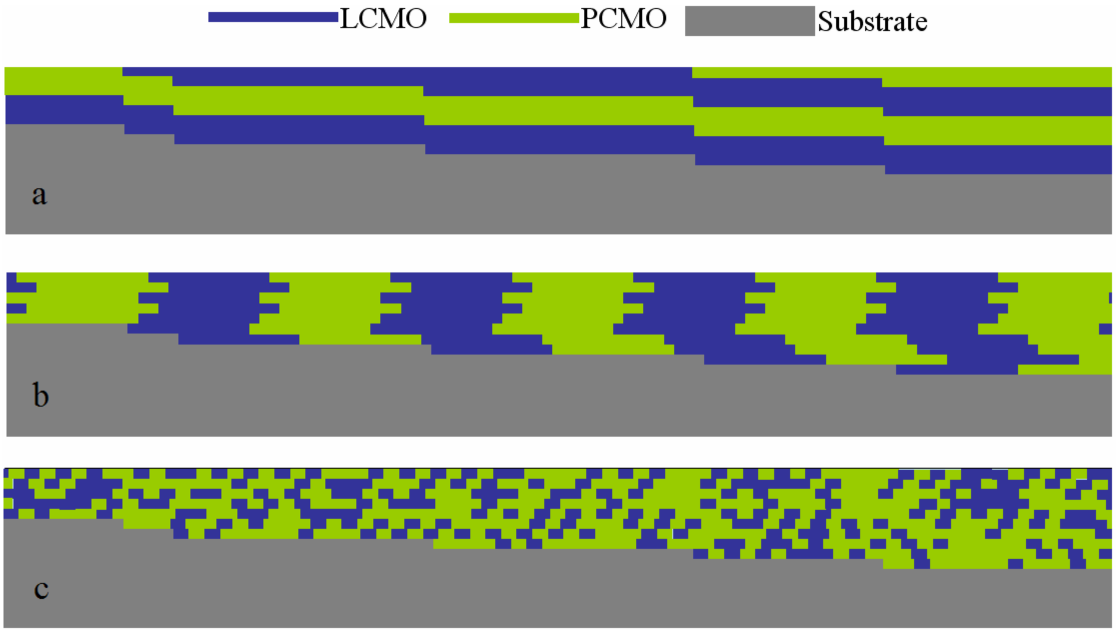

Figure 4-3: Examples of superlattice structures. (**a**) Traditional superlattice. (**b**) Vertical superlattice. (**c**) Disordered.

disordered LPCMO allows us to compare the interfacial elastic energy landscape through the chemical ordering of La / Pr at the in-plane interface. In this experiment, we have grown several different structures in an ABAB…AB repetition where A = x monolayers of LCMO and B = x monolayers of PCMO. Superlattice samples with x = 4, 8, 16, 32 have been grown and inspected with four-circle XRD. Figure 4-4 shows these results and confirms the presence epitaxial superlattice structures.

We would expect that as x → 1 the superlattices will approach the properties of the disordered LPCMO and that as x → 32 the superlattice will begin to behave as a combination of bulk PCMO and bulk LCMO. Our initial magnetization results show that this may not necessarily be the case [Figure 4-5]. We observe that a higher

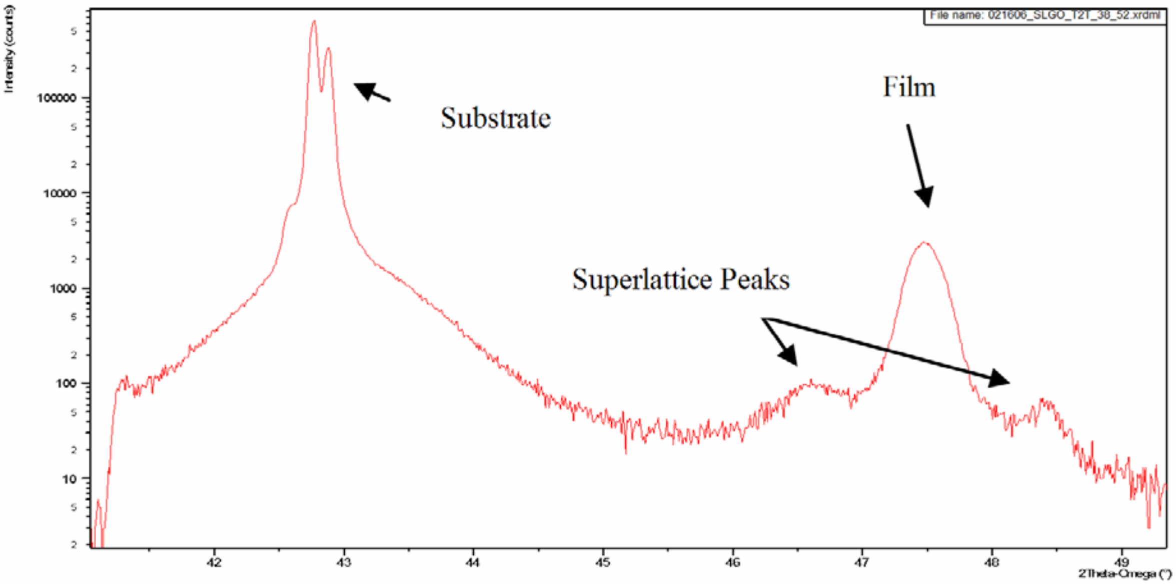

Figure 4-4: XRD of LPCMO on SLGO. (002) peaks showing substrate and superlattice structure.

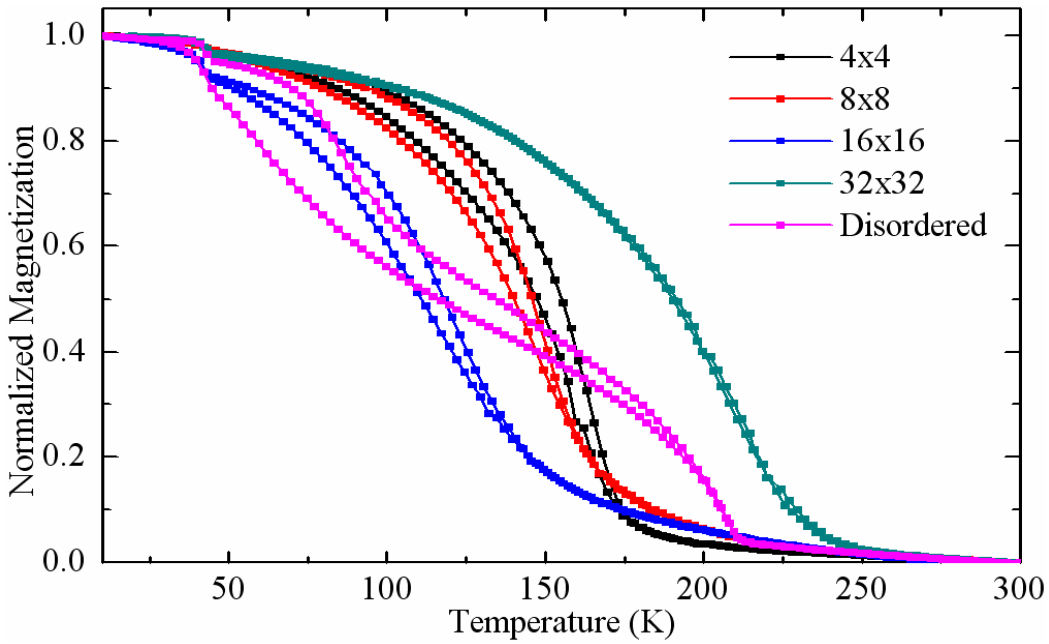

Figure 4-5: Normalized magnetization for various superlattice structures and disordered LPCMO.

magnetization in the 4 x 4 and 8 x 8 superlattices is maintained at higher temperatures than the disordered LPCMO while hysteresis is extinguished at a lower temperature than in the disordered. For the 32 x 32 superlattice, no hysteresis is observed which is surprising as LCMO should have a noticeable ferromagnetic component. Hysteresis for all superlattices disappears at lower temperatures than for the disordered film. It appears that there is a relation between the point at which hysteresis disappears and layer thickness. These results seem to suggest increased La / Pr interaction at the in-plane interface have a substantial influence on the overall magnetization of the sample. In this experimental arrangement we are only controlling the amount of La / Pr interaction in-plane with the substrate. To observe La / Pr interaction relative perpendicular to the substrate plane we must take a different approach.

By growing regular fractional multiples of a single monolayer we can effectively create vertical superlattice towers. While this does not reduce in-plane La / Pr interaction to the degree that tradition superlattices reduce the out-of-plane La / Pr interaction, it does offer much higher in-plane vs. out-of-plane interaction ratio. To do this, we again use $La_{5/8}Ca_{3/8}MnO_3$ / $Pr_{5/8}Ca_{3/8}MnO_3$ but in a ½ monolayer x ½ monolayer configuration [Figure 4-3b]. ½ monolayer growth can be controlled by closely monitored the RHEED during sample synthesis.

Figure 4-5 shows normalized magnetization vs. temperature plots for disordered LPCMO, a traditional superlattice in an 8 x 8 configuration and a vertical superlattice. All films have the same total thickness and overall stoichiometry. The 8 x 8 superlattice was selected because it has roughly the same thickness ratio out-of-plane as the vertical superlattice has in-plane. We see that the vertical superlattice tower configuration has a much more pronounced hysteresis than the traditional superlattice or the disordered film; it also more closely matches the disordered film than any of the traditional superlattices. Similar to the disordered LPCMO film, the vertical superlattice shows hysteresis up to 200 K. This seems to suggest that for thin films in-plane La/Pr interaction is more important than out-of-plane La/Pr interaction in controlling stable phase separation. Follow up work will include changing tower widths and conducting transport measurements.

Finally, we have begun studies that vary the stacking ratio in traditional superlattices to ABAB…AB where A = x monolayers of LCMO and B = y monolayers of PCMO. Our intention is to maintain control over the elastic energy at the interface while tuning the amount of stress between layers in order to study the effects of shifting the electronic states through shifting the ratio of La / Pr. By having x>>y, the LCMO layer will be able to more fully relax while the PCMO layer will be held under a slight tensile strain caused by the slight lattice mismatch between LCMO and PCMO, 0.386 nm /unit cell and 0.382 nm / unit cell respectively. We already know that transport and magnetization are sensitive to substrate strain[61,59] so this method offers an interesting approach to spreading the strain throughout the film.

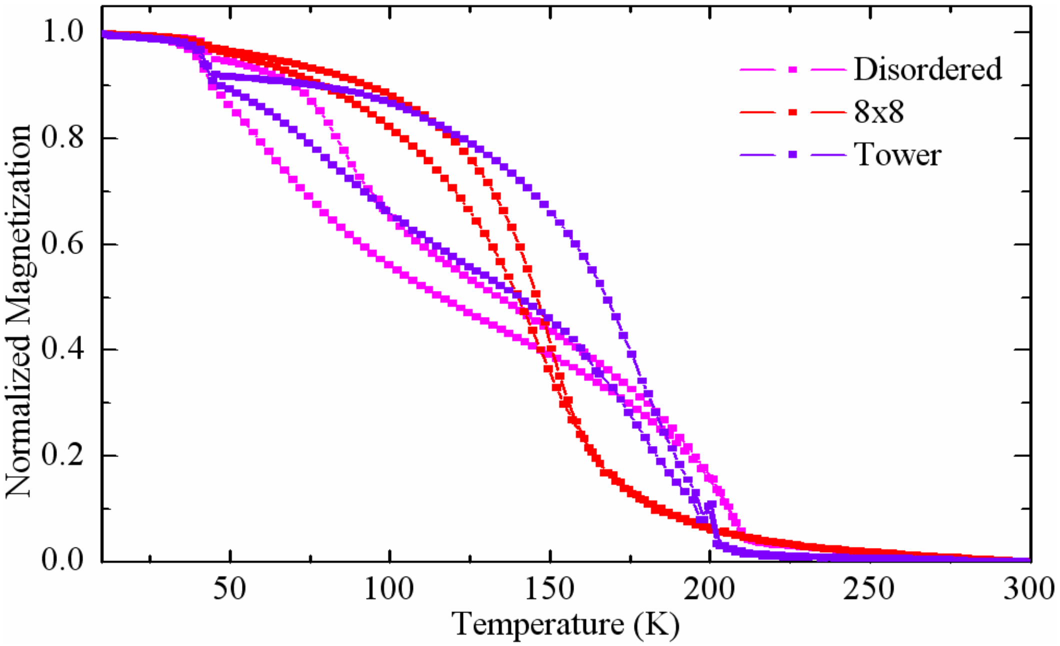

Figure 4-6: Normalized magnetization for traditional 8 x 8 horizontal superlattice, vertical tower superlattice and disordered LPCMO film. All films have same total thickness.

4.3 Concluding Remarks

Complexity can be found all around us. The idea that many inseparable and interacting components can contribute to make complex emergent phenomena is a fascinating concept. The work presented in this dissertation is a necessary first step in attempting to bridge the complex behaviors of quantum devices with the emergent phenomena associated with complex materials.

We have selected $La_{1-y-x}Pr_xCa_yMnO_3$ as our model material, because many different works suggest that it has emergent electronic phase separation at transition on the order of microns. At this scale, growth methods such as laser MBE can be used to grow samples that are sufficiently chemically disordered (random alloy) in a single crystalline structure to insure any observed phase separation is a phenomena based on complexity and not on quenched disorder. For this reason, previous studies on phase separation that use materials with proposed electronic phase domain sizes on the order of a few nanometers such as $La_{1-x}Ca_xMnO_3$ are not appropriate for studying emergent electronic phase separation.

Previous works that claim to image electronic phase separation in manganites using surface probing methods are not suitable for monitoring the behavior of phase separation. This is due to the fact that surfaces can have vastly different properties from bulk. Averaging methods such as neutron diffraction and Mossbauer spectroscopy are also unsuitable for studying single electronic phase domain behavior, as the averaging component reduces the temporal and spatial resolution needed to study a single small region as it undergoes phase transition. Previous studies using transport measurements on bulk and thin films are not limited to probing the surface but, like other averaging methods, the signal is unable to probe local regions with a sufficient resolution, as the electrons will follow the path of least resistance thereby leaving high resistance regions hidden if there is a parallel channel having a higher conductivity. However, by spatially confining a structure, so that parallel conducting channels are removed, it is possible to remove this impediment.

For these reasons, we have studied spatially confined LPCMO. The large scale of the emergent electronic phase domains inherent in LPCMO are easily reached with fairly simple lithographic techniques. In this configuration, transport measurements lose their averaging component and allow us to create a serial resistive network in which multiple electronic phase domains can be probed. Changes in a single node along the serial chain have a dominant effect on the signal which allows us to probe multiple regions independently and has the added benefit of allowing us to probe with a very high temporal resolution only limited by the quality of our electronics.

We have observed several new phenomena that shed light on emergent behavior in manganites. We have shown that by reducing the size of a device to the scale of its inherent electronic phase domains it is possible to observe the exact temperature at which single domains undergo the metal-insulator transition; this is observed as a previously unseen ultrasharp peak in the resistivity vs. temperature scans. Spatial confinement has also allowed us to study complex interactions between chemical pressure and substrate induced strain that influence electronic phase separation and phase transition; we showed that these parameters can be tuned to induce a reemergent metal-insulator transition and noted that this effect, while present, had never been observed in previous studies of any phase separated material.

With the ability to probe a single or few domains, we turned our attention to the dynamics of electronic phase transitions. By carefully balancing at the metal-insulator transition, we were able to observe the first ever stable single electronic phase domain fluctuations. From this, we were able to conclude that as LPCMO undergoes the metal-insulator transition finite regions undergo reversible first order phase transitions that can be modeled as a complex switching network. The differences in fluctuation character were interpreted as the observed fluctuators having slightly different transition temperatures. This is the first experimental evidence that the metal-insulator transition of a manganite is actually comprised of many single domains transitioning at slightly different temperatures across a wide region. We also showed that as phase domains fluctuate they influence other domains in the conduction path—possibly through changes to the strain or electric fields. The emergent behavior involved in the formation of electronic phase separated domains was also confirmed with the observation that thermal cycling seeded domains of varying character.

The work presented in this dissertation offers new information on emergent phenomena in complex materials while demonstrating the ability of reduced dimensionality to produce new qualitative behaviors even in well studied materials. Future research along these lines promises many new discoveries that will be vital in helping us unravel the physics of complex materials.

References

1. Bhalla, A.S., Guo, R. & Roy, R. The perovskite structure – a review of its role in ceramic science and technology. *Materials Research Innovations* **4**, 3-26(2000).
2. Shenoy, V.B., Sarma, D.D. & Rao, C.N.R. Electronic phase separation in correlated oxides: the phenomenon, its present status and future prospects. *Chemphyschem* **7**, 2053-9(2006).
3. Ramakrishnan, T.V. et al. Theory of Insulator Metal Transition and Colossal Magnetoresistance in Doped Manganites. *Phys. Rev. Lett.* **92**, 157203(2004).
4. Uehara, M. et al. Percolative phase separation underlies colossal magnetoresistance in mixed-valent manganites. *Nature* **399**, 560-563(1999).
5. Israel, C., Calderon, M.J. & Mathur, N.D. The current spin on manganites. *Materials Today* **10**, 24-32(2007).
6. Zurauskiene, N. Thin manganite films for fast fault current limiter applications. *Thin Solid Films* **515**, 576-579(2006).
7. Guillet, B. et al. Net of YBCO and LSMO Thermometers for Bolometric Applications. *Advanced Experimental Methods For Noise Research in Nanoscale Electronic Devices* **151**, 327-336(2005).
8. Imada, M., Fujimori, A. & Tokura, Y. Metal-insulator Transitions. *Reviews of Modern Physics* **70**, 1039(1998).
9. Millis, A.J., Shraiman, B.I. & Mueller, R. Dynamic Jahn-Teller Effect and Colossal Magnetoresistance in La1-xSrxMnO3. *Phys. Rev. Lett.* **77**, 175(1996).
10. Millis, A.J. Lattice effects in magnetoresistive manganese perovskites. *Nature* **392**, 147-150(1998).
11. Millis, A.J., Mueller, R. & Shraiman, B.I. Fermi-liquid-to-polaron crossover. II. Double exchange and the physics of colossal magnetoresistance. *Phys. Rev. B* **54**, 5405(1996).
12. Neumeier, J.J. et al. Substantial pressure effects on the electrical resistivity and ferromagnetic transition temperature of La1-xCaxMnO3. *Phys. Rev. B* **52**, R7006(1995).
13. Zener, C. Interaction Between the d Shells in the Transition Metals. *Phys. Rev.* **81**, 440(1951).
14. Zener, C. Interaction between the d-Shells in the Transition Metals. II. Ferromagnetic Compounds of Manganese with Perovskite Structure. *Phys. Rev.* **82**, 403(1951).
15. Anderson, P.W. & Hasegawa, H. Considerations on Double Exchange. *Phys. Rev.* **100**, 675(1955).
16. Alexandrov, A.S. & Bratkovsky, A.M. Carrier Density Collapse and Colossal Magnetoresistance in Doped Manganites. *Phys. Rev. Lett.* **82**, 141(1999).
17. Goodenough, J.B. Theory of the Role of Covalence in the Perovskite-Type Manganites [La, M(II)]MnO3. *Phys. Rev.* **100**, 564(1955).

18. Furukawa, N. Transport Properties of the Kondo Lattice Model in the Limit S=∞ and D=∞. *J. Phys. Soc. Jpn.* **63**, 3214-3217(1994).

19. de Gennes, P.G. Effects of Double Exchange in Magnetic Crystals. *Phys. Rev.* **118**, 141(1960).

20. Millis, A.J. Cooperative Jahn-Teller effect and electron-phonon coupling in La1-xAxMnO3. *Phys. Rev. B* **53**, 8434(1996).

21. Siwach, P.K., Singh, H.K. & Srivastava, O.N. Low field magnetotransport in manganites. *Journal of Physics: Condensed Matter* **20**, 273201(2008).

22. Millis, A.J., Mueller, R. & Shraiman, B.I. Fermi-liquid-to-polaron crossover. I. General results. *Phys. Rev. B* **54**, 5389(1996).

23. Ziese, M. & Srinitiwarawong, C. Polaronic effects on the resistivity of manganite thin films. *Phys. Rev. B* **58**, 11519(1998).

24. Adams, C.P. et al. Charge Ordering and Polaron Formation in the Magnetoresistive Oxide La0.7Ca0.3MnO3. *Phys. Rev. Lett.* **85**, 3954(2000).

25. Quijada, M. et al. Optical conductivity of manganites: Crossover from Jahn-Teller small polaron to coherent transport in the ferromagnetic state. *Phys. Rev. B* **58**, 16093(1998).

26. Kiryukhin, V. et al. Average lattice symmetry and nanoscale structural correlations in magnetoresistive manganites. *Phys. Rev. B* **67**, 064421(2003).

27. Jirak, Z. et al. Neutron diffraction study of Pr1 − xCaxMnO3 perovskites. *Journal of Magnetism and Magnetic Materials* **53**, 153-166(1985).

28. Jonker, G. Semiconducting properties of mixed crystals with perovskite structure. *Physica* **20**, 1118-1122(1954).

29. Mori, S., Chen, C.H. & Cheong, S. Pairing of charge-ordered stripes in (La,Ca)MnO3. *Nature* **392**, 473-476(1998).

30. Ramirez, A.P. et al. Thermodynamic and Electron Diffraction Signatures of Charge and Spin Ordering in La1-xCaxMnO3. *Phys. Rev. Lett.* **76**, 3188(1996).

31. Loudon, J.C., Mathur, N.D. & Midgley, P.A. Charge-ordered ferromagnetic phase in La0.5Ca0.5MnO3. *Nature* **420**, 797-800(2002).

32. Mori, S., Asaka, T. & Matsui, Y. Observation of magnetic domain structure in phase-separated manganites by Lorentz electron microscopy. *J Electron Microsc (Tokyo)* **51**, 225-229(2002).

33. Kuhns, P.L. et al. Magnetic Phase Separation in La1-xSrxCoO3 by Co59 Nuclear Magnetic Resonance. *Phys. Rev. Lett.* **91**, 127202(2003).

34. Vanitha, P.V., Nagarajan, R. & Rao, C.N.R. A 57Fe Mossbauer study of charge ordering and phase separation in the rare-earth manganates, Nd0.5Ca0.5MnO3 and Nd0.5Sr0.5MnO3. *Journal of Solid State Chemistry France* **174**, 74-79(2003).

35. Moshnyaga, V. et al. Structural phase transition at the percolation threshold in epitaxial (La0.7Ca0.3MnO3)1-x:(MgO)x nanocomposite films. *Nature Materials* **2**, 247-252(2003).

36. Ritter, C. et al. Structural and magnetic properties of double perovskites AA'FeMoO6 (AA' = Ba2, BaSr, Sr2 and Ca2). *Journal of Physics: Condensed Matter* **12**, 8295-8308(2000).

37. Wu, W. et al. Magnetic imaging of a supercooling glass transition in a weakly disordered ferromagnet. *Nat Mater* **5**, 881-886(2006).

38. Israel, C. et al. Translating reproducible phase-separated texture in manganites into reproducible two-state low-field magnetoresistance: An imaging and transport study. *Phys. Rev. B* **78**, 054409-5(2008).

39. Fäth, M. et al. Spatially Inhomogeneous Metal-Insulator Transition in Doped Manganites. *Science* **285**, 1540-1542(1999).

40. Wollan, E.O. & Koehler, W.C. Neutron Diffraction Study of the Magnetic Properties of the Series of Perovskite-Type Compounds [(1-x)La, xCa]MnO3. *Phys. Rev.* **100**, 545(1955).

41. Bhide, V.G. et al. Itinerant-electron ferromagnetism in La1-xSrxCoO3: A Mossbauer study. *Phys. Rev. B* **12**, 2832-2843(1975).

42. Pan, S.H. et al. Microscopic electronic inhomogeneity in the high-Tc superconductor Bi2Sr2CaCu2O8. *Nature* **413**, 282-285(2001).

43. Lang, K.M. et al. Imaging the granular structure of high-Tc superconductivity in underdoped Bi2Sr2CaCu2O8. *Nature* **415**, 412-416(2002).

44. Tranquada, J.M. et al. Evidence for stripe correlations of spins and holes in copper oxide superconductors. *Nature* **375**, 561-563(1995).

45. Bozin, E.S. et al. Neutron Diffraction Evidence of Microscopic Charge Inhomogeneities in theCuO2 Plane of Superconducting La2-xSrxCuO4. *Phys Rev Lett* **84**, 5856

46. de Mello, E.V.L. & Caixeiro, E.S. Effects of phase separation in the cuprate superconductors. *Phys. Rev. B* **70**, 224517(2004).

47. Tranquada, J.M. et al. Quantum magnetic excitations from stripes in copper oxide superconductors. *Nature* **429**, 534-538(2004).

48. Zhang, L. et al. Direct Observation of Percolation in a Manganite Thin Film. *Science* **298**, 805-807(2002).

49. Dulli, H. et al. Surface segregation and restructuring of colossal-magnetoresistant manganese perovskites La0.65Sr0.35MnO3. *Phys. Rev. B* **62**, R14629(2000).

50. Freeland, J.W. et al. Full bulk spin polarization and intrinsic tunnel barriers at the surface of layered manganites. *Nat Mater* **4**, 62-67(2005).

51. Reeland, J. et al. Suppressed magnetism at the surfaces and interfaces of manganites. *J. Phys: Condens. Matter* **19**, 315210(2007).

52. Bibes, M. et al. Surface-induced phase separation in manganites: A microscopic origin for powder magnetoresistance. *Appl. Phys. Lett.* **82**, 928-930(2003).
53. Chrisey, D.B. & Hubler, G.K. *Pulsed Laser Deposition of Thin Films*. 648(Wiley-Interscience: 1994).
54. Opik, E.J. The lunar atmosphere. *Planetary and Space Science* **9**, 211-244(1962).
55. Tersoff, J. & Hamann, D.R. Theory of the scanning tunneling microscope. *Phys. Rev. B* **31**, 805(1985).
56. Sarid, D. *Scanning Force Microscopy*. 263(Oxford University Press: 1994).
57. Putnis, A. *Introduction to Mineral Sciences*. 457(Cambridge University Press: 1992).
58. BRAGG, W. The Nature of γ and X-Rays. *Nature* **70**, 270(1908).
59. Ward, T.Z. et al. Reemergent Metal-Insulator Transitions in Manganites Exposed with Spatial Confinement. *Phys. Rev. Lett.* **100**, 247204-4(2008).
60. Zhai, H. et al. Giant Discrete Steps in Metal-Insulator Transition in Perovskite Manganite Wires. *Phys. Rev. Lett.* **97**, 167201-4(2006).
61. Gillaspie, D. et al. Influence of different substrates on phase separation in La1 - x - yPryCaxMnO3 thin films. *J. Appl. Phys.* **99**, 08S901-3(2006).
62. Praus, R.B. et al. Thickness dependent properties of La0.67Ca0.33MnO3 thin films. *Applied Surface Science* **138-139**, 40-43(1999).
63. Li, H., Sun, J.R. & Wong, H.K. Enhanced low-field magnetoresistance in La2/3Ca1/3MnO3 / Pr2/3Ca1/3MnO3 superlattices. *Appl. Phys. Lett.* **80**, 628-630(2002).
64. Dagotto, E., Hotta, T. & Moreo, A. Colossal magnetoresistant materials: the key role of phase separation. *Physics Reports* **344**, 1-3(2001).
65. Dagotto, E. Complexity in Strongly Correlated Electronic Systems. *Science* **309**, 257-262(2005).
66. Mahendiran, R. et al. Ultrasharp Magnetization Steps in Perovskite Manganites. *Phys. Rev. Lett.* **89**, 286602(2002).
67. Mao, Z.Q. et al. Phase Separation in the Itinerant Metamagnetic Transition of Sr4Ru3O10. *Phys. Rev. Lett.* **96**, 077205-4(2006).
68. Hebert, S. et al. Magnetic-Field-Induced Step-like Transitions in Mn-Site Doped Manganites. *Journal of Solid State Chemistry* **165**, 6-11(2002).
69. Kuwahara, H. et al. A First-Order Phase Transition Induced by a Magnetic Field. *Science* **270**, 961-963(1995).
70. Mathur, N. & Littlewood, P. Mesoscopic Texture in Manganites. *Physics Today* **56**, 25-30(2003).

71. Zhai, H. et al. Giant Discrete Steps in Metal-Insulator Transition in Perovskite Manganite Wires. *Physical Review Letters* **97**, 167201(2006).
72. Wu, T. & Mitchell, J.F. Creation and annihilation of conducting filaments in mesoscopic manganite structures. *Physical Review B* **74**, 214423(2006).
73. Teresa, J.M.D. et al. Evidence for magnetic polarons in the magnetoresistive perovskites. *Nature* **386**, 256-259(1997).
74. Adams, C.P. et al. Charge Ordering and Polaron Formation in the Magnetoresistive Oxide La0.7Ca0.3MnO3. *Phys. Rev. Lett.* **85**, 3954(2000).
75. Salamon, M.B. & Jaime, M. The physics of manganites: Structure and transport. *Rev. Mod. Phys.* **73**, 583(2001).
76. Argyriou, D.N. et al. Glass Transition in the Polaron Dynamics of Colossal Magnetoresistive Manganites. *Phys. Rev. Lett.* **89**, 036401(2002).
77. Ahn, K.H., Lookman, T. & Bishop, A.R. Strain-induced metal-insulator phase coexistence in perovskite manganites. *Nature* **428**, 401-404(2004).
78. Milward, G.C., Calderón, M.J. & Littlewood, P.B. Electronically soft phases in manganites. *Nature* **433**, 607-10(2005).
79. Mathieu, R. et al. Colossal Magnetoresistance without Phase Separation: Disorder-Induced Spin Glass State and Nanometer Scale Orbital-Charge Correlation in Half Doped Manganites. *Phys. Rev. Lett.* **93**, 227202(2004).
80. Sen, C., Alvarez, G. & Dagotto, E. Competing Ferromagnetic and Charge-Ordered States in Models for Manganites: The Origin of the Colossal Magnetoresistance Effect. *Phys. Rev. Lett.* **98**, 127202-4(2007).
81. Moreo et al. Giant cluster coexistence in doped manganites and other compounds. *Phys Rev Lett* **84**, 5568-71(2000).
82. Littlewood, P. Condensed-matter physics: Phases of resistance. *Nature* **399**, 529-531(1999).
83. Radaelli, P.G. et al. Mesoscopic and microscopic phase segregation in manganese perovskites. *Phys. Rev. B* **63**, 172419(2001).
84. Yanagisawa, Y. et al. Digitalized magnetoresistance observed in (La,Pr,Ca)MnO3 nanochannel structures. *Appl. Phys. Lett.* **89**, 253121-3(2006).
85. Tokura, Y. et al. Competing Instabilities and Metastable States in (Nd,Sm)1/2Sr1/2MnO3. *Phys. Rev. Lett.* **76**, 3184(1996).
86. Aliaga, H. et al. Theoretical study of half-doped models for manganites: Fragility of CE phase with disorder, two types of colossal magnetoresistance, and charge-ordered states for electron-doped materials. *Phys. Rev. B* **68**, 104405(2003).
87. Troyanchuk, I.O. et al. Phase transition in perovskites. *Journal of Physics: Condensed Matter* **10**, 7957-7966(1998).

88. San-Lin Young et al. Variation of magnetic and transport properties in magnetoresistive oxides La-ln-Pb-Mn-O (Ln=Pr, Nd, Dy, and Y). *Magnetics, IEEE Transactions on* **41**, 2754-2756(2005).

89. Mandal, P. & Das, S. Transport properties of Ce-doped RMnO3 (R=La, Pr, and Nd) manganites. *Phys. Rev. B* **56**, 15073(1997).

90. Lakshmi, L.S. et al. Double MITs and magnetoresistance: an intrinsic feature of Ru substituted La0.67Ca0.33MnO3. *Journal of Physics: Condensed Matter* **18**, 4427-4442(2006).

91. Chatterji, T. *Colossal Magnetoresistive Manganites*. 447(Springer: 2004).

92. Gorbenko, O.Y. et al. Colossal isotope shift of the metal-insulator transition temperature in epitaxial thin films of LPCMO. *Aust. J. Phys.* **52**, 269-278(1999).

93. Amelitchev, V.A. et al. Structural and chemical analysis of colossal magnetoresistance manganites by Raman spectrometry. *Phys. Rev. B* **63**, 104430(2001).

94. Hwang, H.Y. et al. Lattice Effects on the Magnetoresistance in Doped LaMnO3. *Phys. Rev. Lett.* **75**, 914(1995).

95. Dey, P. & Nath, T.K. Enhanced grain surface effect on the temperature-dependent behavior of spin-polarized tunneling magnetoresistance of nanometric manganites. *Appl. Phys. Lett.* **87**, 162501-3(2005).

96. Mayr, M. et al. Resistivity of Mixed-Phase Manganites. *Phys. Rev. Lett.* **86**, 135(2001).

97. Mathur, N.D. & Littlewood, P.B. The self-organised phases of manganites. *Solid State Communications* **119**, 271-280(2001).

98. Zhou, C. & Zhang, X.G. Numerical study of the noise power of carbon nanowire network. *Accepted: Phys. Rev. B* (2008).

99. Reutler, P. et al. Local magnetic order in manganite thin films studied by 1/f noise measurements. *Phys. Rev. B* **62**, 11619(2000).

100. Lee, H.J. et al. Optical evidence of multiphase coexistence in single crystalline (La,Pr,Ca)MnO₃ . *Phys. Rev. B* **65**, 115118(2002).

101. Singh, U.R. et al. Tunneling study of the charge-ordering gap on the surface of La0.350Pr0.275Ca0.375MnO3 thin films. *Phys. Rev. B* **77**, 14404(2008).

102. Yu, R. et al. Short-range spin and charge correlations and local density of states in the colossal magnetoresistance regime of the single-orbital model for manganites. *Phys. Rev. B* **77**, 214434-12(2008).

103. Siwach, P.K., Singh, H.K. & Srivastava, O.N. Influence of strain relaxation on magnetotransport properties of epitaxial La0.7Ca0.3MnO3 films. *J. Phys: Condens. Matter* 9783(2006).

104. Meir, Y. Percolation-Type Description of the Metal-Insulator Transition in Two Dimensions. *Phys. Rev. Lett.* **83**, 3506(1999).

105. Lust, L.M. & Kakalios, J. Dynamical Percolation Model of Conductance Fluctuations in Hydrogenated Amorphous Silicon. *Phys. Rev. Lett.* **75**, 2192(1995).

106. Ralls, K.S. & Buhrman, R.A. Microscopic study of 1/f noise in metal nanobridges. *Phys. Rev. B* **44**, 5800(1991).

107. Kogan, S. *Electronic Noise and Fluctuations in Solids*. 275-277(Cambridge University Press: 1996).

108. Yuzhelevski, Y. et al. Metastable conductivity in low-doped manganites. *J. Appl. Phys.* **91**, 7397-7399(2002).

109. Reutler, P. et al. Local magnetic order in manganite thin films studied by 1/f noise measurements. *Phys. Rev. B* **62**, 11619(2000).

110. Raquet, B. et al. Noise Probe of the Dynamic Phase Separation in La2/3Ca1/3MnO3. *Phys. Rev. Lett.* **84**, 4485(2000).

111. Podzorov, V. et al. Phase separation and 1/f noise in low-TMI colossal magnetoresistance manganites. *Phys. Rev. B* **64**, 115113(2001).

112. Merithew, R.D. et al. Mesoscopic Thermodynamics of an Inhomogeneous Colossal-Magnetoresistive Phase. *Phys. Rev. Lett.* **84**, 3442(2000).

113. Hardner, H.T. et al. Non-Gaussian noise in a colossal magnetoresistive film. *J. Appl. Phys.* **81**, 272-275(1997).

114. Choudhary, R.J. et al. Evaluation of manganite films on silicon for uncooled bolometric applications. *Appl. Phys. Lett.* **84**, 3846-3848(2004).

115. Jiang, J. et al. Plan-View TEM Study on Interfacial Structure of (La, Ca)MnO3/MgO. *Microscopy and Microanalysis* **14**, 232-233(2008).

116. Scofield, J.H., Mantese, J.V. & Webb, W.W. 1/f noise of metals: A case for extrinsic origin. *Phys. Rev. B* **32**, 736(1985).

117. Quintero, M. et al. Phase coexistence regimes in La0.325Pr0.300Ca0.375MnO3. *Physica B* **354**, 63-66(2004).

Appendix

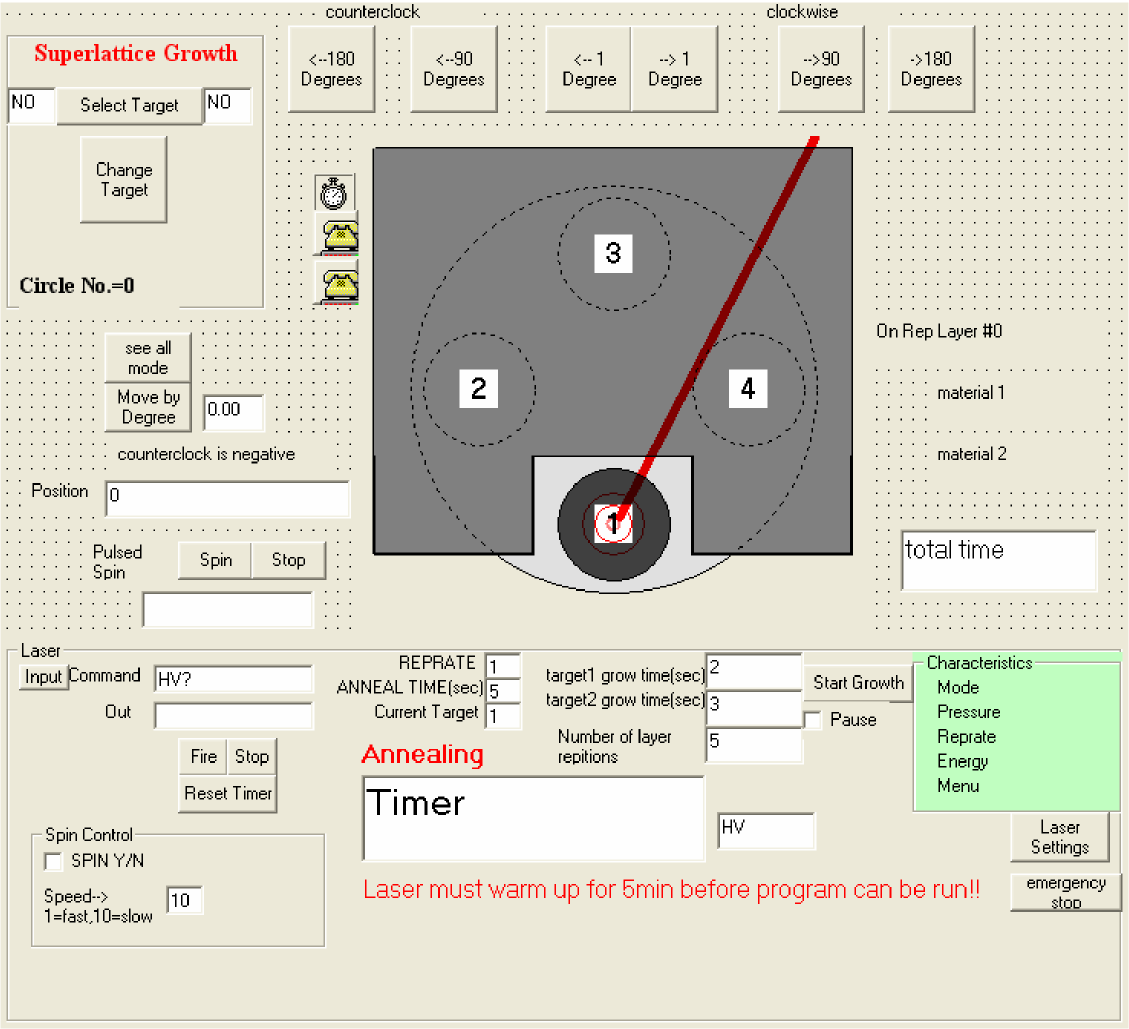

NO Select Target NO

Circle No.=0

Move by Degree 0.00

Position 0

On Rep Layer #0

total time

Command HV?

Out

REPRATE 1

ANNEAL TIME(sec) 5

Current Target 1

target1 grow time(sec) 2

target2 grow time(sec) 3

Number of layer repitions 5

☐ Pause

Timer

HV

Laser must warm up for 5min before program can be run!!

☐ SPIN Y/N

Speed--> 1=fast,10=slow 10

Figure A-1: Front Panel of Visual Basic sample growth controller.

```
Public z As Long, Y As Integer, p1 As Double, p2 As Double, p3 As Double, p4 As
    Double
Public start As Integer, diffpause As Long, firestart As Integer, firediffpause As Integer
    Public T1pos As Integer, T2pos As Integer, target1 As Integer, target2 As Integer
Public buttonstate As String
Public mode As Integer '092007 added
Public layertime As Integer
Public dis As Long
Public tt1layer As Integer, tt2layer As Integer, tt As Integer, tt1layerdone As Integer,
    tt2layerdone As Integer, tanneal1done As Integer, tanneal2done As Integer
```

```
Public ttsave As Integer, firediffpausesave As Integer, stepnum As Integer, stepnumsave
      As Integer
Public totaltime As Integer
Public movedis As Integer
Public totalturn As Long
Private Declare Sub Sleep Lib "kernel32" (ByVal dwMilliseconds As Long)

Private Sub timer()  'times growth process
Dim gmtime As SYSTEMTIME
Dim firediff As Integer
Dim firenow As Long
Dim firestart As Integer
Dim firestart1 As Integer
Dim firenow1 As Integer
Dim firestart2 As Integer
Dim firenow2 As Integer
Counter = 0


 GetSystemTime gmtime: Sleep (50): DoEvents
 firediff = 0
 Text5.Text = firediffpausesave & "pausesave " & firediffpause & "pause"
 firediffpause = firediffpausesave: DoEvents

 firestart = gmtime.wSecond + gmtime.wMinute * 60 + gmtime.wHour * 60 * 24 +
      gmtime.wDay * 24 * 3600 - firediffpause

 firenow = gmtime.wSecond + gmtime.wMinute * 60 + gmtime.wHour * 60 * 24 +
      gmtime.wDay * 24 * 3600


 firediff = firenow - firestart
 firediffpause = 0
 DoEvents          '09-20-07 added gmtime.wday to stop 24hr fault

While check2.Value = 0
 Label25.Caption = "On Rep Layer #" & tt + 1 & " save " & ttsave:
 firediffpausesave = 0
 stepnumsave = 1
 ttsave = 0
 If Check3.Value = 0 Then
 GetSystemTime gmtime: Sleep (50): DoEvents
 firenow = gmtime.wSecond + gmtime.wMinute * 60 + gmtime.wHour * 60 * 24 +
      gmtime.wDay * 24 * 3600
 firediff = firenow - firestart
```

```
Text15.Text = firediff \ 60 & " min " & firediff Mod 60 & " sec"
DoEvents
 If Counter = Text17.Text * 3000 Then
 If stepnum = 1 Then
 spin
 End If
 If stepnum = 3 Then
 spin
 End If
 lasersettings
 Counter = 0
 DoEvents
 End If
If firediff >= layertime Then
 check2.Value = 1
 layerdone = 1
 MSComm2.Output = "OPMODE=OFF" & vbCr: Sleep (50): DoEvents 'LASER OFF!!
firediff = 0 'added 10-12-06 problem with timer going to negative after long times
If stepnum = 1 Then
 target1 = Text1.Text
 target2 = Text2.Text
 movedis = 90 * (target1 - target2)
 dis = movedis
  love (dis)
  Sleep (1000): DoEvents
End If
If stepnum = 3 Then
 target1 = Text1.Text
 target2 = Text2.Text
 movedis = -90 * (target1 - target2)
 dis = movedis
  love (dis)
  Sleep (1000): DoEvents
End If
End If
 Counter = Counter + 1
Else
Check1.Value = 1
ttsave = tt
firediffpausesave = firediff
stepnumsave = stepnum: DoEvents
check2.Value = 1
layerrepsave = layerreps: DoEvents
MSComm2.Output = "OPMODE=OFF" & vbCr: Sleep (50): DoEvents 'LASER OFF!!
End If
```

```
 Wend
 firediffpause = firediff
 'firediffpausesave = firediff
If stepnum < 4 Then
 stepnum = stepnum + 1
Else
 stepnum = 1
End If
DoEvents
MSComm2.Output = "OPMODE=OFF" & vbCr: Sleep (50): DoEvents 'LASER OFF!!
End Sub


Private Sub Command3_Click() 'added 092007
If Check6.Value = 1 Then
Check6.Value = 0
Command7.Visible = False
Command8.Visible = False
Label2.Visible = False


ElseIf Check6.Value = 0 Then
Check6.Value = 1
Command7.Visible = True
Command8.Visible = True
Label2.Visible = True


End If
DoEvents

End Sub

Private Sub Command6_Click()
MSComm2.Output = Text3.Text & vbCr: Sleep (50): DoEvents
MSComm2.Input: Sleep (50): DoEvents
lasersettings

End Sub

Private Sub Estop_Click() 'resets all save values from superlattice growth pause
MSComm2.Output = "OPMODE=OFF" & vbCr: Sleep (50): DoEvents 'LASER OFF!!
ttsave = 0: tt = 0: firediffpausesave = 0: firediffpause = 0: stepnumsave = 1
Check1.Value = 0: check2.Value = 0: Check3.Value = 0: stepnum = 1:
```

```
firediffpausesave = 0
 stepnumsave = 1
 ttsave = 0
End Sub

Private Sub Pause_Click()
Check1.Value = 1: check2.Value = 1
ttsave = tt
firediffpausesave = firediffpause
stepnumsave = stepnum
MSComm2.Output = "OPMODE=OFF" & vbCr: Sleep (50): DoEvents 'LASER OFF!!
End Sub
Private Sub startgrowth_Click()   'startgrowth button
'Dim tt As Integer
Dim tt1layer As Integer
Dim tt2layer As Integer
Dim tanneal As Integer
Check1.Value = 0
check2.Value = 0
Check3.Value = 0

tt1layer = Text11.Text: tt2layer = Text12.Text: tanneal = Text9.Text
layerreps = Text13.Text - 1
DoEvents
tt = 0
tottime = ((tt1layer + tt2layer + (tanneal * 2)) * Text13.Text)
Text14.Text = tottime \ 60 & "min " & tottime Mod 60 & "sec Remaining"

buttonstate = False: enablebuttons
stepnum = stepnumsave
tt = ttsave + tt
While tt <= layerreps

 If Check1.Value = 1 Then
 check2.Value = 1
 Check3.Value = 0
 Else
 If stepnum = 1 Then
 check2.Value = 0
 stepnum = 1
 Label26.Caption = "GROWING MATERIAL 1"
 Label27.Caption = "material 2 waiting"
 layertime = tt1layer  'target 1
 MSComm2.Output = "Reprate=" & Text6.Text & vbCr: Sleep (50): DoEvents
 MSComm2.Output = "OPMODE=OFF" & vbCr: Sleep (50): DoEvents  'LASER ON!!
```

```
 Y = 1: timer: Y = 0: firediffpause = 0:
 Label26.Caption = "material 1 layer finished": DoEvents
 End If
End If

If Check1.Value = 1 Then
 check2.Value = 1
 Check3.Value = 0
Else
 If stepnum = 2 Then
 check2.Value = 0
 stepnum = 2
 layertime = tanneal: Label24.Caption = "Anneal #1": Label24.Visible = True: DoEvents
 Y = 1: timer: Y = 0: Label24.Visible = False: firediffpause = 0:
 DoEvents
 End If
End If

If Check1.Value = 1 Then
 check2.Value = 1
 Check3.Value = 0
Else
 If stepnum = 3 Then
 check2.Value = 0
 stepnum = 3
 Label27.Caption = "GROWING MATERIAL 2": layertime = tt2layer: DoEvents
 MSComm2.Output = "Reprate=" & Text6.Text & vbCr: Sleep (50): DoEvents
 MSComm2.Output = "OPMODE=OFF" & vbCr: Sleep (50): DoEvents  'LASER ON!!
 Y = 1: timer: Y = 0: firediffpause = 0:
 Label27.Caption = "material 2 layer finished": DoEvents
 End If
End If

If Check1.Value = 1 Then
 check2.Value = 1
 Check3.Value = 0
Else
 If stepnum = 4 Then
 check2.Value = 0
 stepnum = 4
 layertime = tanneal: Label24.Caption = "Anneal #2": Label24.Visible = True: DoEvents
 Y = 1: timer: Y = 0: Label24.Visible = False: firediffpause = 0:
 DoEvents
 End If
End If
```

```
Check3.Value = 0
tt = tt + 1
Wend
buttonstate = True: enablebuttons
'Label25.Caption = "Finished Layer #" & tt:
End Sub
Private Sub love(ByVal d As Long) 'controls move
'Dim totalturn As Long
'l = 0
buttonstate = False: enablebuttons
cir (dis)
 l = dis / 360: DoEvents
totalturn = totalturn + dis
 MSComm1.Output = "speed=.1" & vbCr: Sleep (250)
 MSComm1.Output = "out(4)=0" & vbCr: Text7.Text = "Target NOT Spinning": Sleep (250):
 MSComm1.Output = "movei=" & l & vbCr: Sleep (500): MSComm1.Output = "abspos" & vbCr: DoEvents

Sleep (250): 'Text5.Text = l
Text5.Text = totalturn Mod 360

'Text1.Text = Text2.Text: Text2.Text = Text3.Text: Text3.Text = Text4.Text: Text4.Text = n
Sleep (250): z = z + 1
If z = 4 Then
z = 0
End If
buttonstate = True: enablebuttons
End Sub

Private Sub lasersettings()

MSComm2.Output = "MODE?" & vbCr: Sleep (50): DoEvents
Label17.Caption = "MODE = " & MSComm2.Input: DoEvents
MSComm2.Output = "pressure?" & vbCr: Sleep (50): DoEvents
Label18.Caption = "Pressure = " & MSComm2.Input: Sleep (50): DoEvents
MSComm2.Output = "REPRATE?" & vbCr: Sleep (50): DoEvents
Label19.Caption = "Reprate = " & MSComm2.Input: Sleep (50): DoEvents
MSComm2.Output = "EGY?" & vbCr: Sleep (50): DoEvents
Label20.Caption = "Energy = " & MSComm2.Input: DoEvents
MSComm2.Output = "MENU?" & vbCr: Sleep (50): DoEvents
Label21.Caption = "Menu: " & MSComm2.Input
```

```
End Sub

Private Sub stopspin()
Y = 0
MSComm1.Output = "out(4)=0" & vbCr:
Text7.Text = "Target NOT Spinning": DoEvents
MSComm1.Output = "speed=.1" & vbCr: Sleep (500) ' set speed
End Sub

Private Sub spin()
If Check5.Value = 1 Then
 Text4.Text = "target spinning"
Y = 1
MSComm1.Output = "speed=0.1" & vbCr: ' set speed

 MSComm1.Output = "movei=-.0027778 " & vbCr: Sleep (250): DoEvents
 MSComm1.Output = "out(4)=1" & vbCr: Sleep (30) '092007 time down from 50

 MSComm1.Output = "out(4)=0" & vbCr: 'Sleep (50)
 MSComm1.Output = "movei=.0027778 " & vbCr: Sleep (250)
 DoEvents
 Text7.Text = "Target Spinning": 'Sleep (300)
 DoEvents: Sleep (100):

Else

Text4.Text = "target not spinning"


End Sub
Private Sub enablebuttons()
Command1.Enabled = buttonstate: Command2.Enabled = buttonstate
Command4.Enabled = buttonstate: Command5.Enabled = buttonstate
Command7.Enabled = buttonstate: Command8.Enabled = buttonstate
Command9.Enabled = buttonstate: Command10.Enabled = buttonstate
Command11.Enabled = buttonstate: Command12.Enabled = buttonstate
Command13.Enabled = buttonstate: Command17.Enabled = buttonstate
Command18.Enabled = buttonstate: startgrowth.Enabled = buttonstate
Fire.Enabled = buttonstate
End Sub
Private Sub cir(ByVal d As Double)
r = 1320 'radius of large circle
q = 360
p1 = ((-d * 3.14159265) / 180) + p1  'this section controls target graphics
p2 = 1.570796325 + p1
```

```
p3 = 3.14159265 + p1
p4 = 4.712388975 + p1

Shape9.Left = (r * Cos(p1)) + r + 600     'target 4
Shape9.Top = (r * -Sin(p1)) + r + 600
Shape11.Left = Shape9.Left: Shape11.Top = Shape9.Top
Label6.Left = (r * Cos(p1)) + r + 600 + q
Label6.Top = (r * -Sin(p1)) + r + 600 + q

Shape3.Left = (r * Cos(p2)) + r + 600     'target3
Shape3.Top = (r * -Sin(p2)) + r + 600
Shape13.Left = Shape3.Left: Shape13.Top = Shape3.Top
Label7.Left = (r * Cos(p2)) + r + 600 + q
Label7.Top = (r * -Sin(p2)) + r + 600 + q

Shape4.Left = (r * Cos(p3)) + r + 600     'target 2
Shape4.Top = (r * -Sin(p3)) + r + 600
Shape12.Left = Shape4.Left: Shape12.Top = Shape4.Top
Label4.Left = (r * Cos(p3)) + r + 600 + q
Label4.Top = (r * -Sin(p3)) + r + 600 + q

Shape10.Left = (r * Cos(p4)) + r + 600    'target 1
Shape10.Top = (r * -Sin(p4)) + r + 600
Shape8.Left = Shape10.Left: Shape8.Top = Shape10.Top
Label5.Left = (r * Cos(p4)) + r + 600 + q
Label5.Top = (r * -Sin(p4)) + r + 600 + q
End Sub

Private Sub Command13_Click()    'set targets to use for growth

target1 = Text1.Text
target2 = Text2.Text
'If Label5.Caption = 1 Then

movedis = 90 * (target1 - target2)
End Sub

Private Sub Command18_Click()
firediffpause = 0
End Sub

Private Sub Command17_Click()  'return laser settings button
lasersettings
End Sub
```

```
Private Sub Fire_Click()   'start fire for laser with reprate

Dim u As Integer
check2.Value = 0
MSComm2.Output = "Reprate=" & Text6.Text & vbCr: Sleep (50): DoEvents
MSComm2.Output = "OPMODE=ON" & vbCr: Sleep (50): DoEvents 'LASER ON!!!
Text7.Text = "Target Spinning"

While Check5.Value = 1

 If u = Text17.Text * 3000 Then '9-20-07
 spin
 u = 0
 Else
 u = u + 1
 End If
Wend

Y = 1
'timer
Y = 0
Text7.Text = "Target not Spinning"
End Sub

Private Sub Stop_Click()   'stops laser
'check2.Value = 1
Check4.Value = 1
MSComm2.Output = "OPMODE=OFF" & vbCr: Sleep (50): DoEvents 'Laser off
Text4.Text = stopped
lasersettings
Text7.Text = "Target Not Spinning"
'Y = 0
End Sub


Private Sub Command10_Click()   '180 degree clockwise
dis = -180
love (dis)
End Sub
Private Sub Command11_Click()    '180 degree counterclockwise
dis = 180
love (dis)
End Sub
Private Sub Command4_Click()    '1 degree clockwise movement
buttonstate = False: enablebuttons
```

```
dis = -1
cir (dis)
MSComm1.Output = "speed=0.1" & vbCr: MSComm1.Output = "movei=-.0027778 " &
      vbCr:
Sleep (250): DoEvents
buttonstate = True: enablebuttons
End Sub
Private Sub Command5_Click()    '1 degree counter clockwise move
buttonstate = False: enablebuttons
dis = 1
cir (dis)
MSComm1.Output = "speed=0.1" & vbCr: MSComm1.Output = "movei=.0027778 " &
      vbCr:
Sleep (250): DoEvents
buttonstate = True: enablebuttons
End Sub
Private Sub Command1_Click()    '90 degree clockwise
dis = -90
love (dis)
End Sub
Private Sub Command9_Click()    '90 degree counterclockwise
dis = 90
love (dis)
End Sub

Private Sub Command7_Click()     'spin button
Y = 1
MSComm1.Output = "speed=0.1" & vbCr: ' set speed
While Y = 1
MSComm1.Output = "movei=-.0027778 " & vbCr: Sleep (250): DoEvents
 MSComm1.Output = "out(4)=1" & vbCr: Sleep (25)

 MSComm1.Output = "out(4)=0" & vbCr: 'Sleep (50)
 MSComm1.Output = "movei=.0027778 " & vbCr: Sleep (250)
DoEvents
Text7.Text = "Target Spinning": 'Sleep (300)
DoEvents: Sleep (100):
Wend
If Y = 0 Then
MSComm1.Output = "speed=.1" & vbCr: Sleep (500) ' set speed
End If
Text7.Text = "Target NOT Spinning":
End Sub

Private Sub Command8_Click() 'stop spin button
```

```
Y = 0
MSComm1.Output = "out(4)=0" & vbCr:
Text7.Text = "Target NOT Spinning": DoEvents
MSComm1.Output = "speed=.1" & vbCr: Sleep (500) ' set speed
End Sub

Private Sub Command2_Click()   'select degree movement
MSComm1.Output = "speed=.1" & vbCr: Sleep (250)
Y = 0: n = 0
Y = Text8.Text: cir (-Y) 'enter movement
n = Y * 0.0027778

MSComm1.Output = "out(4)=0" & vbCr: Text7.Text = "Target NOT Spinning": Sleep
    (250)
MSComm1.Output = "movei=" & n & vbCr: Sleep (1000): MSComm1.Output =
    "abspos" & vbCr
Sleep (250): Text5.Text = MSComm1.Input
End Sub

Private Sub Form_Load()
z = 0: Y = 0: p1 = 0: p2 = 0: p3 = 0: p4 = 0
Check6.Value = 0
diffpause = 0
Dim gmtime As SYSTEMTIME
Dim TheTime As String
buttonstate = True
Label24.Visible = False
stepnumsave = 1: firediffpausesave = 0
'totalturn = 0
For X = 1 To 10000

Next

MSComm1.CommPort = 1   'open port to stepper motor
MSComm1.Settings = "9600,N,8,1"
MSComm1.PortOpen = True

MSComm2.CommPort = 2   'open port to laser
MSComm2.Settings = "9600,N,8,1"
MSComm2.PortOpen = True

MSComm1.Output = "wndgs=1" & vbCr: Sleep (500) 'turn on current
MSComm1.Output = "speed=.1" & vbCr: Sleep (500) ' set speed
MSComm1.Output = " abspos=0" & vbCr: Sleep (500) 'reset position
```

```
End Sub


Private Sub Form_Unload(Cancel As Integer)
MSComm1.Output = "out(4)=0" & vbCr: Sleep (250)
MSComm1.Output = "speed=.1" & vbCr: Sleep (250)
MSComm2.Output = "OPMODE=OFF" & vbCr: Sleep (50)
'Dim bb As Long

bb = (totalturn Mod 360) / -360
Text14.Text = bb
MSComm1.Output = "movei=" & bb & vbCr: Sleep (5000): MSComm1.Output =
      "abspos" & vbCr: DoEvents


' If z = 1 Then
'MSComm1.Output = "movei=-.25" & vbCr: Sleep (1000) 'moves back to initial pos
'MSComm1.Output = "movei=-.25" & vbCr: Sleep (1000)
'MSComm1.Output = "movei=-.25" & vbCr: Sleep (1000)
'ElseIf z = 2 Then
'MSComm1.Output = "movei=-.25" & vbCr: Sleep (1000)
'MSComm1.Output = "movei=-.25" & vbCr: Sleep (1000)
'ElseIf z = 3 Then
'MSComm1.Output = "movei=-.25" & vbCr: Sleep (1000)
'End If

 MSComm1.Output = "wndgs=0" & vbCr: Sleep (250)  'turn off current
 MSComm1.PortOpen = False     'Close port to stepper

 MSComm2.PortOpen = False     'Close port to laser
End Sub



‘MODULE1
Public Declare Sub GetSystemTime Lib "kernel32" (lpSystemTime As SYSTEMTIME)
Public Declare Function SetSystemTime Lib "kernel32" (lpSystemTime As
      SYSTEMTIME) As Long

Public Type SYSTEMTIME
  wYear As Integer
  wMonth As Integer
  wDayOfWeek As Integer
  wDay As Integer
  wHour As Integer
```

```
  wMinute As Integer
  wSecond As Integer
  wMilliseconds As Integer
End Type
```

Vita

Thomas Zachariah Ward was born and raised in Jefferson City, Missouri. After graduating from public high school, he spent the next 7 years intermittently studying English literature and creative writing at the University of Missouri and traveling. By the time he graduated with a BA in English in 2000, he had lived in Japan, Australia and France, hitchhiked through 20 countries and knew that no one was interested in what he was writing.

In 2001, he was accepted into the naval officer candidate school with a contract to become a naval aviator. This boyhood dream of flying jets off of boats was crushed when terrorists destroyed the world trade center, thereby pushing his scheduled flight training back several months making him ineligible due to his advanced old age of twenty-six.

In a fit of masochism, he returned to the University of Missouri to study Physics and earned a BS in 2004. Not wanting the torture to end, he enrolled in the Physics PhD program at the University of Tennessee. The next 4 years were devoted to not looking directly into lasers and not spilling hydrofluoric acid on himself. With these two goals met, he was awarded a PhD in December 2008.

He is currently living in Knoxville, Tennessee with his long standing roommate Jenny Burkemper and a fat little dog named Walter. Incredibly, Zac continues to grow more intelligent and more handsome with each passing month. You can be assured that this is so, since he has written this *vita* himself and his Physics training has taught him a devotion to absolute objectivity.